STRUCTURAL CHARACTERIZATION OF EPITAXIAL GRAPHENE ON SILICON CARBIDE

A Thesis
Presented to
The Academic Faculty

by

Joanna R. Hass

In Partial Fulfillment
of the Requirements for the Degree
Doctor of Philosophy in the
School of Physics

Georgia Institute of Technology
December 2008

STRUCTURAL CHARACTERIZATION OF EPITAXIAL GRAPHENE ON SILICON CARBIDE

Approved by:

Professor Phillip N. First, Advisor
School of Physics
Georgia Institute of Technology

Professor Edward H. Conrad, Advisor
School of Physics
Georgia Institute of Technology

Professor Walter A. de Heer
School of Physics
Georgia Institute of Technology

Professor Andrew Zangwill
School of Physics
Georgia Institute of Technology

Professor Brent Carter
Department of Materials Science and Engineering
Georgia Institute of Technology

Date Approved: 11 November 2008

To my parents, Jayne Byrnes and Arthur Hass.

ACKNOWLEDGEMENTS

I would like to graciously thank my thesis committee: Dr. Walter de Heer, Dr. Andrew Zangwill, Dr. Brent Carter, and most of all, my co-advisors Dr. Phillip First and Dr. Edward Conrad. Phil and Ed have truly been ideal graduate student advisors, providing a perfect balance between guidance to move the project forward and freedom to make creative decisions. I am grateful to the former students who built the UHV chamber and STM: Paul Quesenberry and Bill Cullen, and the former students I was able to work with who helped me learn many experimental techniques: Rui Feng, Craig Jeffery, Tianbo Li, Asmerom Obazghi, and Sameh Dardona. I am also extremely grateful to many current students who work with Dr. First, Dr. Conrad, and Dr. de Heer: Greg Rutter, D. Lee Miller, Kevin Kubista, D. Britt Torrence, Xuebin Li, Fan Ming, Jorge Millán-Otoya and most of all Mike Sprinkle and Nikhil Sharma. Without their collaboration and generous help, none of this work could have ever been completed.

My close friends at Georgia Tech have provided immense support throughout my graduate studies, so I am extremely grateful to them as well: Eva Bookjans, Adam Steele, Brandon Donehoo, and of course, Adam Perkins. Finally, I want to thank my family. My mother and father have encouraged a true love of learning throughout my life that led me to follow this path. I owe so much to them, as well as my sister, Kendra, stepmother, Karen and my grandparents, who before I was born ensured that college would be a part of my future.

TABLE OF CONTENTS

LIST OF TABLES

LIST OF FIGURES

SUMMARY

This work examines the structural character of epitaxial graphene on silicon carbide via surface X-ray diffraction (SXRD) and scanning tunneling microscopy (STM), as well as other surface science techniques. Graphene, a single sheet of carbon atoms sp^2-bonded in a honeycomb lattice, is a possible all-carbon successor to silicon electronics. Ballistic conduction at room temperature and a linear dispersion relation that causes carriers to behave as massless Dirac fermions are features that make graphene promising for high-speed, low-power devices. Critical advantages of epitaxial graphene (EG) grown on SiC are its compatibility with standard lithographic procedures and the ability to fabricate both devices and contacts from the same material.

SXRD and STM results are presented on the domain structure, interface composition and stacking character of graphene grown on both polar faces of semi-insulating 4H-SiC. The data reveal intriguing differences between graphene grown on these two faces. Substrate roughening is more pronounced and graphene domain sizes are significantly smaller on the SiC(0001) Si-face compared to the SiC($000\bar{1}$) C-face. Specular X-ray reflectivity measurements show that both faces have a carbon rich, extended interface that is tightly bound to the first graphene layer. This results in charge transfer between the graphene and the SiC substrate and leads to a buffering effect that shields the first graphene layer from the bulk SiC, as predicted by *ab initio* calculations.

In-plane X-ray crystal truncation rod analysis indicates that rotated graphene layers are interleaved in C-face graphene films. These rotational faults are most likely

caused by joint graphene/SiC and graphene/graphene commensurate supercells. Corresponding superstructures are observed in STM topographs, further evidence for the presence of rotational stacking faults. The unique stacking character of multilayer C-face graphene is shown to preserve the linear dispersion found in single layer graphene, making EG electronics possible even for a multilayer material.

Details about each experimental apparatus used and their principles of operation are also explained to supplement the understanding of work presented.

CHAPTER I

INTRODUCTION

1.1 Research Motivation & History

Properties of epitaxial graphene grown on SiC have shown its potential as a viable candidate for post CMOS electronics.[1,2] At some point in the near future, the path to lower power, faster, smaller integrated circuits via silicon technology will come to an end. New systems will have to be implemented for the continuation of Moore's law and continued innovation in industry. This provides an impetus for a thorough study of the properties of epitaxial graphene (EG) and how it can be produced.

Graphene studies sprouted from research on the attractive electronic properties of carbon nanotubes (CNTs) that led to a variety of work towards developing CNT electronic switching devices. Problems with large intrinsic resistance in contacts and the inability to control tube helicity (i.e. whether or not they are metallic or semiconducting) made large scale CNT integrated circuit designs problematic. A solution to these problems was proposed when it was deduced that the electronic properties of a graphene ribbon patterned on a SiC substrate should be similar to those of a CNT.[1] It was pointed out that that graphene ribbons can be considered as an unrolled CNTs with different boundary conditions (two dimensional versus cyclic).[1,3] The advantage of epitaxial graphene over CNTs for electronics resides in its planar 2D structure and the fact that it is affixed to a substrate. This enables circuit design with standard lithography techniques and provides a platform on which graphene can be cut with different shapes and selected edge direction. By selecting the correct ribbon edge direction and ribbon width, it should be possible to tailor a bandgap for semiconducting graphene ribbons[3–6](analogous to helicity in CNTs).

Research into the electronic properties of graphene has followed two parallel courses. One involves the study of mechanically exfoliated graphene sheets.[7–9] Here, graphene flakes (typically micron size) are mechanically pealed from a bulk graphite crystal and placed onto a support substrate. Once a single graphene sheet is subsequently located by optical microscopy, metal contacts are attached for transport studies.[7–9] The second research avenue involves graphene directly grown on large area insulating or semiconducting SiC substrates. Once grown, the films are lithographically patterned and metal contacts applied to make electronic devices.[1] Graphene produced this way is referred to as Epitaxial Graphene (EG).

Mechanically exfoliated graphene flakes have been used to study a variety of fundamental graphene properties. They have been shown to exhibit 2D transport properties characteristic of chiral massless Dirac electrons expected for an isolated graphene sheet.[10] These include an unusual half integer quantum Hall effect and a non-zero Berry's phase.[8,9] What has propelled epitaxial graphene research as a leading contender for post CMOS electronics was the discovery that even multilayer graphene films grown on SiC show electronic properties similar to an isolated graphene sheet. These include a Berry's phase of π, weak anti-localization and a square root dependence of Landau level energies with applied magnetic field.[11–13]

The similarity of EG and exfoliated graphene's transport properties to those of a theoretically isolated graphene sheet is remarkable considering that graphene/substrate interactions should influence the 2D Dirac electrons responsible for graphene's unusual properties. The result is also very fortuitous since graphene grown on an insulating substrate promises the most practical and scalable approach to 2D graphene electronics. For this reason graphene grown on SiC has been the focus of research targeting a path towards graphene electronics.

Progress in this field requires a detailed understanding of both the structure and growth of epitaxial graphene. For that reason, this thesis work examines the structure

of graphene grown on SiC.

1.2 Research Objectives

The motivation provided above led directly to the goals of this work. They were:

- to characterize the surface morphology of graphene grown on the two polar faces, (0001) and $(000\bar{1})$, of hexagonal SiC
- to develop a structural model of the EG/SiC interface region for both polar faces
- to gain an understanding of how graphene's single layer properties are maintained despite its epitaxial relationship with a substrate.

All of the above was to be accomplished using a variety of experimental surface science techniques, with a focus on surface X-ray diffraction (SXRD) and scanning tunneling microscopy (STM). Indeed, all of these major goals have been addressed in this thesis, with the hope that this work has contributed to the development of a successful EG electronics paradigm.

CHAPTER II

GRAPHENE BACKGROUND: WHY ALL THE HYPE?

2.1 Defining Graphene

Structurally, graphene is defined as a single two dimensional hexagonal sheet of carbon atoms as shown in Fig. 1(a). The standard in-plane unit cell vectors are $|\mathbf{a}_\mathrm{G}| = |\mathbf{b}_\mathrm{G}| = 2.4589\text{Å}$.[14] The unit cell contains two carbon atoms at (0,0) and $(a_\mathrm{G}/3, 2b_\mathrm{G}/3)$. This gives a carbon areal density of 3.820 atoms/Å^2.

Graphene can also be defined by its unusual, theoretically predicted electronic properties. This description involves an infinite 2D plane of carbon atoms, arranged as described above, isolated in free space. This theoretical system has been studied at length over the past 50 years. Predictions made regarding its linear energy dispersion (a signature of relativistic charge carriers) and 2D electron gas properties have frequently been used as a second way of classifying what is known as "graphene" Any physical study of graphene involves complications, (primarily manifested as graphene-substrate interactions) thus recently the name "graphene" has been applied to a larger family of physical materials for which the electronic properties mentioned above have

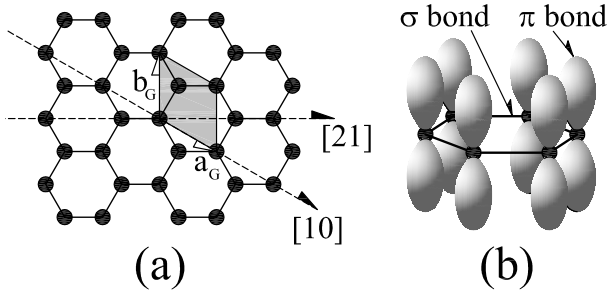

Figure 1: (a) Graphene hexagonal structure of identical carbon atoms. The unit cell (shaded) containing 2 carbon atoms is shown along with standard unit cell vectors $\mathbf{a}_\mathrm{G}$ and $\mathbf{b}_\mathrm{G}$. The [21] "armchair" edge and the [10] "zig-zag" directions are shown. (b) Schematic of the in plane σ bonds and the π orbitals perpendicular to the plane of the sheets.

been experimentally verified. In this thesis, a structural definition of graphene will be used, regardless of its surrounding environment. This is with the caveat that the unique electronic properties of graphene refer to those from an *electronically isolated* graphene sheet and that the electronic properties of epitaxial graphene (EG) structures are not necessarily those of an isolated sheet.

Graphene bonds are hybridized into a sp^2 configuration. There are three in-plane (σ) bonds per atom. These bonds are extremely strong and form the rigid backbone of the hexagonal structure. It is the partially filled p_z orbitals (π orbitals) perpendicular to the plane that are responsible for electron conduction [see Fig. 1(b)]. Due to the out-of-plane π orbitals, interactions between graphene and a substrate or between graphene layers should and does influence the electronic structure of epitaxial graphene. The fact that transport properties of isolated exfoliated graphene flakes and multilayer epitaxial graphene grown on SiC are similar, despite the graphene/SiC interface and layer interactions in multilayer EG films, is quite surprising. This point will be addressed repeatedly throughout this thesis.

Sheets of graphene are known to stack in a number of ways to produce materials with the generic name of graphite. The three most common stacking arrangements are: Hexagonal or $AA..$ stacking, Bernal or $AB..$ stacking, and Rhombohedral or $ABC..$ stacking [see Fig. 2]. The lowest energy stacking and most abundant configuration (80%)[15] in single crystal graphite is Bernal stacking. Bernal structure is formed by stacking two graphene sheets on top of each other and rotating one 60° relative to the other about a z axis (in the $\widehat{\mathbf{c}}$ direction through any atom). The sheets are separated by a distance $c_{\mathrm{G}}/2$ where $c_{\mathrm{G}} = 6.672$Å at 4.2K and 6.708Å at 297K.[14] This produces two sublattices of atoms, an A atom positioned above an A atom in the sheet below or a B atom with no atom below it in the adjacent sheet. The Bernal cell has four atoms/cell. In Bernal graphite the overlap of partially filled p_z orbitals (π orbitals) perpendicular to the plane account for the weak bonding between $AB..$

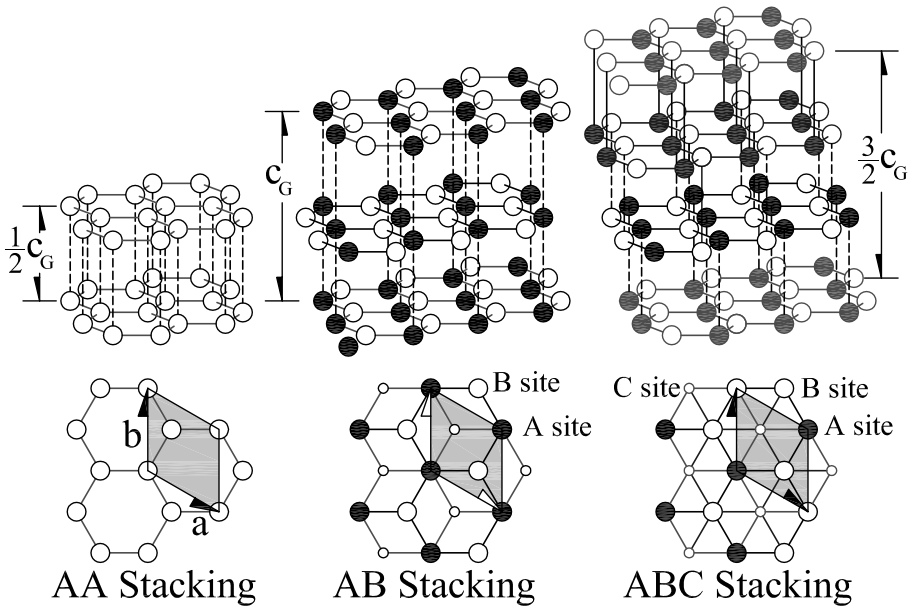

Figure 2: Three common graphite structures with different graphene stacking arrangements: (i) Hexagonal *AA..* stacking, (ii) Bernal *AB..* stacking and (iii) Rhombohedral *ABC..* stacking. Shaded area is the unit cell.

sheets. These bonds are sometimes referred to as Van der Waals bonds.[16]

Hexagonal *AA..* stacking consists of two unrotated sheets separated by a distance $c_G/2$ perpendicular to the sheets [Fig. 2]. This is the least common form of graphite ($<6\%$). It contains a single sheet sublattice with two atoms per cell. Rhombohedral graphite, which accounts for 14% of natural graphite,[15] is formed with three graphene sheets each separated by $c_G/2$ [see Fig. 2]. The second sheet is rotated relative to the first by 60° as in Bernal graphite. The third sheet has the same orientation relative to the second but is translated $(2a_G/3, b_G/2)$ from the second sheet. The Rhombohedral cell has 6 atoms. Note that that $c_G/2$ in Fig. 2 is slightly different for each stacking arrangement. These differences are $\sim 0.2\%$[17] of Bernal stacking and can usually be ignored.

2.2 Unique Properties of Graphene

2.2.1 Electronic Band Structure

The electronic band structure of graphene was first calculated by Wallace as early as 1947.[18] Figure 3(a) shows an *ab initio* band structure calculation for an isolated graphene sheet. The crucial aspect of the band structure occurs at E_F ($E = 0$ in the plot) with the electron momentum near the K-point. Hopping between the two equivalent carbon sublattices A and B (see Fig. 1) leads to the formation of energy bands which intersect at the zone boundary K-point.[19] These intersection points are known as Dirac points. The energy dispersion near the Dirac points is linear; $E = \hbar k v_F$ where $v_F \approx c/300$ and gives rise to a Fermi surface near $E = 0$ that is composed of the six Dirac cones seen in Fig. 3(b) and (c)). This unique linear dispersion means that the effective mass of the electrons is zero near E_F.

The linear dispersion has another important consequence on the electron states below E_F and the hole states above E_F. Electrons and holes cannot be described by independent Schrödinger equations, as they are in most solid state materials. Instead the electrons and holes are represented as quasi-particles connected in a way that is best described by the Dirac equation.[10,20–28] Electrons and holes belonging to the same branch of the dispersion curve are described by a pseudospin σ that is parallel to the electron momentum but opposite the hole momentum. This "chirality" means that an electron hopping from K to K' [see Fig. 3(b)] is not allowed since the pseudospin is not conserved. This conservation rule gives rise to the ballistic transport observed in graphene and CNTs.[19] As in CNTs, electron phonon scattering is expected to be very weak.[29,30] This coupled with the fact that long range Coulomb potentials cannot trap Dirac quasi-particles[31,32] means that coherence lengths can be very large in graphene.[11]

The fundamental properties of graphene discussed above are altered when the

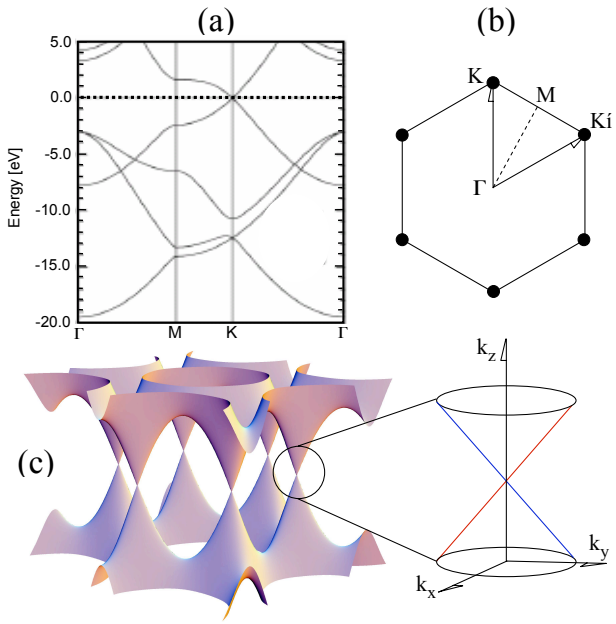

Figure 3: (a) An *ab initio* band structure calculation of graphene from [33]. (b) a schematic of the Fermi surface of graphene consisting of points intersecting the Dirac cone. (c) The two dimensional tight binding energy surface of graphene, from [34]. The blow up shows the linear dispersion (Dirac cones) near the K-point in the vicinity of $E = E_F$.

equivalence of A and B sublattices is broken. This can occur in many ways. For instance, in thin ribbons of graphene the edge structure becomes important. A ribbon width dependent gap opens at E_F that depends on the details of the edge geometry and termination.[3–5] Graphene ribbons with "armchair" edges running in the [21] direction in Fig. 1 contain both A and B sites on the edge while the "zig-zag" edges running in the [10] direction contain either all A or all B sites. "Armchair" ribbons are known to be semiconducting with a ribbon width dependent band gap. "Zig-zag" ribbons were initially expected to be metallic,[3] although more recent *ab initio* calculations show that they in fact have nonzero direct band gaps as well.[5] Relationships between ribbon width and crystallographic orientation have been studied experimentally using mechanically exfoliated graphene sheets, however precise control over edge directions has not yet been achieved.[6]

The stacking sequence of graphene layers can also significantly alter its band structure by breaking the symmetry of the A and B sublattices.[24,25,28,33] While AA..

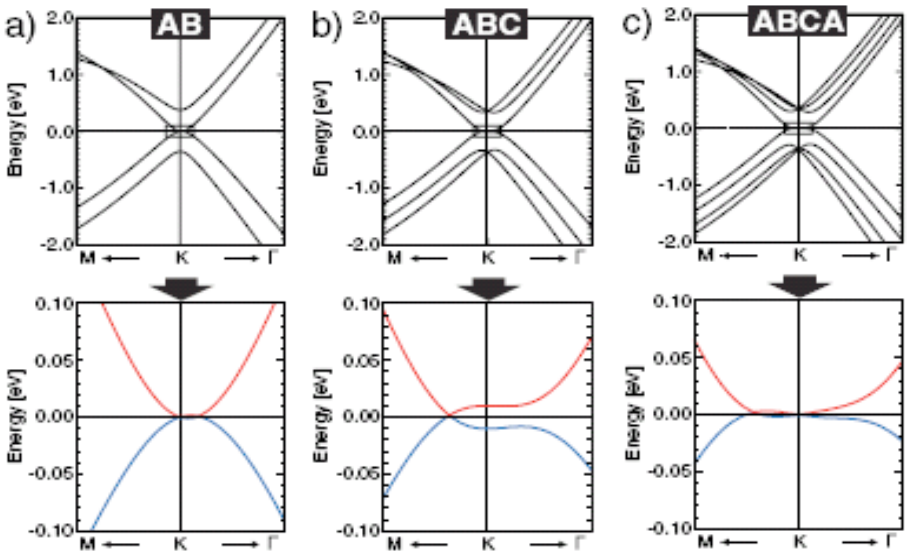

Figure 4: *Ab intio* band structures near the K-point at four different graphene stacking arrangements. (a) an AB stacked graphene pair, (b) three ABC stacked graphene sheets and (c) four $ABCA$ stacked graphene sheets. Bottom panels are blowups of the band crossings near $E=E_F$. Taken from [33].

stacking of graphene sheets preserves the symmetry, $AB..$ stacking does not. In $AB..$ stacking the A atoms are bonded to A atoms in the plane above while B atoms have no corresponding atom in the plane above [see Fig. 2]. This causes A and B lattice atoms to be distinguishable.

Results from a density functional theory (DFT) calculation that explores the effects of different stacking on the band structure of multilayer graphene are shown in Fig. 4. In both Bernal and Rhombohedral stacking the weak inter-planar interaction breaks the lattice symmetry and produces bonding π and σ states and anti-bonding π^* and σ^* states resulting in a splitting of the bands near the Dirac point and a corresponding change change in energy dispersion that is no longer linear.

Such effects have also been demonstrated experimentally via angle resolved photoemission spectroscopy (ARPES.)[35–38] This is a photon-in, electron-out technique which is capable of directly mapping a crystal's electronic energy-momentum phase space, providing a look at its electronic band structure. The incident beam, generated by a synchrotron photon source, is generally hundreds of microns in diameter and,

as a result, data from this technique has thus far only been obtained for epitaxial graphene on silicon carbide (EG). (Various graphene materials will be introduced thoroughly in the following section, but for the time being it is noted that most EG samples are a few millimeters in length compared to 10 micron exfoliated graphene samples.) Linear dispersion has been observed for single layer graphene on the polar Si-face of SiC[36–38] and for multi-layer graphene on the polar C-face.[38] Parabolic dispersion and band splitting occurs, as predicted, for $AB..$ stacked graphite, observed in multi-layer epitaxial graphene on the polar Si-face.[36,37] The details regarding the structures of these materials and resulting effect on their band structure will be thoroughly addressed in coming chapters.

2.2.2 2DEG Properties

The linear dispersion relation and ballistic transport unique to graphene are the more exotic physical properties of this material, but perhaps an important characteristic which involves a more familiar phenomenon is its two-dimensional electron gas (2DEG) nature. 2DEG materials have been extensively studied over the past 50 years and their properties are well established. Most of the literature on two-dimensional systems focuses on either theoretical studies of two-dimensional Coulomb gases (systems of "electrons interacting in a strictly two-dimensional universe in which electromagnetic fields are confined to a plane") or experimental studies of structures consisting of metal-insulator-semiconductor heterojunctions.[39] The most common of such structures (and the most technologically well developed) is the metal-silicon dioxide-silicon system. This is the basis for metal-oxide-semiconductor field effect transistors (MOSFETs) used in integrated circuits as building blocks for complementary metal-oxide-semiconductor (CMOS) electronics. Other commonly studied 2DEG systems are layered structures composed of materials with varying band gaps (such as GaAs and AlGaAs) made by molecular beam epitaxy, as well as electrons on the

surface of liquid helium. The common link between all of the above physical systems is that their structure provides a thin layer with relatively defect-free interfaces in which electron transport is confined.

It was long suspected that if a single layer of graphene could be isolated from natural graphite, it would be possible to experimentally justify its addition to the list of 2DEG materials. In November of 2005, this is precisely what happened, as Andrew Geim's group from the University of Manchester and Phillip Kim's group from Columbia University simultaneously published such evidence after determining a method to mechanically isolate single graphene flakes.[8,9] Evidence for the 2D nature of epitaxial graphene shortly followed.[11,12]

It is somewhat intuitive that electrons traveling strictly in two dimensions (without a third dimension to interact with) may have more appealing transport properties, such as higher mobilities and simpler charge modulation. The signature experiment which indicates two-dimensionality is measurement of the quantum Hall effect (for which von Klitzing won the Nobel prize in 1985.[40]) In two-dimensional systems Hall conductivity does not vary continuously, but exists in quantized steps called Landau levels, which are integer multiples of e^2/h. Lanadu levels are observable in 2D systems due to the reduced scattering that electrons experience when they are confined to two dimensions. Landau quantization specifically refers to the cyclotron orbits of charged particles exposed to magnetic fields, thus there are experiments other than measurement of the quantum Hall effect that can be performed to conclusively identify Landau levels. A second technique to be discussed below is far infrared magneto-spectroscopy.

Klaus von Klitzing and his collaborators were the first to measure the quantum Hall effect (QHE) with great precision in their seminal 1980 paper.[40] For all 2D materials studied (prior to graphene), this involved subjecting field effect transistor (FET) devices made from 2DEG materials to liquid He temperatures ($4K$) and

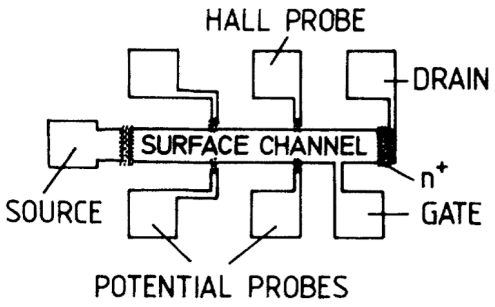

Figure 5: A typical Hall device structure, top view. Taken from [40].

high magnetic fields ($\geq 10T$.) These extreme conditions significantly reduce electron scattering and amplify the effect to make measurement possible. (Although, in 2000 experiments with certain semiconducting materials pushed the upper detection temperature to 30K.[41]) A typical Hall bar device is shown in Fig. 5. As electrons flow lengthwise across the surface channel from source to drain the presence of a magnetic field out of the plane of the page results in a build up of charge and thus a steady state potential difference develops across the width of the channel. In 2D systems the electron's energy levels are completely quantized into cyclotron orbits, whereas a third dimension (the direction of the magnetic field) would allow a more complex electron energy spectrum. Measurement of the Hall voltage should result in a series of steps corresponding to quantized Landau levels.

Initial measurements of the quantum Hall effect in graphene were performed on exfoliated flakes patterned into devices similar to that described above at liquid He temperatures and in high magnetic fields.[8,9] More recent QHE data was obtained in mechanically exfoliated devices all the way up to room temperature (yet still at high magnetic fields.)[41] This novel high temperature work demonstrates the truly unique low-scattering character of graphene.

The QHE has not yet been observed in epitaxial graphene, although Shubnikov-de Haas oscillations at the proper spacing to indicate Dirac carriers have been observed in Hall bar devices.[11] It has been noted that the Shubnikov-de Haas oscillations were

observed more prominently in the poorer quality EG samples, possibly indicating an absence of local defects necessary to observe the QHE in cleaner samples.[42] An alternative measurement confirming epitaxial graphene's 2D nature has been demonstrated by Sadowski *et al.* via far-infrared magnetospectroscopy.[12] This technique measures the far-inrared transmission spectrum at varying temperatures and magnetic field strengths. In epitaxial graphene peaks arise which correspond to Landau level transitions characteristic of a two-dimensional material with Dirac-like carriers. This study was performed on EG samples grown in Georgia Tech's radio-frequency induction furnace and it was observed that as these graphene samples grow in layer thickness, the signature 2D graphene peaks actually increase in strength, rather than reverting to a spectrum characteristic of Bernal stacked graphite. This clearly indicates that multi-layer EG is a very different material than bulk graphite with unique electronic properties. This point will be addressed in further detail later in this thesis, as the crystal structure of this material, found to be responsible for this phenomenon, is a focus of this work.

In conclusion, both exfoliated graphene and epitaxial graphene exhibit clear evidence of electronic two-dimensionality. Both systems are also dominated by Dirac-like carriers. Remarkably, these characteristics have been observed in both systems at room temperature and very recently in EG at low magnetic fields. These exciting results point towards promising potential for epitaxial graphene (which can be grown on a large scale atop SiC wafers) to be used in revolutionary low-power devices as a possible successor to CMOS electronics.

2.3 Various Graphene Systems: Structure

In this section, structures of each of the experimental systems for which graphene has been identified will be described. This includes epitaxial graphene on silicon carbide, mechanically exfoliated graphene and graphene films on transition metals. The focus of this thesis is EG on SiC, so that will be the first system discussed.

2.3.1 Epitaxial Graphene (EG) on Silicon Carbide

As implied in previous sections, the vast majority of research on epitaxial graphene to date has focused on graphene grown on the (0001) and $(000\bar{1})$ polar faces of silicon carbide. It is on these faces that there is an epitaxial match for the hexagonal graphene lattice. For any epitaxial system it is important to be familiar with the substrate material's bulk crystal and surface structure when considering the formation of a thin film overlayer and the interface structure in between. This happens to be particulary true of silicon carbide's surfaces since the growth and character of EG is highly dependent on which SiC face it is grown.

SiC Structure

SiC grows in both cubic and a number of hexagonal polytypes. Most graphene growth on SiC has focused on the hexagonal form. The two commonly used polytypes of hexagonal SiC are 6H and 4H. Their unit cells are shown in Fig. 6. In both cases the cells are composed of Si-C bilayers with different stacking arrangements. For 4H-SiC the stacking is *ABCB..* and for 6H-SiC it is *ABCACB...* The c_{SiC} and a_{SiC} spacings of the 4H and 6H unit cells are given in Table 1. A nH-SiC cell is made of n SiC bilayers. Each bilayer contains a plane of C atoms and a plane of Si atoms. For reference in later sections we define a relative areal density of carbon or silicon atoms, ρ, to be 1 in a bilayer plane (the atom density in a bilayer is therefore $\rho = 2$). The

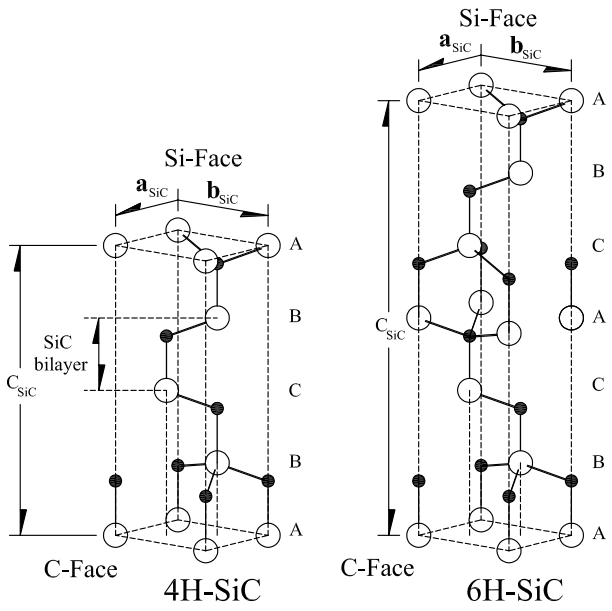

Figure 6: The unit cell structure of 4H- and 6H-SiC. Filled circles are carbon atoms and open circles are silicon atoms.

Table 1: Structural parameters of 4H- and 6H-SiC from [44].

SiC Polytype	a_{SiC} (Å)	c_{SiC} (Å)
4H	3.0805	10.0848
6H	3.0813	15.1198

ideal distance between bilayers for nH-SiC is $(3/4)(1/n)c_{\mathrm{SiC}}$ and the Si-C bond length is $(1/4)(1/n))c_{\mathrm{SiC}}$. There are small vertical relaxations from these ideal spacings that are of the order $(10^{-4})(c_{\mathrm{SiC}})$.[43] For the purpose of graphene growth on SiC, these small relaxations can be ignored.

For graphene growth It is important to emphasize that SiC has two polar faces perpendicular to the c-axis. The bulk terminated SiC(0001) Si-terminated face (Si-face) has one dangling Si bond per Si atom, while the SiC(000$\bar{1}$) C-terminated face (C-face) has one C dangling bond per C atom [see Fig. 6]. As demonstrated in the following chapters, the growth of graphene and the structure of graphene are very different on these two polar faces.

Epitaxy of Graphene on SiC

Because of the relationship between graphene and SiC lattice constants, there are a large number of possible orientations of a graphene lattice that lead to nearly commensurate structures with the SiC(0001) and $(000\bar{1})$ surfaces. Many of these structures are observed in the graphene/SiC system. Which of these structures form depends on the specific SiC polar face chosen for growth along with other experimental conditions. Therefore, these structures are presented in this section as a reference for later discussions. Since both graphene and SiC basis vectors will be used, the need to switch between notation to describe the surface periodicity of various supercells will occur. To avoid confusion the periodic supercells in graphene basis vectors will be written with the subscript G, i.e $(n\times m)_{\mathrm{G}}$. Cells in the SiC basis vectors will *not* be subscripted.

In general these commensurate phases can be calculated when an integer multiple of the SiC unit cell is nearly equal to an integer multiple of the graphene unit cell;

$$|n'\mathbf{a}_{\mathrm{SiC}} + m'\mathbf{b}_{\mathrm{SiC}}| \approx |n\mathbf{a}_{\mathrm{G}} + m\mathbf{b}_{\mathrm{G}}|\,. \tag{1}$$

where n', m', n and m are integers. For convenience we define the dimensionless distances $R_{\mathrm{G}} = \sqrt{m^2 + n^2 - nm}$.

In terms of SiC unit vectors, a set of commensurate structures gives rise to both $(l\times l)$ and $(l\sqrt{3}\times l\sqrt{3})$R30 SiC reconstructions when:

$$l \approx \text{Integer} \begin{cases} \frac{a_{\mathrm{G}}}{a_{\mathrm{SiC}}} R_{\mathrm{G}} & (l\times l) \\ \frac{a_{\mathrm{G}}}{a_{\mathrm{SiC}}\sqrt{3}} R_{\mathrm{G}} & (l\sqrt{3}\times l\sqrt{3})\mathrm{R30} \end{cases} \tag{2}$$

The rotation angle of the commensurate graphene sheets, relative to the SiC $n'\mathbf{a}_{\mathrm{SiC}}$ direction, can be calculated for different integer m and n's:

$$\theta(\text{mod. } 60^\circ) = \begin{cases} \cos^{-1}\left(\frac{2m-n}{2R_{\mathrm{G}}}\right) & (l\times l) \\ \cos^{-1}\left(\frac{2m-n}{2R_{\mathrm{G}}}\right) - 30 & (l\sqrt{3}\times l\sqrt{3})\mathrm{R30} \end{cases}. \tag{3}$$

Table 2: A short list of graphene/SiC commensurate structures.

Commensurate SiC Unit Cell	Graphene angle relative to SiC $[00\bar{1}0]$	Strain $\Delta l/l(\%)$	Ref.
$(6\sqrt{3}\times 6\sqrt{3})$R30° Quasi (6×6)	30°	0.15	45–47
$(6\sqrt{3}\times 6\sqrt{3})$R30° Quasi (6×6)	$\pm 2.204°$	0.15	48
(9×9) Quasi $(3\sqrt{3}\times 3\sqrt{3})$	$30 \pm 2.543°$	0.05	49, 50
(5×5)	$\pm 16.10°$	-0.30	49, 51
$(2\sqrt{3}\times 2\sqrt{3})$R30° Quasi (2×2)	$\pm 6.59°$	0.44	49, 52

One structure of particular relevance is the $(6\sqrt{3}\times 6\sqrt{3})$R30° structure that is the predominant reconstruction observed by low energy electron diffraction (LEED) for graphene grown on the Si-face of SiC.[45–47] A ball model of this commensurate graphene structure is shown in Fig. 7. Note the high symmetry points of the graphene lattice relative to the SiC (shaded hexagons). These are points where either a carbon atom in the graphene layer sits directly above an atom in the SiC layer below, or that a SiC atom lies directly below the center of a graphene hexagon. We can define a quasi unit cell that is defined by these high symmetry points. For the commensurate $(6\sqrt{3}\times 6\sqrt{3})$R30°structure shown in Fig. 7 the quasi cell would be a (6×6) SiC unit cell. Many of the nearly commensurate graphene/SiC structures have these high symmetry cites that lead to smaller quasi cells. These cells are mentioned because, as we will see in later chapters, the influence of the SiC substrate/graphene interaction and the graphene-SiC interface structure causes an apparent distortion of the first 1-2 graphene layers so that scanning tunneling microscopy (STM) images often see a surface unit cell that is smaller than the cell measured by diffraction.

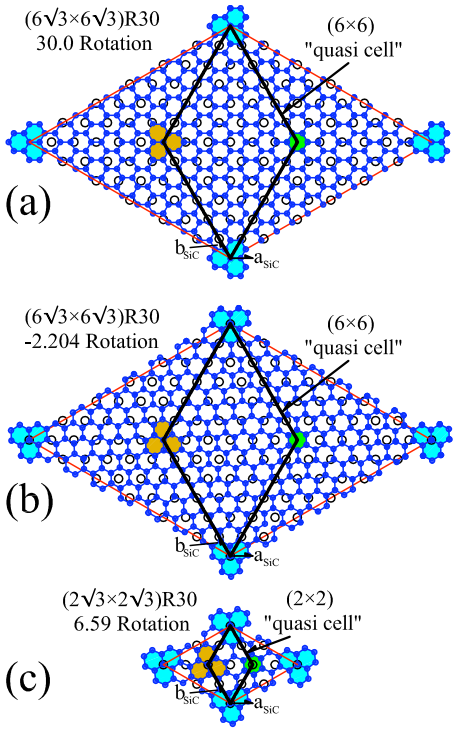

Figure 7: (a) and (b) are two graphene-SiC $(6\sqrt{3}\times 6\sqrt{3})$R30°unit cells, one with graphene rotated 30° and the other with graphene rotated $-2.204°$ relative to the SiC unit cell (red line). Open circles are atoms in the SiC and filled circles are C atoms in the graphene layer. Shaded area shows high symmetry points between the graphene lattice and the SiC lattice. A (6×6) unit cell connecting the high symmetry points is also shown. (c) a $(2\sqrt{3}\times 2\sqrt{3})$R30 cell with graphene rotated 6.59° is also shown with its quasi (2×2) cell.

Table 2 is a short list of these commensurate graphene/SiC structures showing the graphene sheet's rotational angle relative to the SiC $[00\bar{1}0]$ direction along with their relative strain. The strain is defined as $\Delta l/l = 1 - (a_{\rm G}/a_{\rm SiC})R_{\rm G}/l$ or $1 - (a_{\rm G}/\sqrt{3}a_{\rm SiC})R_{\rm G}/l$ for the $(l\times l)$ and $(l\sqrt{3}\times l\sqrt{3})$R30 cells, respectively. These nearly commensurate structures represent a small fraction of the structures possible but are important in that they have been observed in various experiments. A larger group of rotational phases observed for graphene grown on the C-face of SiC will be discussed in Chap. 7. The quasi cells, if they exist, are also listed along side the commensurate structures in Table 2.

This background will be extremely useful when scanning tunneling microscopy (STM) and surface X-ray diffraction (SXRD) data are presented later.

Growing Graphene on SiC

At this point, a brief history and overview of graphene growth on SiC will be outlined, although details about graphene production at Georgia Tech will be covered in Chap. 4. Important structural considerations will also be discussed here, particularly regarding the stoichiometry of graphene growth from SiC substrates.

The pioneering investigations of graphite formation on 6H-SiC(0001) and $(000\bar{1})$ surfaces were performed by van Bommel *et al.*[45] They showed that heating either the C-face or the Si-face surfaces in ultrahigh vacuum (UHV) to temperatures between 1000°C and 1500°C sublimated sufficient Si to leave behind a carbon rich surface. Low Energy Electron Diffraction (LEED) patterns from these surfaces were consistent with a surface graphite structure. They also found a corresponding change in the carbon Auger peak from a "carbide" character to a "graphite" character. Subsequent work showed that that the carbon layers at these temperatures ordered into a graphene structure with clear sp^2 bonding that was aligned with the SiC substrate.[45,47,49,50,53–58] It was also clear from these early works that graphene formation on the two polar surfaces was clearly different.[45,47,53,55] Graphene growth on the Si-face is much slower compared to growth on the C-face.[45,59] In addition, Si-face graphene is epitaxial with an orientational phase rotated 30° relative to the SiC while C-face films can have multiple orientational phases.[45,55] Because of the orientational disorder in C-face grown graphene, most structural, growth and electronic studies of epitaxial graphene focused on Si-face graphene. A major result of this thesis work is that the quality of C-face graphene can be far superior to that grown on the Si-face. In fact, improvements in growth already allow device integration over hundreds of microns.

From stoichiometry alone the formation of a single graphene sheet requires the carbon contained in 3.14 SiC bi-layers $(2/a_{\mathrm{G}}^2)/(1/a_{\mathrm{SiC}}^2) = 3.139$. Liberating this much

carbon requires the removal and subsequent sublimation into the vacuum of Si from more than three SiC bi-layers. This presents a serious challenge because even at temperatures of 1440°C (well above the graphitization temperature), the diffusion of Si or C in bulk SiC is essentially zero.[60,61]

Another stoichiometric consequence of the SiC bilayer carbon concentration is that when Si is removed from the SiC/graphene interface, so that enough carbon has been liberated to form a single graphene sheet, there must be a partial SiC bilayer left at the carbon-graphene interface. We can define the "excess carbon" remaining in the partial SiC bilayer as the amount of surface carbon atoms/[(1×1) SiC cell] after the n^{th} graphene layer has formed but before enough carbon is available to complete the $n^{\text{th}}+1$ layer. In other words, this is an assumption that a graphene layer forms only when the areal density of carbon is equal to the areal density of graphene. While this is obviously not the case since partial graphene layers do form, the "excess carbon" parameter allows us to view the amount of partial SiC bilayers remaining after the completion of an integer number of graphene layers has formed (assuming all the carbon comes from the SiC substrate). A plot of the excess carbon as a function of SiC bi-layers consumed during Si sublimation reveals a periodic minimum every ~ 7 graphene layers. This is demonstrated in Fig. 8. The role of this carbon is unclear. It must play a role in the growth kinetics by affecting the diffusion of Si through the bulk/graphene interface. Due to bonding symmetry differences on the two polar faces, it is expected that the release of Si on these two faces must also be different. Also, since a partial SiC bilayer lead to steps on the surface, achieving a smooth graphene layer-by-layer growth becomes a problem unless the partial bi-layers can be removed by some process.

A thorough understanding of the EG growth mechanism has yet to be achieved, although it is a likely focus of much current experimental and theoretical work.

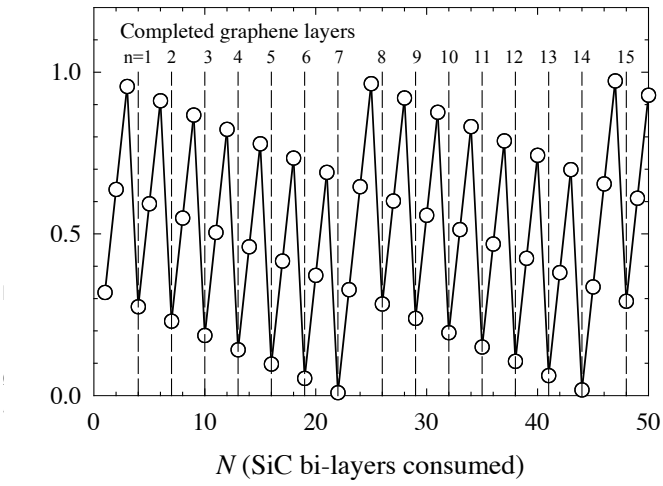

Figure 8: Excess carbon versus the number of SiC bi-layers that have been completely depleted of Si. Dashed lines indicate the number n of integer graphene layers that have been formed after sublimating N SiC bi-layers.

2.3.2 Mechanically Cleaved Graphene

Another extensively studied graphene system is that of mechanically cleaved graphene flakes. This form of graphene has been used as a prototype for studying the properties of an idealized single isolated graphene sheet. While exfoliated graphene is not scalable to device applications, it is still an important physical system and what is structurally known about these systems is particularly relevant as a comparison to epitaxial graphene. It must be realized that exfoliated graphene is far from an idealized isolated system due to processing and the disorder and interactions introduced by laminating them to either a substrate or a support. Even "unsupported" exfoliated graphene[62] starts with a graphene sheet deposited on a substrate that is subsequently chemically etched away. This process will leave a memory of the initial substrate's structure on the sheet's topography. A direct comparison between structural order parameters of exfoliated graphene and epitaxial graphene show that

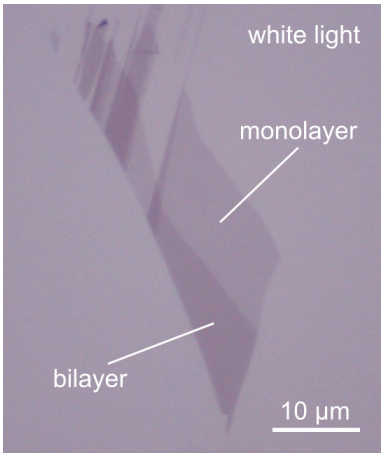

Figure 9: An optical microscope image of an isolated graphene flake. Taken from [64].

exfoliated graphene is in general more disordered.

The process for producing single graphene sheets involves mechanically exfoliating single crystal graphite followed by placement on a SiO_2 substrate.[9] The flakes are exfoliated by mechanically rubbing or are peeled off with Scotch tape, deposited on SiO_2 and searched for using phase contrast optical microscopy.[7,9] An image of such a graphene sheet is illustrated in Fig. 9. Some work has also been done on chemically exfoliating graphene from graphite,[63] but since most transport measurements have been done on mechanically exfoliated flakes, this discussion will be restricted to the mechanically produced flakes.

Transmission electron microscopy (TEM) experiments on unsupported exfoliated graphene sheets have shown that they exhibit a $\pm 5^\circ$ variation in the surface normal.[62] This huge surface mosaic is nearly two orders of magnitude larger than even the poorest SiC grown graphene (a lower bound of 0.06° can be estimated from the graphene rod width measured on Si-face samples via Surface X-ray Diffraction (SXRD.)[65] The huge mosaic angle corresponds to surface height fluctuations of 10Å. As a comparison, the rms surface fluctuation on C-face grown graphene is <0.05Å.[66] The mosaic is most likely due to defects in the graphene caused by either the exfoliation process, the initial substrate roughness or the wet chemistry involved in forming the unsupported

film. Because there are no studies of the chemical contamination in exfoliated films, it is not possible to comment on the role of impurities on the graphene roughness. It is clear however, that the roughness of exfoliated graphene is more endemic and not the sole property of unsupported graphene. The main support for this conclusion is that the rms roughness in exfoliated graphene supported on SiO_2 surfaces is nearly the same as unsupported graphene. Stolyarova *et al.*[67] have used both STM and AFM to measured peak-to-peak height fluctuation of 8Å to 15Å over a 200×200Å area. This should be contrasted to the measured roughness on C-face films that are less than 0.05Å over a 3000×3000Å area.[66] It is clear that exfoliated graphene is not nearly as flat as the 2D films grown epitaxially on SiC.

Another important structural property is the point defect density in graphene. Raman experiments have shown that the D-band peak is absent in both exfoliated[68] graphene (as long as the edges of the sheets are avoided) and C-face epitaxial graphene,,[69] but present in Si-face EG films.[70,71] Since the D-band is known to be sensitive to impurities and defects in the lattice, it can be concluded that the defect concentration is comparably low in exfoliated sheets and C-face EG.

2.3.3 Graphene on Metals

The first monolayer graphene systems studied experimentally (then called monolayer *graphite*) were actually made over 20 years ago by depositing carbon on metals and transition metal carbides. In the early 1980s, studies were published which investigated the formation of graphite overlayers on metal surfaces, such as Ni(111).[72] In this instance, few-layer films were formed on Ni substrates cleaned under UHV conditions and exposed to $10^{-5} - 10^{-6}$ torr CO at elevated temperatures. This work was expanded upon over the years to include isolation of monolayer graphite films on TaC(111), TiC(111), HfC(111) and WC(0001)[73] as well as on Ni(111).[74] In all

cases shifts in graphite's chemical bonds were found, with related expansions (usually $\sim 3\%$) of the graphite in-plane lattice constant. Monolayer graphite (MG) films were also always found to be closely bound to each of the substrates listed; for example, on the Ni(111) surface the interface spacing was found to be 2.11 ± 0.07Å, much lower than the graphite interlayer spacing.[74] It was initially thought that the in-plane bonding shifts could be related to significant charge transfer from the substrates, as in graphite intercalation compounds, however work done by Nagashima *et al.* showed that it was instead a result of rehybridized bonding between substrates and graphene overlayers.[75,76]

With the recent explosion in graphene research, new attention is being given to graphene films on metals. Work on Ni(111) has been revisited and chemical vapor deposition (CVD) growth was compared to unsuccessful attempts to deposit thin graphene films on Si(111) by Obraztsov *et al.*[77] They found that as a result of the far better epitaxial match, Ni surfaces were significantly better for thin film formation. In fact, wrinkles, or "pleats" form in a similar way seen on C-face EG samples (see discussion in Secs. 4.3.1 and 4.3.2.) This particular study did not report on the isolation of monolayer graphene or on the stacking character of their few layer (1.5±0.5 nm) films.

Single layer films have been isolated recently on Ru(0001) surfaces as well.[78] The method used is unique; the carbon needed for graphene formation segregates from impurities present in the single crystal bulk ruthenium wafer. In this study, annealing was performed in a UHV chamber via electron beam heating and graphene formation occurred at a relatively low temperature, 1000 K. STM topographs show the graphene lattice along with a 30 nm period Moiré pattern, explained as a hexagonal superstructure which arises as a consequence of the overlap of the ruthenium and graphene lattices.

Detailed studies of the graphene crystal (and electronic) structure, stacking order,

and interface formation have yet to be performed on these graphene-metal systems. Due to the promising film quality and domain size demonstrated recently,[77,78] further work will likely appear soon.

CHAPTER III

EPITAXIAL GRAPHENE PRODUCTION: EXPERIMENTAL APPARATUS

A number of common surface science techniques are employed during the production and characterization of epitaxial graphene on silicon carbide. This chapter will outline each experimental apparatus used at Georgia Tech and briefly describe its principles of operation. Thorough explanations of the more complex theory behind each technique can be found in the reference materials; the focus here will be with regard to concepts necessary for data analysis of the EG system.

3.1 UHV Chamber

The ultra high vacuum growth and majority of characterization experiments done on epitaxial graphene at Georgia Tech take place in a room temperature UHV chamber.[79] The system, kept at a base pressure of $1\times\ 10^{-10}$ torr, is maintained by a Perkin-Elmer ion pump and a Varian Titanium Sublimation Pump (TSP.) The stainless steel chamber is equipped with a low energy electron diffraction (LEED) apparatus, an Auger electron spectroscopy (AES) apparatus, a field ion microscope, multiple metal evaporators, as well as the scanning tunneling microscope (STM) discussed in detail in Chap. 4. The UHV chamber is shown in Fig. 10 below.

3.1.1 Sample Mount and Transfer

A load lock apparatus enables transfer of two samples and four STM tips from the laboratory into the main body of the UHV chamber. It is pumped down to pressures in the $1\times\ 10^{-8}$ torr range by a Balzer turbomolecular pump backed by an oil-free diaphragm pump. Samples are mounted on molybdenum holders using tantalum strips

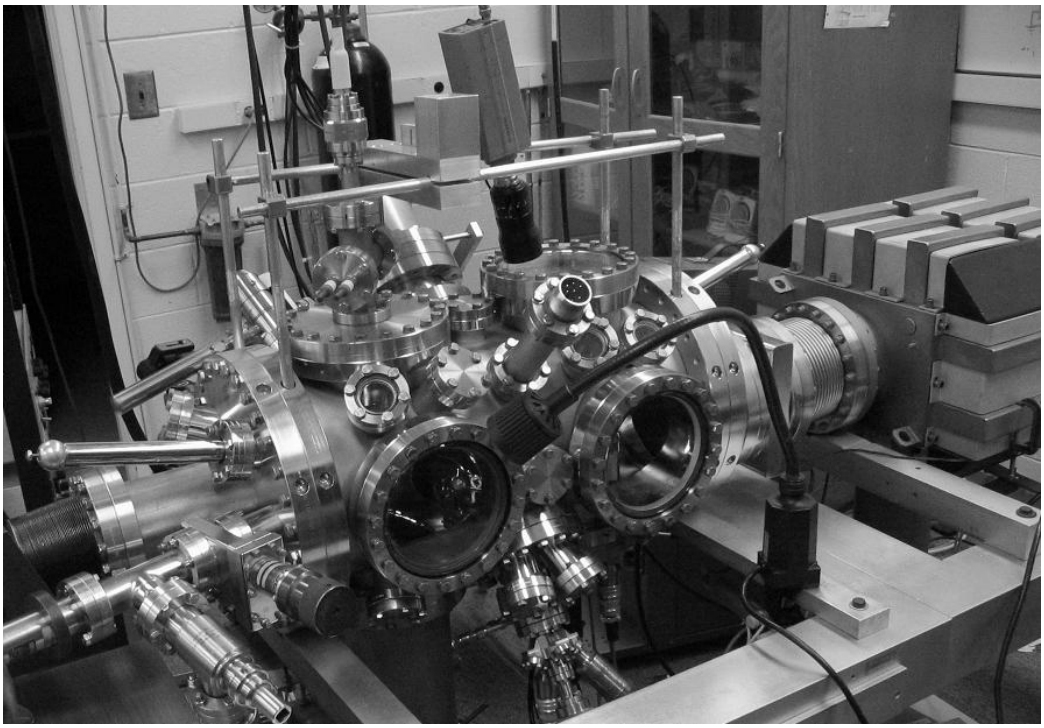

Figure 10: Room temperature UHV chamber.

to pin the sample in place via spot welds. An epitaxial graphene sample mounted in this fashion is shown in Fig. 11. As seen in the photograph, there is usually a hole centered on the molybdenum sample holder in order to expose the sample directly to the electron beam used for heating. The top of the sample holder is designed for easy grabbing with pincers which extend from the two wobble sticks engineered for sample and tip manipulation within the chamber.

Mounted samples are placed in machined slots in the load lock arm (along with any new STM tips ready for transfer) and the load lock chamber is sealed up with either a 3 bolt and Viton seal configuration (for daily use) or a 6 bolt and copper gasket configuration (for main chamber bakeouts.) Once the partitioned load lock chamber is pumped down to the 1×10^{-8} torr range, the load lock gate is opened and the arm is extended into the main chamber via an ex situ magnet operated by the user. One of the wobble sticks is then used to grab the sample (or tip) and transfer it to its respective parking station or to the sample (or tip) heater for experimentation.

Figure 11: Room temperature system molybdenum sample holder. An EG/SiC sample is clamped down by tantalum strips.

The sample manipulator, shown in Fig. 12, houses the heater apparatus and is also used to hold and position the sample for metal deposition, Low Energy Electron Diffraction (LEED) and Auger Electron Spectroscopy (AES) experiments. It is contains one rotational and three translational degrees of motion. The holder itself is fashioned out of 0.5mm tantalum wire (not shown), however a more stable design consists of a molybdenum L-shaped plate bent to just over 90° with a slot cut out for the sample holder. This piece simply attaches to the bottom of the holder block and folds up to the front face of the block at a slight angle which keeps the sample holder safely in place. Either design will work, but the tantalum wire in use now is too malleable to reliably hold the sample in place through the full 360° of motion.

3.1.2 Electron Beam Heater

The sample heater can be seen behind the holder block in Fig. 12. It consists of a homemade tungsten filament and a cone-shaped tantalum foil shield. The sample block itself is held at ground potential and the filament and shield apparatus can be set at a specified high voltage potential. With enough filament current flowing, emission will occur. The sample block and sample holder fit just so the center of the hole on the sample holder is directly in front of the filament. As long as the

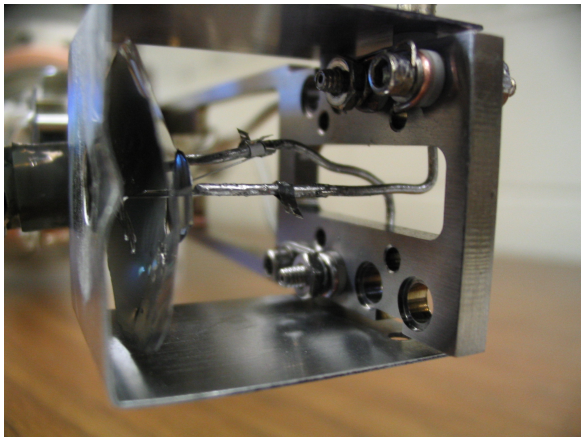

Figure 12: Sample heater on vacuum side of sample manipulator.

sample has been properly centered, it will receive the majority of the electron beam flux and heating will occur. The filament currently being used is 0.05" tungsten wire and is shaped in a standard hairpin geometry. Filament current between $4 - 5.4$ A is generally used for emission. A Thermionics high voltage power supply provides both the filament current and voltage difference between the filament and sample holder/block.

Temperature Determination

Temperature determination of silicon carbide samples under heat treatment proves to be quite difficult. This is because silicon carbide is optically transparent, which results in procedural error as IR and optical pyrometers read the temperature of whatever is behind the sample rather than the sample itself. In our case this is primarily the tungsten filament, which is at a far higher temperature than anything else in the field of view. To date, the best solution for this problem is to ensure that the samples are mounted with sufficient surface area overlapping the molybdenum holder at the sample corners. This allows enough area in the optical pyrometer field of view for a fairly accurate temperature reading. Unfortunately the spot size of the IR pyrometer is too large to focus it fully on such an area, resulting in temperature

readings that are usually 100-200°C higher than optical pyrometer readings.

Another challenge for temperature determination is that SiC forms a eutectic with the material usually used for thermocouples. This prohibits direct contact between a thermocouple and a SiC sample. In the room temperature chamber, a type-K thermocouple is attached to the sample manipulator and is designed to tighten down on the molybdenum sample holder. The resulting thermocouple readings are usually 200-300°C lower than what is read with the optical pyrometer.

Ultimately, temperature calibration on SiC/EG can only be accomplished by comparing observed temperatures for successive stages of growth from the literature with results obtained at Georgia Tech. The optical pyrometer results are consistent within ±50°C of literature values (which can also vary quite a bit.) Extensive detail about the temperatures used to attain all stages of UHV graphene growth on SiC substrates will be given in Chap. 4.

3.2 RF Induction Furnace

To date, EG samples produced by most research groups are made under UHV conditions, in vacuum chambers much like the one described above. As it turns out, the highest quality EG samples are made under low vacuum conditions in a radio frequency (RF) induction furnace. This method for graphene growth was pioneered by Walt deHeer's group at Georgia Tech. The furnace shown in Fig. 13 was used to produce most of the carbon-face samples studied in this work. The main components of the furnace include an AC power supply, a large copper coil, quartz tube, sample stage, and protective shield. The power supply provides alternating current in the middle RF range (200 kHz.) This induces eddy currents in the sample, housed inside the tube and thus generates heat. This method is particularly convenient because it is not localized (as with an electron-beam) and no contacts need be made directly to the sample. The furnace is evacuated by a turbopump but details of the vacuum

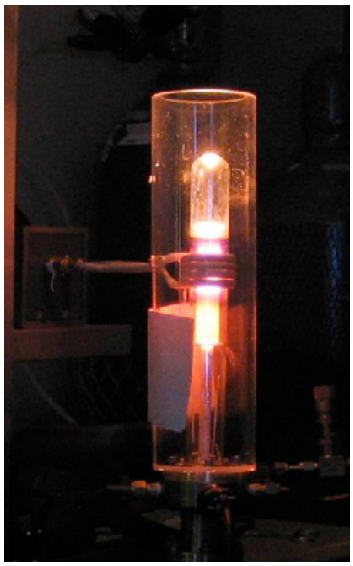

Figure 13: RF induction furnace used for the production of high quality epitaxial graphene.

environment at the sample position are not known because the small furnace volume makes pressure measurements difficult. It is estimated from conductance that the pressure at the sample position is between $P \sim 10^{-4} - 10^{-3}$ Torr. Temperatures are measured with a W Re type-C thermocouple on the sample enclosure. Ambient gases can also be easily introduced into the tube, which may in fact be crucial to attaining the high quality surfaces generated by this method. For this work, samples were prepared by the de Heer group using the equipment described. The reader is referred to the thesis work of Xuebin Li[80] and Mike Sprinkle[81] for further information.

3.3 Low Energy Electron Diffraction

One of the quickest and easiest experimental techniques which has provided a great deal of structural information about the various stages of EG growth is Low Energy Electron Diffraction (LEED.) The RT chamber is equipped with Princeton Research model RVL 6-120 LEED optics, which include an electron gun, phosphor-coated screen and nested set of hemispherical high voltage retarding grids. The optics work in conjunction with Perkin Elmer PHI model 11-020 LEED electronics. This is essentially a control unit which provides high voltage to the grids and screen, as well as

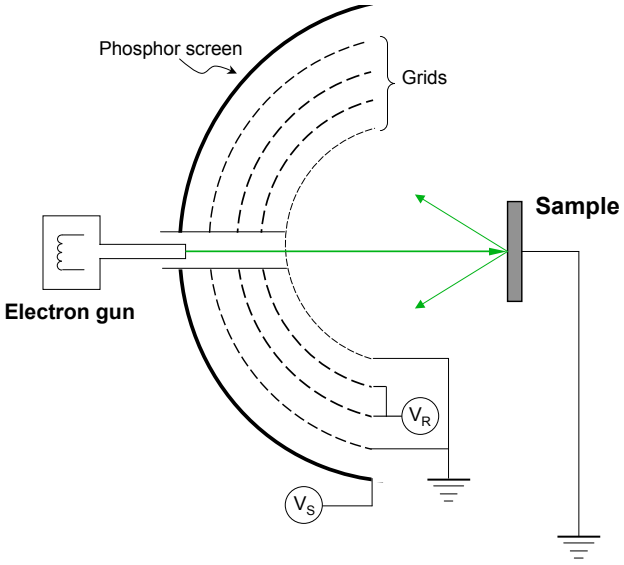

Figure 14: Schematic of LEED optics. Main features are the electron gun, phosphor-coated screen, and hemispherical grids. The sample and first grid are set to ground potential, while the following two grids are set to a retarding voltage, V_R, just below the filament bias. There is one more grid at ground potential before electrons are accelerated to the screen, set at V_S.

providing power to the filament and emmision current. A schematic representative of a general LEED apparatus is shown in Fig. 14.

The electron gun provides the incident beam of electrons (with a range of 0-10 mA emission current) which contact the sample in its position on the sample manipulator. The spot size of the incident beam is approximately 0.5 mm$\times$ 0.5 mm. The scattered electron intensity travels in straight lines through the vacuum, which is maintained as a field free region by setting the first hemispherical grid to ground potential (the same as the sample.) This maintains the original radial distribution of emitted electrons. The following two grids are set to retard all electrons which were not elastically scattered by using a potential, V_R, slightly less than that of the source filament. Finally, the elastically scattered electrons are accelerated towards the screen by applying a high voltage to the screen itself (V_S). This ensures the production of a visible diffraction spot pattern on the phosphor screen.[82] This pattern

is essentially a picture of the surface reciprocal net. The LEED electronics also allow for adjustment of the incident beam energy. Due to the diffracted beam's dependence on the incident wavevector, this results in a scan through the reciprocal net at various "magnifications."

At key stages throughout the sample preparation process, the study of LEED spot patterns provides a quick evaluation of the translational symmetries present on the sample surface. This valuable information with regard to graphene will be discussed thoroughly in Chap. 4.

Principle of Operation The physical realities of electron diffraction make it an inherently surface sensitive technique. It is dependent upon elastically scattered electrons, and its surface sensitivity can be equally attributed to two effects.[82] First is the very short mean free path of inelastically scattered electrons in the typical LEED energy range (20 - 300eV.) This translates to a low probability of electrons reaching deeper atomic layers in a material being elastically scattered back out, as it is likely that much of the incident flux will lose energy and coherence to inelastic scattering. The second issue is with regard to elastic scattering itself. Backscattering is strong and is an inhibiting factor due to large ion core scattering cross sections (which can be as large as 1Å.) Again, the end result is that layers farther from the surface do not see as much incident flux and thus contribute less to the elastically scattered beam. It is generally accepted that LEED experiments can only probe as far as $10-20$Å into a crystal surface. Scattering cross sections for elastic and inelastic processes are similar enough within the typical LEED energy range that the associated effects are both important causes for the technique's surface sensitivity.[83]

Unfortunately, the same phenomena which are responsible for LEED's surface sensitivity also lead to very complex diffraction processes. Highly interactive low energy electrons undergo elaborate scattering events upon entering a crystal, far more so

than the high energy photons used for X-ray diffraction. Kinematic scattering theory (used to model X-ray diffraction via single scattering events) is covered thoroughly in Sec. 5.1.1 of this thesis and is a good starting point to describe electron diffraction, yet a number of adjustments must be made to approach a realistic model for LEED.[83] A thorough description of electron diffraction would necessarily involve a "dynamic scattering theory," the relevant details of which are far beyond the scope of this work. For now it will suffice to list a few of the major physical issues which are corrected for in order to provide a qualitative understanding of the differences between X-ray and electron diffraction.

One of the most obvious modifications is that multiple scattering must be taken into account. This can be achieved by adjusting the atomic form factors to allow for multiple events to occur within the individual atoms. Secondly, attenuation factors must be applied to reflect the short penetration depth of the electrons. Effects of the inner potential, the spatial average of the periodic potential seen by the electron in the crystal, are important and must be accounted for. This correction allows for the band structure of the crystal to be addressed, something not necessary for X-ray diffraction. Finally, the thermal motions of the crystal should be considered as well.[83] In order to use LEED to qualitatively evaluate spot patterns, it is important to keep in mind all of the phenomena mentioned above, although further detail will not be necessary.

3.4 Auger Electron Spectroscopy

Another fast and well-known experimental technique which can provide critical information about the progression of EG production is Auger Electron Spectroscopy (AES.) AES, like LEED, is an electron in, electron out technique. The major difference, as their names suggest, is that with LEED we were interested in elastically

scattered (diffracted) electrons, while with AES we will be looking at an energy spectrum of emitted electrons which have experienced a specific type of interaction with the sample.

Our room temperature Auger apparatus consists of a Perkin-Elmer PHI model 11-010 electron gun & controller, Perkin-Elmer PHI model 10-555 Cylindrical Auger Electron Optics (containing a Cylindrical Mirror Analyzer, or CMA), a Physical Electronics Auger System Control unit, an EG & G Princeton Applied Research lock-in amplifier, and a NIM standard model AEC-315B high voltage DC power supply. The electron gun controller provides the power for the filament current and high voltage needed for the emission of a 1.2mA electron beam incident on the sample. Meanwhile, the Auger system controller modulates the DC voltage applied to the outer cylinder of the CMA via an oscillator contained in the external lock-in amplifier. This allows for the ramping of a specified bandwidth of acceptance energies for the incident electron flux from the sample surface. Thus, the range of electrons that contribute to the collector current is limited, which reduces the already large background signal to a narrower energy range. The electron current from the sample is also enhanced by an electron multiplier contained within the cylindrical Auger optics (but powered by the external power supply.) The AC component output of the electron multiplier collector current is then amplified by the Auger system control and coupled to the external lock-in amplifier. A first derivative of the resulting signal is displayed on a computer monitor.

Principle of Operation An incident electron beam induces excited electron states near a sample surface. The decay of these excited states will often result in electron emission, the Auger process being the most common out of all such events. Auger emission is characterized by three general steps: (1) an atom near the sample surface is ionized (at the core level) by an incoming electron, (2) this core hole is

filled by an electron from a shallower energy level (often at the valence level), and finally (3) the resulting energy release is transmitted as kinetic energy to another shallowly bound electron, which exits the surface.[82] Due to the characteristic binding energies of electrons to host atoms, the energy spectrum of the exiting electrons can be used as a fingerprint for the chemical species present. Traditionally, three step Auger processes are expressed using X-ray level notation. For example, the process we are generally most interested in during graphene formation is the C (carbon) KLL transition.

The energy spectrum of electrons emitted from solid materials consists of a large background with fairly small peaks, therefore Auger data is usually presented as a derivative energy spectrum.

3.5 Atomic Force Microscopy

A brief description of Atomic Force Microscopy (AFM) will round out our discussion of initial characterization techniques. Two AFMs are in operation in Dr. deHeer's laboratory. One is a Park Scientific Autoprobe CP and the second is a newer model, the Digital Instruments CP-II. Most EG samples, particularly those grown in the RF furnace, are imaged with one of these instruments for initial surface characterization. Scan sizes generally range from $5 - 20\mu\text{m}^2$. Vertically, the instrument resolution is about an angstrom and laterally it is dependent on the tip in use (and is usually about 7 nm.)

Principle of Operation AFM imaging can be performed in any of three standard modes: (1) contact mode, (2) non-contact mode and (3) intermittent contact (or "tapping") mode. All use a tip sharpened down to an angstrom-scale diameter that is affixed to the end of a cantilever. Scanning occurs by moving the sample underneath the tip via voltages applied to a piezo-electric tube underneath the sample holder.[84] Contact mode is the simplest of the three methods. A feedback loop based on the

measured deflection of the cantilever as it rasters over a sample surface provides a topographical map of the surface.[85] The downside of this method is that it can often damage fragile sample surfaces as the tip is dragged over delicate features. Non-contact mode is a good alternative, as its name implies. It uses a vibrating cantilever held $50 - 100$Å above the sample surface set at a frequency close to its mechanical resonance frequency. It acquires information about the topography of the surface by monitoring changes in its frequency of vibration due to "force gradients that vary with the tip-to sample spacing."[84]

Almost all AFM images taken on EG at Georgia Tech have been performed using the third mode, "tapping mode", which is essentially a cross between the other two. As in non-contact mode, the tip is vibrated near its resonant frequency, but is allowed to get close enough to the sample such that it actually makes contact at the lowest point of its trajectory. Changes to the tip frequency are again interpreted to attain an image of the surface topography. This method was selected to minimize any potential damage to the surface and also avoid erratic tip vibrations that can occur during non-contact operation. For a more in-depth treatment of the methodology behind tapping mode AFM, see [86].

AFM imaging is an extremely effective way to attain a quick survey of sample surface quality without having to deal with an UHV chamber. AFM results obtained on EG grown on the the two polar faces of SiC exhibit striking differences and will be discussed in the following chapter.

CHAPTER IV

EPITAXIAL GRAPHENE PRODUCTION: PROCEDURES & RESULTS

In the previous chapter all of the laboratory equipment used for EG film formation and initial characterization was introduced. Now, the results attained when these devices are put to work acquiring data on the EG/SiC system will be discussed. Each technique plays its own role in developing an understanding of the character of these unique films.

4.1 SiC Substrates

Due to interest in SiC as a wide gap semiconductor, a great deal of literature exists on both its bulk and surface structure. For reviews the reader is referred to Refs. [52] and [87]. The relevance of any initial SiC surface preparation techniques to epitaxial graphene growth or film quality has yet to be proven, but should nonetheless be mentioned as a topic which could certainly be explored in greater detail. The earlier SiC literature was concerned with producing ordered SiC surfaces with specific structural and chemical stoichiometries. Much attention was given to extensive cleaning procedures and the CVD growth of silicon carbide itself.

4.1.1 Pre-cleaning & Surface Preparation Methods

Current studies use high quality commercial SiC samples (all Georgia Tech wafers have been purchased from Cree, Inc.) and extensive cleaning techniques are not necessary. Even so, surface scratches from polishing remain even in the highest grade SiC wafers. To remove these scratches the samples are hydrogen-etched in either the furnace shown in Fig. 13 or one with a similar design. This procedure starts by

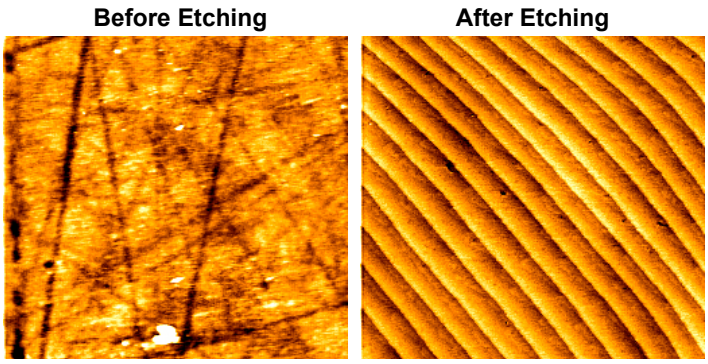

Figure 15: Atomic force microscopy images of 6H-SiC(0001) surfaces as-received (left) and after H_2 etching. Scratches are removed and the surface is left with a stepped structure which is determined by the miscut of the wafer when ordered.

ultrasonic precleaning in acetone and ethanol, followed by hydrogen etching steps that are listed in the literature.[56,88] This usually means etching occurs in an atmosphere of 5% H_2 and 95% Ar mixture at 1 atm pressure. A general furnace hydrogen etching cycle consists of ramping to between $1500 - 1600°C$ at a rate of 100°C/min followed by a 30min soak at 1600°C. The sample is then cooled at a rate $\sim$50°C/min down to 800°C and allowed to cool rapidly down to room temperature. It is important that the samples are cooled slowly after reaching the maximum temperature to remove crystalized Si deposits produced during etching.[89] The H_2 etching treatment leaves a regular atomic stepped surface. This can be seen in Fig 15, where an AFM image of an as-received (Cree, Inc.) SiC wafer is displayed along side a H_2 etched wafer. The difference is dramatic. The step density seen on the treated wafer is determined only by the original sample miscut with the step height usually one unit cell high. Typically terrace widths exceed many microns.

Once H_2 etched, there still remains a problem with surface oxides. Heating the samples to $1000 - 1100°C$ for 6 min in UHV will remove the surface oxide by the formation of SiO gas. This means that the oxide removal also depletes the Si surface concentration. To get around this problem samples can be heated in the presence of

a Si flux ($\sim 10^{14}$/cm^{2}sec for $\sim$ 2min) to remove oxides while preserving the surface chemical stoichiometry.[50,55,90,91] The sample temperature must be kept above 850°C in the presence of the Si flux to prevent the formation of a polycrystalline Si surface and no higher than $900 - 1000$°C to prevent etching. Note that this process allows the removal of O_2 at a much lower temperature than by simply heating. A closer look at effects of these pretreatments on the Si-face SiC structure will be addressed in the following section.

Here at Georgia Tech a few Si-face samples were annealed in the presence of a Si flux, although the process was soon abandoned due to a lack of noticeable difference in graphene film quality. The massive material transport and rearrangement of many SiC bilayers involved at the high temperatures during graphitization make the influence of the details of the starting surface questionable. It is possible that the interface region (between the bulk SiC and the graphene) remains more ordered as a result of Si deposition pre-graphitization, but (1) there is no conclusive evidence for this assertion and (2) it remains unknown how order in interface structure beneath graphene films affects properties of the graphene itself. This is an interesting question for future study, but was not addressed further in this work.

Because the series of reconstructions that form after the pre-cleaning steps are specific to the two polar faces of SiC, the entire graphitization process will be discussed for the Si-face and C-faces separately.

4.2 Si-face Epitaxial Graphene

Growth Phases

Prior to the formation of graphene, the SiC(0001) face goes through a number of surface reconstructions depending on the surface Si concentration. To slow down

Si desorbtion, many groups incorporate a Si flux not only in the pre-cleaning stages, but throughout much of the graphitization process. STM experiments performed by various groups have observed an initial sequence of transitions from $(\sqrt{3}\times\sqrt{3})$R30°, $(2\sqrt{3}\times 6\sqrt{3})$R30°, (3×3) and (7×7) structures as the surface Si concentration is increased.[90,91] LEED studies (both in the literature and in the experiments done for this thesis), on the other hand, have only observed the $(\sqrt{3}\times\sqrt{3})$R30° and (3×3) phases[47,92] indicating that the $(2\sqrt{3}\times 6\sqrt{3})$R30° and (7×7) structures are due to local disorder. It is worth noting that an initial (1×1) LEED pattern has been seen by our group, as well as others, immediately after introduction of the oxidized SiC(0001) surface into the vacuum.[49,80,93] The existence of the (1×1) pattern and its long range order seem to depend on how the original SiC surface was grown and treated. Regardless, this oxidized surface transforms to the well documented $(\sqrt{3}\times\sqrt{3})$R30° after heating above 1050°C, consistent with the $(\sqrt{3}\times\sqrt{3})$R30° being a Si depleted surface.[49,80,94] Whether or not a Si flux is used, heating above 1050°C results in a well defined $(\sqrt{3}\times\sqrt{3})$R30° phase, further heating above 1100°C causes a mixture of $(6\sqrt{3}\times 6\sqrt{3})$R30°and $(\sqrt{3}\times\sqrt{3})$R30° phases to develop. Continued heating above 1200°C results in only the $(6\sqrt{3}\times 6\sqrt{3})$R30°pattern (diffraction spots unique to the $\sqrt{3}$ structure are extinguished.) This is the precursor structure before graphene forms.

Due to the substantial substrate roughening which occurs on this face during graphitization, research has been done investigating the effects of various substrate pre-treatments. Starke *et al.*[95] have done a detailed comparison of the 4H SiC $(\sqrt{3}\times\sqrt{3})$R30° surface prepared via three different techniques:

1. Heating an ex situ prepared hydrogen etched sample in UHV for 30 min at 950°.

2. Preparing the silicon rich (3×3) in a Si flux phase and subsequently heating the sample for 30 min at 1000°C.

3. Heating the sample between $1000-1100$°C in a Si flux to avoid silicon depletion

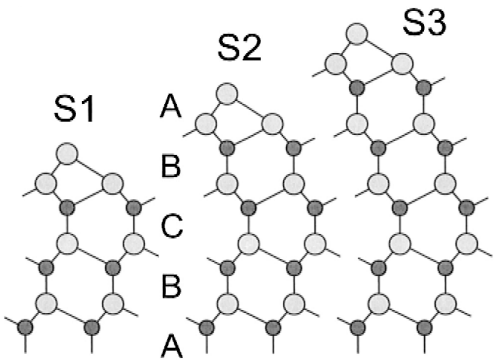

Figure 16: Different stacking terminations denoted as S1, S2 or S3 according to the number of identically oriented bilayers at the surface. Note that the S3 termination breaks the 4H bulk-stacking sequence. Large and bright spheres represent Si atoms, while small and dark spheres represent C atoms. From [94].

of the surface.

These different pre-cleaning procedures ultimately lead to the $(\sqrt{3}\times\sqrt{3})$R30° structure, but with different SiC stacking faults just below the surface.[94,95] The different types of faulted surfaces are shown in Fig. 16. Starke *et al.*[95] assert that the different stacking terminations are seeds for either cubic (S3 termination) or hexagonal (S1 and S2) growth that in turn can influence the degree of surface order. This statement might suggest that: (1) starting from a (3×3) versus a $(\sqrt{3}\times\sqrt{3})$R30° structure or (2) H_2 etching the substrate versus no pre-etching might influence the graphene that is subsequently grown from these different starting surfaces. To date, no clear link has been made between these early preparation stages and the subsequent quality of graphene films grown from them.

The sequence of growth phases seen during UHV sample preparation at Georgia Tech is: (1×1) ⇒ $(\sqrt{3}\times\sqrt{3})$R30° ⇒ $(6\sqrt{3}\times6\sqrt{3})$R30°⇒ graphene. None of the above stages are strictly separated; there is a continuous transition from one to the next and various parts of the sample surface may be at different stages of growth at any given time. Because growth happens quickly and at significantly higher temperatures in the furnace, the sequence of growth phases in that environment has not been monitored.

4.2.1 UHV Production

After the pre-cleaning and pre-graphitization processes described above, the SiC is heated to higher temperatures until graphene forms. The vast majority of the Si-face samples prepared in UHV at Georgia Tech have been made following the (beginning to end) procedure below:

1. Ultrasonically clean in acetone and ethanol.
2. H_2 etch *ex situ* as described in section 5.1.1. (Although this step was not regularly included in earlier years.)
3. Transfer sample into UHV and outgas sample (and holder) at $\sim 600°C$, preferably overnight.
4. E-beam heat to $\sim 1050°C$ to acheive $(\sqrt{3}\times\sqrt{3})R30°$ structure.
5. Continue heating to $\sim 1200°C$ to acheive $(6\sqrt{3}\times 6\sqrt{3})R30°$structure.
6. Heat beyond 1300°C for graphitization, selecting soak temperature up to 1450°C based on desired film thickness.

Heating times were varied without much correlated change in film thickness; soak temperature was far more determinate in final film heights. Standard heating procedures consisted of steady ramping to each of the temperatures in steps (4) - (6) above and holding for approxmately 6 minutes. Flash heating at soak temperatures was also used sometimes, however notable differences in film character were not seen. All annealing was accomplished with the electron beam heater (seen in Fig. 12) and heating was likely localized on whichever portion of the sample was most closely aligned with the filament for a given sample mount.

An understanding of the onset of graphene formation has evolved over the last two decades. In the earliest studies, conducted by Muehlhoff *et al.*,[53] X-ray photoemission spectroscopy (XPS), Auger electron spectroscopy (AES) and electron energy-loss

spectroscopy (EELS) data for both polar faces of 6H and 15R SiC polytypes revealed that the Si/C surface concentration on the (0001) Si-face was very stable up until ~ 1030°C. Above this temperature a "massive surface segregation of C to the surface" occurs. They report features in EELS and XPS data characteristic of graphite at temperatures as low as 900°C and that prolonged annealing at 1170°C increases the graphitic carbon concentration. This is indeed accurate, although recent work has revealed a more detailed series of steps leading to the formation of epitaxial graphene.

Even though graphitic bonds begin forming as low as 1000°C,[91,96] it is generally agreed that a carbon layer with a graphene structure only forms at temperatures above $1250 - 1350$°C.[47,49,93] Graphene grown on the Si-face surface of SiC grows epitaxially, rotated 30° from the SiC substrate commensurate with the pregraphitized SiC(0001) $(6\sqrt{3}\times 6\sqrt{3})$R30°reconstruction [see Fig. 7].[45,47] A LEED pattern from a 1-2 layer graphene film is shown in Fig. 17. The LEED shows a 6-fold pattern from the graphene overlayer, faint integer order SiC rods that are attenuated by the graphene film and a large number of spots (rods) from the $(6\sqrt{3}\times 6\sqrt{3})$R30°reconstruction. Other structures besides the $(6\sqrt{3}\times 6\sqrt{3})$R30°have also been observed in small concentrations, such as the (5×5).[49,51] Riedl *et al.*[51] have shown that the amount of (5×5) present on the surface depends on which of three different preparation techniques (described in the previous section) is used to prepare the substrate.

Surface Character

Initial characterization of graphene film character and quality is achieved by examining LEED and AFM images. AES data is generally used for layer thickness determination, which will be described later in this chapter. Yet, due to a significant change in the C peak shape when a transition is made from carbidic to graphitic carbon, AES can also be used to gauge the onset of graphitization.

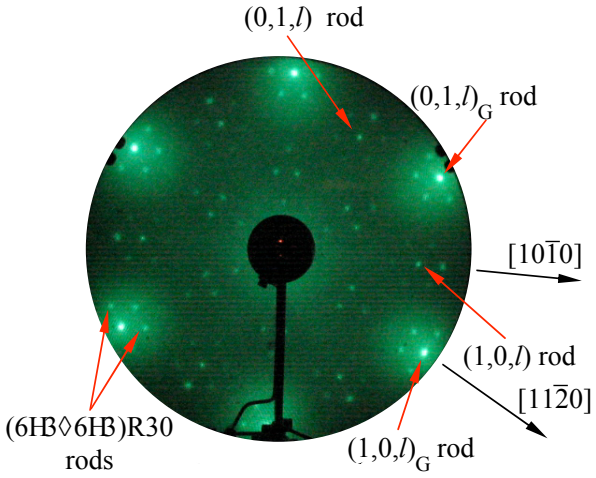

Figure 17: LEED image taken at 69.1eV of a 4H Si-face graphene film (1-2 layers thick) showing the $(6\sqrt{3}\times 6\sqrt{3})$R30°reconstruction. The principle graphene $(1,0,\ell)_{\mathrm{G}}$ rod is aligned along the SiC $[11\bar{2}0]$ direction. Also shown are the SiC rods: $(1,0,\ell)$ and $(0,1,\ell)$. The SiC $[10\bar{1}0]$ direction is shown for reference.

LEED images, such as the one shown in Fig. 17 can indicate a general degree of surface order by the sharpness of the diffraction spots and amount of diffuse background seen. A bright background (which makes diffraction spots hard to distinguish) is indicative of poor surface order. Blurry spots which cannot be focused are also suggestive of smaller domains and possible surface contamination.

AFM images give very straightforward, real space data which provide large scale surface character. A typical image of a graphitized Si-face sample is displayed in figure 18. Even though the starting SiC substrate is composed of uniformly spaced SiC steps, the surface after graphitization is very rough with random steps and deep pits. A review of the published literature shows that the average SiC terrace size after graphitization is no larger than 500Å and more typically 200Å[42,51,97,98] with an rms roughness of 0.17Å.[99] This should be compared to $1-2\mu$m SiC terraces before graphitization. The substrate order (or lack of it) has turned out to be insensitive to surface pretreatment. Using a H_2 pre-etch, a Si-flux to remove the surface oxide or preparing different starting surfaces as described by Riedl *et al.*,[51] all lead to similar terrace sizes as measured by AFM or STM.[42,51,97,98] LEEM studies reach a similar

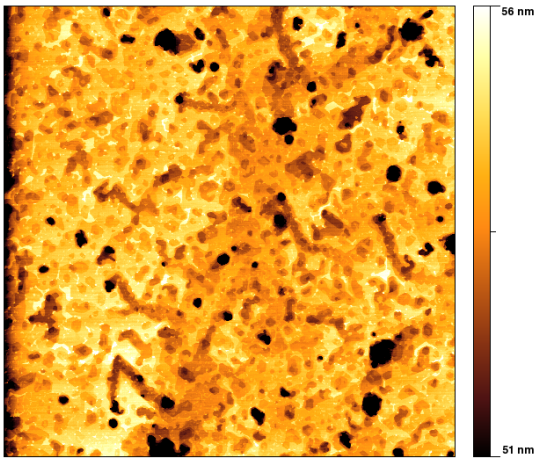

Figure 18: A $10\mu m \times 10\mu m$ AFM image of a 4H Si-face graphene film (1-2 layers thick) graphitized in UHV. Surface pits are common and it can bee seen that the original substrate steps (as seen with a different sample orientation in Fig. 15) have been eaten away.

conclusion.[100]

The good news is that there is an abundance of evidence in the literature (and data taken for this thesis) which shows graphene films growing right over these substrate steps, as a carpet can be laid over a staircase.[97] This also holds true for graphene growing over other graphene sheets.[101] All of the details for this phenomenon will be introduced in Chap. 6, when scanning tunneling microscopy (STM) imaging and characterization is addressed in detail.

4.2.2 RF Furnace Production

Si-face graphene films grown in the RF induction furnace (see Fig. 13) have only recently become a focus of study. Prior to the last year or so furnace growth was heavily focused on C-face films (due to their superior quality and domain size.) The growth parameters are quite different in the furnace than in UHV, however the variation in soak temperature is less dramatic on the Si-face. Generally, the SiC samples are heated to 1200°C for $\sim$ 20min to outgas the furnace and remove surface oxides from the SiC. After this step the furnace is quickly ramped to the graphitization temperature. The thinnest of the Si-face graphene films are grown at soak temperatures of

$\sim 1430°$C and are an average of 1-2 layers thick. There is still a portion of the surface that remains un-graphitized, as commonly seen with thin films grown in the UHV environment, but it is always a far smaller portion of the surface area. Thicker films (up to 10 layers) have been grown at temperatures up to $\sim 1475°$C. Further detail about Si-face furnace growth can be found in the thesis work of Mike Sprinkle.[81]

Surface Character

Graphene film quality is greatly improved when a low-vacuum furnace environment is used. LEED images show an essentially identical diffraction pattern to that seen in Fig. 17, indicating that the $(6\sqrt{3}\times 6\sqrt{3})$R30° interface structure is also formed during furnace growth. One difference in LEED images is that furnace grown films consistently exhibit sharp spots with low diffuse intensity. The reason for this becomes clear when AFM images of Si-face graphene surfaces grown in UHV and the RF furnace are compared. A typical scan taken from one of these furnace grown samples is shown in Fig. 19. As seen, the substrate pits that plague UHV grown samples (Fig. 18) are now absent. The substrate steps present in the pre-graphitized SiC are still intact, however evidence of step bunching and reformation of step edge geometry and orientation can be seen. Perhaps most striking is the appearance of new "tiger stripe" structures which form perpendicular to the step edges. The origin and composition of these novel features is not well understood, although (as will be discussed later in Sec. 6.2.1) the current belief is that they are comprised of an amorphous carbon material.

STM studies of this surface indicate that larger graphene domains and lower densities of in-plane atomic defects are found. This will be discussed further when STM is addressed in detail (Chap. 6.) For a more thorough treatment, the reader is referred to the thesis work of Nikhil Sharma.[102]

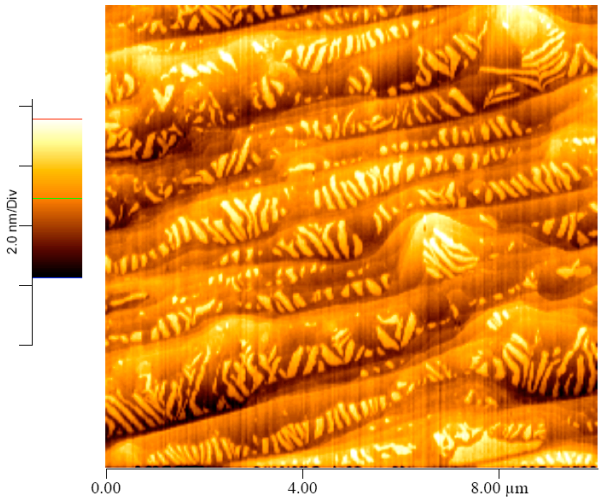

Figure 19: AFM image of a 4H Si-face graphene film (1-2 layers thick) graphitized in a RF induction furnace. Original substrate steps can still be seen and new "tiger stripe" structures are abundant. The substrate pits and roughening are greatly reduced from what is observed in UHV grown Si-face films

4.3 C-face Epitaxial Graphene

As seen in the previous section, there are significant differences between Si-face graphene grown under UHV and furnace conditions. This distinction pales in comparison to the contrast seen on the C-face films grown in these two environments. Vast differences in sample quality and film character are seen when the growth method is varied on the polar C-face termination. These differences are outlined below.

Growth Phases

There have been far fewer studies of the SiC C-face than the Si-face, however, samples have been prepared with a number of different pretreatment procedures. Samples that were only H_2 etched prior to introducing them into UHV have a SiO layer with a $(\sqrt{3}\times\sqrt{3})$R30° reconstruction.[80,103] Heating this surface in UHV leads to a number of different reconstructions cited in the literature: heating to 1050°C for 15 min removes the oxide and gives a (3×3) reconstruction,[104,105] continued heating to 1075°C produces a $(2\times2)_C$ phase in coexistence with the (3×3) phase.[103] The

subscript "C" is used to distinguish this phase from a $(2\times2)_{\mathrm{Si}}$ phase that is formed by depositing Si on a graphitized C-face surface at 1150°C.[103] Seubert et. al[106] have determined the prominent stacking sequences for well annealed 6H C-face surfaces with the $(2\times2)_{\mathrm{C}}$ reconstruction. While well annealed Si-face samples with a (3×3) phase break the hexagonal stacking (S3) in a majority of the domains, the C-face prefers to maintain the S1 hexagonal stacking shown in Fig. 16.

Other groups remove the initial surface oxide while preserving the substrate order by heating in UHV to $\sim$ 850°C in the presence of a Si flux[55,91] or a Ga flux.[91] The initial (1×1) pattern transforms into a (3×3) reconstruction following these treatments.[55,104] When heated above ~ 1050°C the (3×3) structure transforms to the $(2\times2)_C$ reconstruction.[55,107] A number of groups have studied the effects of Si surface concentration on the pre-graphitized surface reconstructions. The (3×3) can be transformed into a $(\sqrt{3}\times\sqrt{3})$ by heating at 950°C in the presence of a Si flux.[49,50] Reannealing to 850°C reversible transforms the surface back to (3×3) structure.

The structures of these different reconstructions are not completely understood. It is generally thought that the $(\sqrt{3}\times\sqrt{3})$ structure is due to Si adatoms absorbed on T_4 sites of the carbon surface.[49,50,108] This explanation is consistent with XPS results that show surface carbon enrichment (i.e the loss of Si atoms) begins at $600-1000$°C on the C-face.[53] The Si adatom model also explains why a Si flux is necessary to maintain the $(\sqrt{3}\times\sqrt{3})$ structure when the surface is heated above 600°C. The $(2\times2)_{\mathrm{C}}$ structure is also thought to be made of Si adatoms.[106] Instead of T_4 sites, the Si atoms lie in H_3 sites but with a lower density than the silicon in the $(\sqrt{3}\times\sqrt{3})$ structure..[106]

4.3.1 UHV Production

There have only been a handful of attempts to grow graphene on the C-face in UHV at Georgia Tech over the past five years, due to the vast superiority of films grown in the RF furnace. In any case, some data was taken on the few samples which actually

exhibited crystal structure (rather than amorphous carbon mounds, another observed outcome.) Consistent with reports in the literature about the growth of UHV grown C-face films, graphene formation occurred at much lower temperatures than on the Si-face. Onset of graphitization was at approximately $1150 - 1200°$C. Annealing procedures closely mimicked those described for the Si-face films (see section 5.2.1) although the temperatures used in steps (4) - (6) were lower, usually 1000°C, 1100°C, and $\geq 1200°$C as a range for final soak temperatures. The sequence of reconstruction patterns was not carefully monitored on this face, although there is no reason to believe that they would be different from those seen by other groups in the absence of an Si flux during annealing.

Surface Character

Unlike Si-face EG, C-face EG is not strictly epitaxial. A typical LEED image from one of the UHV grown C-face EG samples (taken 12° off-axis) is shown in Fig. 20. It is immediately evident that rotational disorder is present in the graphene, due to the existence of diffuse intensity seen as an almost continuous ring at the graphene diffraction rod radius. There are clearly peaks in this intensity at positions rotated 30° and $\pm \sim 15°$ from the SiC $(0, \bar{1}, \ell)$ rods. Note that the only graphene rod position for Si-face films is the 30° rotated position, seen in this image labeled as the $(1, 0, \ell)_{\mathrm{G}}$ graphene rod. (This can bee seen in Fig. 17 as well.) This characteristic diffuse-arc graphene pattern has been observed by all groups that have published diffraction data on C-face EG samples.[38,107] Until the stacking of C-face furnace grown EG films was studied, (a major focus of this thesis work) it was largely assumed that these diffraction patterns were a result of small AB... stacked graphene domains rotated at random angles from one another. This disorder was undesirable, and in search of single crystal epitaxial growth, groups generally moved away from this C-face material and focused on Si-face films.

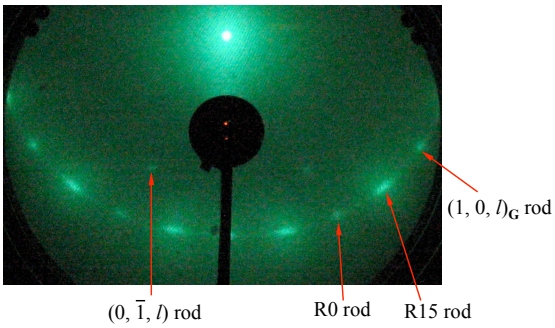

Figure 20: LEED image acquired at 54.6 eV from a 4H-SiC($000\bar{1}$) UHV grown C-face sample with ≤ 5 graphene layers. The graphene and SiC spots are visible and diffuse arcs are labeled as R0 and R15 rods.

Recent work done by Varchon *et al.*[109] provides some of the best real space imaging of typical domains found on UHV grown C-face graphene. To date, the only type of imaging published on these films are scanning tunneling microscope (STM) topographs. An image of a typical UHV grown C-face EG surface is shown in Fig. 21. Even in this relatively small field of view, a large amount of disorder is seen in the graphene film. The surface is covered with pleats, labeled with a "P" in this image, which rise up out of the graphene and are assumed to be tube-like all-carbon structures. Note the enormous height of these features, usually between $5 - 20$Å, far larger than a graphene layer spacing.[109] In addition to the pleats, series of beaded structures labeled with a "B" are also seen. These have been identified as the characteristic beading typically seen in grain boundaries formed between adjacent domains. The frequent presence of both "P" and "B" features are symptomatic of the high degree of disorder found in these films.

The challenge of growing large graphene domains in UHV on the ($000\bar{1}$) face proved too great to sustain further interest in this material. This makes sense in light of the improved order on UHV grown Si-face films, but will be even better understood when comparisons are made with the furnace grown C-face films discussed below.

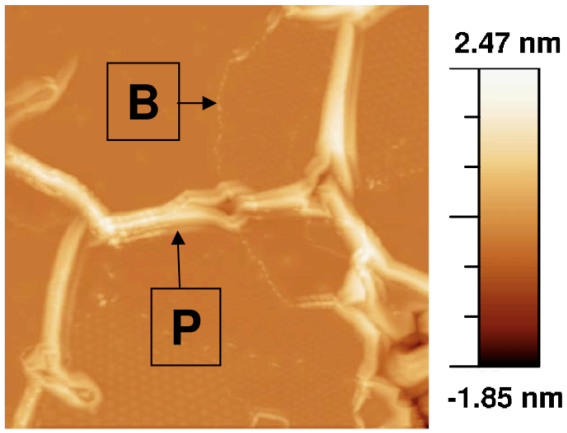

Figure 21: 150nm × 150nm scanning tunneling microscopy image acquired on a UHV-grown 6H-SiC(000$\bar{1}$) EG sample taken at 1.0V sample bias and 0.1 nA tunneling current. Pleat (P) and bead (B) structures are indicated, as discussed in the text. Taken from [109].

4.3.2 Furnace Production

The RF furnace growth has been heavily focused on the C-face material ever since the furnace was developed. As discussed for the Si-face graphene, the SiC samples are heated to 1200°C for ∼ 20min to outgas the furnace and remove surface oxides from the SiC. The furnace is then quickly ramped to the graphitization temperature, which is a minimum of 1420°C on this face. This temperature is almost 300°C higher than the minimum graphitization temperature required to grow C-face graphene in UHV. The graphene film thickness can be controlled by both the growth temperature and growth time. At 1420°C a 4-5 layer graphene film forms in ∼6min. This relatively fast growth rate means it is difficult to produce very thin graphene layers because the thermal mass of the furnace prevents rapid temperature control.

During the past five years, two students were primarily responsible for managing the growth of samples in the RF induction furnace; Xuebin Li and Mike Sprinkle. The design of the RF furnace evolved slightly when the responsibility for sample preparation passed from one student to the other, therefore slight differences in the surface character will be explored accordingly.

Surface Character

The quality of the graphene grown by the furnace method is exceptionally good. Figure 22 shows an AFM image from a furnace grown 10-15 layer graphene film on the 4H-SiC C-face. Unlike UHV grown films, the furnace growth method for C-face films nearly preserves the pre-graphitized substrate step density (typical SiC terrace widths are $>1\mu$m.) The bright lines running through the AFM image in Fig. 22 are not cracks or grain boundaries in the graphene film. They are most likely graphene pleats due to the thermal expansion difference between graphene and SiC as the samples are rapidly cooled after graphitization. These pleats are similar to those seen in Fig. 21 on UHV grown C-face graphene films but are far less prevalent. It should be noted that such pleats have also observed in graphene grown on Ni surfaces.[77] The fact that these pleats run continuously over many SiC steps indicates that the furnace grown C-face graphene films are likely to be continuous over very large distances ($>9\mu$m). It should be noted that these features could also be tubes that form during growth, as there is not yet conclusive evidence either way. It is also possible that *both* pleats and tubes form on the C-face material.

The stark contrast in graphene quality between C-face films grown in an RF furnace and in UHV cannot be overstated. The quality of the samples is such that point defect densities (i.e. missing atoms or impurities) in these films can be difficult to estimate. Raman spectroscopy offers sensitivity to these defects through a higher order scattering process over a beam size of 10-100μm.[68,110] In particular the D-band near 1350cm^{-1} is known to be sensitive to impurities and defects in the lattice. Raman experiments on furnace grown C-face epitaxial graphene conclude that the D-band is absent[69] indicating that the defect concentration in these films is very low.

While most of the SiC C-face surface preparation techniques described earlier have little or no effect on the quality of the graphene films grown on the C-face, the H_2 pre-etching process does. Even though a comparison of H_2 etched and unetched

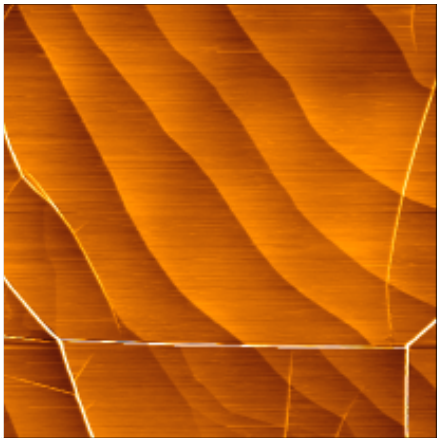

Figure 22: A $9\mu\text{m}\times9\mu\text{m}$ AFM image of a 10-12 layer graphene film grown on the SiC$(000\bar{1})$ C-face in a furnace environment. Lines are most likely pleats in the graphene similar to those shown in Fig. 21, although far less frequent.

graphitized samples by AFM show no discernible difference in the sample quality, X-ray diffraction detects both a high degree of point-like defects and surface faceting. This is explained a bit more at the end of Chap. 5, when X-ray diffraction data is explained. The C-face furnace grown graphene is the only face and preparation method combination for which extensive X-ray studies have been performed, so it is quite possible that similar effects would be seen on the Si-face.

LEED images can also be examined for evidence of surface structure unique to this material. As with UHV grown C-face graphene, strict epitaxy is not observed. There is something inherent in the interface structure that allows films grown on this face to rotate azimuthally as they develop. LEED images on this polar face again exhibit the absence of diffraction rods associated with an interface reconstruction and show the characteristic diffuse intensity along the graphene radius that indicates rotational disorder.

It is in LEED data that differences in sample character from one furnace design to the next appear. Figure 23 contains LEED images from (a) a representative sample made by X. Li in the older RF furnace and (b) a representative sample made by M.

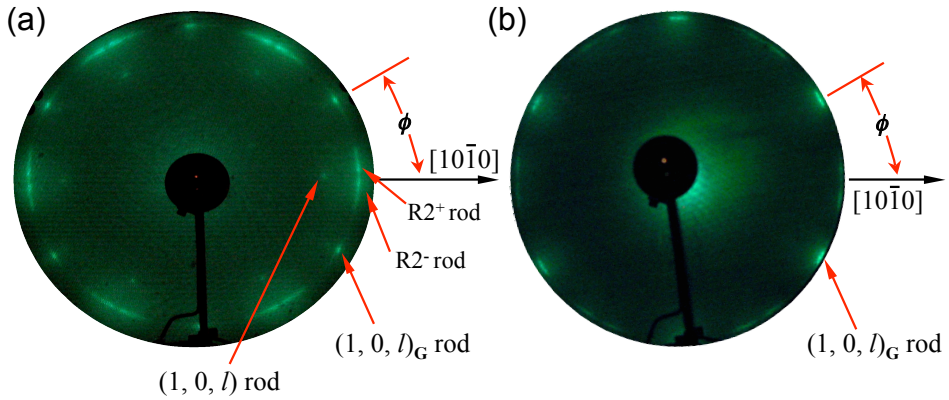

Figure 23: LEED images acquired at (a) 72.2 eV and (b) 72.6 eV from 4H-SiC(000$\bar{1}$) C-face furnace-grown samples with $\sim$5.5 and $\sim$9 graphene layers, respectively. Graphene and SiC spots are labeled, but note that the SiC rods do not appear on the thicker sample. Diffuse arcs are labeled as the R2^{+} and R2^{-} rods in (a) while they remain unlabeled in (b) due to the broader intensity distribution. Image (a) was taken on sample 485, made by X. Li in the older RF furnace, while (b) was from sample 7H3 made by M. Sprinkle in a RF furnace with a new design. The SiC [10$\bar{1}$0] ($\phi = 0$) direction is shown for reference. X-ray azimuthal scans taken along the diffuse arcs on each of these samples are presented in Figs. 45 and 64, respectively.

Sprinkle in the newer RF furnace. A comparison can be made between the rotation angles seen in the diffraction patterns. In both samples a similar intensity distribution is present at the 30° position. (Rotation angles, ϕ, are referenced to the SiC $(0, 1, \ell)$ rods and sweep out in the counterclockwise direction.) Note that the 30° position is also the $(1, 0, \ell)_{\mathrm{G}}$ surface rod. The difference in the data appears near the $\phi = 0°$ position. In (a) the intensity is well focused and symmetric at either side of $\phi = 0°$ with no intensity at the center, whereas in (b) there is a broader, more asymmetric distribution with some intensity present at $\phi = 0°$. A more detailed rotation angle comparison will be made in Chap. 7 when X-ray and STM data regarding this issue are investigated.

Another possible (and maybe more likely) reason for the differences in observed

graphene rotation angles is the miscut angle (and thus step orientation) of the substrate wafer. It happened that, along with the transition from one furnace design to the next, there was also a transition in substrate wafers. Each wafer purchased from Cree, Inc. has a distinct miscut angle, which is responsible for the particular step structure on that wafer. All C-face samples made prior to and including the 400 series wafer (according to the de Heer lab numbering scheme) were made in the older furnace. To date, C-face graphene samples have been grown on more than five wafers, all with different miscut angles. A more careful examination of LEED patterns may result in a correlation between miscut angle and observed rotational domains.

It should be noted that some C-face EG/SiC LEED images have, in rare cases, contained possible interface reconstruction spots. Diffraction rods, other than the $(1 \times 1)_G$ and $(1 \times 1)_{SiC}$, were seen fairly frequently when the earliest C-face furnace grown samples were prepared. A typical LEED pattern seen during this time was used in the Berger *et al.*[11] *Science* publication. Additional spots are located at the $(\sqrt{3} \times \sqrt{3})$ SiC position and could be due to an interface reconstruction of that periodicity. Another possibility is that these spots appear because parts of the sample surface remain ungraphitized. Due to the large spot size of the LEED beam, the signal from any ungraphitized areas could certainly contribute to such a diffraction pattern. On this particular sample, this reconstruction pattern was only observed when the LEED beam was centered on one half of the surface. This, along with the fact that the $(\sqrt{3} \times \sqrt{3})$ reconstruction is characteristic of an ungraphitized surface, makes a strong case that this is not due to an interface reconstruction.

There was one additional case in which another set of diffraction rods was observed. The circumstances were unique, as this particular sample was studied by X-ray diffraction and subsequently peeled with Scotch tape. The goal was to reduce the graphene thickness by mechanically removing the top layers. This was the only instance in which a furnace grown film exhibited a (2×2) reconstruction, similar to

those seen in thin C-face UHV grown graphene films.[107] The conclusion that this (2×2) pattern is an interface reconstruction is consistent with the understanding that furnace grown films are thicker, but can be thinned out via mechanical exfoliation.

The above observations are by and large preliminary and nowhere near comprehensive. There is a lot of interesting future work that must be done to gain further understanding of how and why these C-face graphene rotations form.

4.4 Thickness Determination

To date, there is no standard procedure for absolute determination of the number of graphene layers present on either polar face of SiC. A number of surface analysis techniques have been employed to measure graphene film thickness. While different methods provide pieces of the puzzle, a comprehensive and comparative study to determine what is being measured, the relative accuracy of a particular technique and under what conditions each is applicable has yet to be carried out. In this section an attempt will be made to assess and correlate information from all current methods that have been applied to the problem of determining graphene coverage. As previously mentioned, graphene can be defined both structurally and electronically. Because there is no tool that can provide a complete picture of both these properties, it is critical to use more than one technique in order to make sensible conclusions about the thickness of these films. Techniques used to probe graphene's atomic structure include: SXRD, ellipsometry, LEED and LEEM. Techniques entirely based on electronic band structure measurements are KRIPES and ARPES; capable of probing the type of bonding between atoms. Other techniques like STM, STS, AES, XPS and Raman spectroscopy provide both structural, electronic and local chemical composition.

It must be kept in mind that all of these techniques, with the exception of STM and LEEM, measure properties averaged over the probe beam size. Because graphene

thickness and growth rate are sensitive to temperature, thermal gradients across a sample can produce a lateral height distribution in the graphene film. If the height distribution is wide, an average thickness determined from a spatially averaging probe must be taken with a grain of salt. As a final caveat, measurements of thickness by many of these techniques are heavily dependent on a model of the EG/SiC system and therefore have systematic errors that are dependent on the accuracy of the model. In many cases it has been assumed that the graphene rests directly above a bulk terminated surface. It will be shown in Sec. 5.4.2 that this cannot possibly be correct.

An early method that is still used to determine graphene thickness is AES.[53,54,80] The carbon (KLL) AES spectrum shows a distinct change from C in SiC to C in graphene. This is shown in the insert of Fig. 24. The ratio of the Si(LVV)/C(KLL) peak area can be tracked as the films develop and used as an estimate of the number of graphene layers. Tianbo Li[80] has calculated the Si(LVV)/C(KLL) ratios, including the appropriate inelastic mean free paths and elemental sensitivity factors, for three different models for graphene grown on the Si-face of SiC:

1. The graphene films grown directly on the bulk terminated Si-face of SiC.

2. A Si inferface layer with 1/3 the density of Si in the bulk bi-layer. This was used to represent an adatom layer.

3. The same model as (2) but with C atoms substituted for the Si adatoms.

An important caveat to these estimates is that models (2) and (3) have only about 1/3 and 1/2 of the density of C atoms in the interface layer as determined by SXRD (to be discussed in Chap 5.4.2.) Model (1) does not have *any* C atoms at the interface. This means that AES measurements based on the above models will overestimate the film thickness by $\sim$1 layer because the experimental C(KLL) intensity includes a contribution from additional carbon atoms at the interface. Beyond

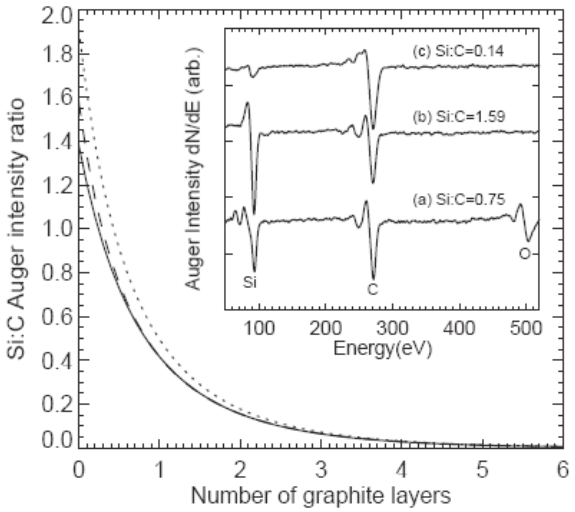

Figure 24: The number of estimated graphene layers versus Auger peak-to-peak ratio of the Si(LVV)/C(KLL) lines for the three models: (I) bulk terminated SiC (dashed line), (II) A Si adatom interface with 1/3 the bulk atom density (dotted line), (III) A C adatom interface with 1/3 the bulk atom density (solid line). The inset shows Auger spectra corresponding to different Si-face reconstructions after heating in UHV. (a) clean surface after H_2 etching, (b) $(\sqrt{3}\times\sqrt{3})$R30° surface after annealed to 1150°C, (c) Graphitized $(6\sqrt{3}\times6\sqrt{3})$R30°surface after annealing to 1350°C.

choosing the appropriate model, there are a number of other factors that must be considered in applying AES to determine graphene thickness. Because the electron penetration depth of the Si(LVV) electron is short, AES estimates becomes very uncertain for graphene layers exceeding more than four layers. This makes the AES method more applicable to Si-face films than to the thicker C-face graphene films. The AES estimate also depends on the growth process. For instance, if the growth leaves an excess of Si atoms on the surface, the AES method is seriously compromised and will underestimate the number of graphene layers. Thickness estimates will be discussed further (and some of these issues will be cleared up) in Chap. 5 when X-ray layer estimates are introduced.

4.5 Growth Kinetics

Little is known about the growth kinetics on either polar face of hexagonal SiC. Ong and Tok[111] have done an STM study of the development of the $(6\sqrt{3}\times6\sqrt{3})$R30°phase

that precedes graphitization on the Si-face of SiC. Starting from the Si-rich (3×3) phase, they follow a sequence of steps involving the formation different Si-clusters that leads to a carbon rich surface. Outside of this study, kinetics information about the growth of graphene must be gleaned from a number of unrelated experiments. This section will outline what is and is not known about graphene growth on SiC.

The growth of graphene appears to be essentially independent of whether or not it is grown from 4H- or 6H-SiC substrates. This is demonstrated in Fig. 25 were the number of graphene layers as a function of growth temperature is plotted for both 4H- and 6H-SiC substrates. This result is a bit surprising since the half-cell stacking fault in the 6H polytype is 3-bilayers compared to 2-bilayer in the 4H polytype. Because the carbon in $\sim$ 3-bilayers is needed to produce a single graphene layer, it would seem that 6H-SiC would be more conducive to a layer-by-layer growth mode. There is some evidence based on AES that graphitization on 4H-SiC appears to start 50°C higher compared to 6H-SiC but relative error bars on both absolute temperature and the graphene thickness measurements make these claims hard to prove.[54] There are, however, fundamental differences in the kinetics between graphene grown on the Si-face and C-face and also between graphene grown in UHV or in a furnace environment. XPS, AES and EELS all indicate that on the Si-face the UHV grown graphene film thickness increases slowly while on the C-face the films grow much faster.[53]

The minimum temperature for the formation of graphitic bonds, as determined by KRIPES spectra, is approximately the same for UHV grown Si-face and C-face graphene ($\sim 1080 - 1100$°C measured by an infrared pyrometer using an assumed emissivity of 0.9).[55] The data in Fig. 25 shows the onset of graphitization occurring at a much higher temperature, $\sim$1350°C. Another interesting feature of UHV Si-face grown graphene is that the number of layers grown is relatively insensitive to the annealing time and seems to only depend on the growth temperature [see Fig. 25]. In contrast, furnace grown C-face graphene depends on both temperature and growth

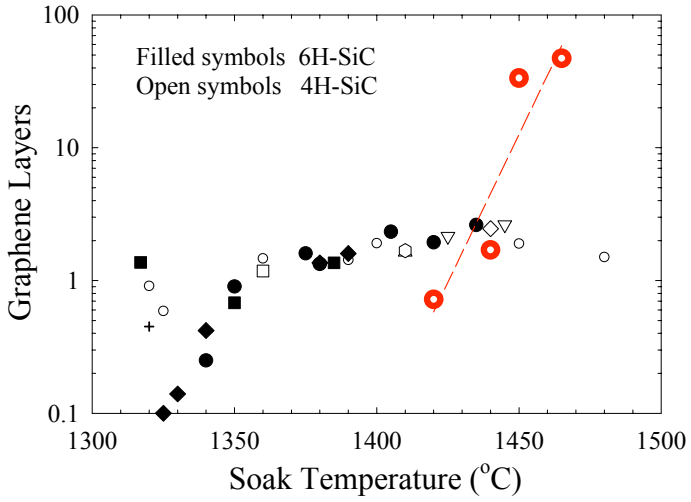

Figure 25: The number of graphene monolayers grown in UHV on Si-face SiC for different soak temperatures as determined by AES (see the previous section for details of the AES estimate). Temperature was measured with an optical pyrometer. Filled symbols are for 6H-SiC substrates and open symbols are for 4H-SiC substrates. Symbols represent different soak times: (◇) 3min, (◇) 5min, (○) 6min, (▽) 7min, (△) 8min and (hexagon) 20min. Red partially filled circles are for furnace-grown graphene on the C-face of 4H-SiC (Thickness determined by ellipsometry). Dashed line is a guide to the eye.

time. Also note in Fig. 25 that the thickness of furnace grown C-face graphene is a rapid function of temperature.

It can be concluded that kinetics at the graphene/SiC interface control the growth of graphene. This follows for a number of reasons. First, there is no significant bulk diffusion at the graphitization temperatures.[60,61] Second, diffusion through the graphene film and sublimation of atoms or molecules containing Si or C from the graphene/vacuum interface must be the same for graphene grown on both surfaces. Finally, there are real structural differences in the interface between SiC and graphene on the Si-face and the C-face (see Sec. 5.4.2) that potentially affect activation barriers for diffusion of either C or Si. While there have been no published experimental investigations of the growth kinetics of epitaxial graphene, there is indirect evidence that suggest a number of kinetic processes that may be key to understanding and controlling the production of epitaxial graphene.

Graphene growth on both polar faces requires diffusion of Si to the vacuum interface were it can be removed. An estimate of Si diffusion through graphite shows that Si can readily diffuse through the growing graphene film at the graphitization temperature.[112] Regardless of the exact mechanism to remove Si from the vacuum/graphene interface, the rate of diffusion of Si, or some Si complex, through the graphene film must be the same on either polar face. These observations point to a Si diffusion limitation at the graphene/substrate interface. To explain the differences in graphene growth on the two polar faces, the removal of Si from the interface must be different for the Si-face and the C-face. This is consistent with evidence from XPS that carbon enrichment at the surface occurs between $600-1000°$C on the C-face, while no significant carbon enrichment is observed on the Si-face in the same temperature range.[53] The slower rate of Si removal from the interface on the Si-face of SiC would also explain the higher surface roughness after graphitization. It is known from studies of SiC growth that on the Si-face excess Si nucleates on the SiC terraces and gives rise to faceting and twinning.[113] Si that is trapped at the graphene/SiC interface would recrystallize as SiC clusters on the SiC terraces that would then nucleate islands that ultimately cause the surface to roughen.

Another important factor in graphene growth is the environment. In Sec. 4.3.2 it was shown that furnace-grown graphene on the C-face grows in very large films with little roughness in the SiC surface. Also, while UHV-grown C-face graphene begins to grow $\sim 100-150°$C lower than Si-face graphene,[47,107] the growth temperature of furnace grown C-face graphene is shifted to higher temperatures. This is demonstrated in Fig. 25. The differences between the growth of graphene in UHV and a furnace environment are not understood. In part this is due to the lack of any detailed knowledge of the furnace atmosphere. Regardless, there is evidence that enhanced Si diffusion occurs in an O_2 atmosphere. It has been suspected for some time from experiments on the growth of CNTs on the C-face of SiC that active oxidation of

Si occurs through diffusion of oxygen to the substrate.[114,115] SiO gas is transported back to the graphene/vacuum interface were it desorbs. Kusunoki *et al.*,[114] using a transmission electron microscope (TEM) equipped with energy loss optics, were able to measure the oxygen K-edge loss feature across the CNT/SiC boundary from thin crossectioned samples grown in a furnace environment at 1300°C. The measurements clearly show an oxide buildup at the CNT/SiC interface. In work done on previously prepared samples which were transported to Argonne National Lab for X-ray diffraction experiments, the production of ozone near the SiC surface, by exposure to X-rays in air produced SiO at the surface of thick graphene films. (This is explained further in Sec. 5.4.4.) This process occurs at room temperature suggesting that ozone rapidly leaches Si from the graphene/SiC interface to the surface.

It has been conjectured that the oxidation of Si at the interface occurs through three possible reaction paths:[114]

$$SiC + \frac{1}{2}O_2(\text{gas}) \rightarrow C(\text{s}) + SiO(\text{gas}) \tag{4a}$$

$$SiC + CO(\text{gas}) \rightarrow 2C(\text{s}) + SiO(\text{gas}) \tag{4b}$$

$$SiC + H_2O(\text{gas}) \rightarrow C(\text{s}) + SiO(\text{gas}) + H_2(\text{gas}) \tag{4c}$$

In all three reactions O_2 gas diffuses to the interface and reacts with the SiC to form SiO gas that can diffuse out of the interface and through the graphene where it can desorb from the surface. These processes are estimated to proceed in the pressure range of 10^{-2}–10^{-6}torr at temperatures between 1200°C-1600°C.[115] SiO gas is also suspected to drive the formation of CNTs on the C-face of SiC by causing the formation of nanocaps either on the SiC terraces or at step edges. The caps form when the partial pressures of SiO at the SiC-substrate boundary exceeds the vacuum partial pressures. This leads to a net force that lifts the graphene from the surface and causes caps or nanotubes to grow.[116] The effect of these oxidation processes is

expected to be very different for UHV and furnace environments. In UHV the partial pressure of these gases is much lower than in the furnace atmosphere and may enhance nanocap formation.

Another consideration is that the vapor pressure of Si in a furnace environments can be relatively high. In a furnace Si may be in near equilibrium with the sample and the furnace walls through either SiO gas or a direct flux of Si atoms that are continually deposited on to and subsequently evaporated from the hot oven walls. There are a number of possible roles that a Si flux can play on the growing film. Bernhardt *et al.*[103] have shown that depositing Si in UHV on a graphitized C-face at 1150°C causes the (1×1) graphene pattern to transform into a Si-rich $(2\times2)_{Si}$ phase. Continued heating of this phase at 1050°C causes the surface to revert back to the pre-graphitized (3×3) phase. This suggests that Si can etch the graphene film. In a furnace environment a high O_2 pressure can oxidize Si deposited on the graphene surface and desorb as SiO gas. This process would prevent substantial diffusion of O_2 to the SiC-graphene interface, thus lowering the partial pressure of SiO at this boundary. Clearly a good deal of work remains before a complete understanding of the the growth of graphene on SiC is possible.

CHAPTER V

SURFACE X-RAY DIFFRACTION ON EPITAXIAL GRAPHENE

5.1 Introduction to X-ray Diffraction

X-ray diffraction has been used for precise determination of bulk crystal structure for almost 100 years. No better technique exists for this purpose, as it is non-destructive, precise and relatively quick. Diffraction occurs because the X-ray wavelength, λ is on the order of the periodic spacing between atoms in a crystal, d, as described by Bragg's law, $2d\sin\theta = n\lambda$. (Here, θ is the angle between the incident X-ray beam and the scattering surface.) Rotating anode X-ray sources are abundant and readily available at most research universities and commercial research labs across the world. These instruments use Bremsstrahlung radiation generated when electrons emitted from a cathode are decelerated at an anode, often copper, tungsten, or molybdenum. Such set-ups are convenient for bulk crystallography and powder diffraction.

Synchrotron radiation provides a more powerful X-ray source, capable of far greater resolution and several orders of increased flux.[117] In this case, the X-ray radiation is produced by a large particle accelerator that incorporates a series of bending magnets and insertion devices to branch the X-ray radiation off into different beamlines. Thin film and surface studies benefit greatly from higher X-ray flux and highly focused beams. The development of synchrotron facilities, scattered across the globe, introduced the high flux X-rays needed to spur development of surface X-ray diffraction (SXRD) techniques in the 1970s.

5.1.1 Kinematic Scattering

X-rays are the ideal weakly interacting investigation tool for crystals. This allows for straightforward analysis using a simple, well developed kinematic scattering theory.[83,118,119] X-ray diffraction directly measures the Fourier transform of the electron density around the atomic nuclei (also known as the auto-correlation function.) Electrons have a far greater X-ray scattering cross section than protons or neutrons, which is why their localized positions are detected. Unlike real space measurement techniques, such as Scanning Tunneling Microscopy (discussed in the following chapter,) diffraction data is taken in reciprocal space, where units are reciprocal lengths. The primitive cell of the reciprocal crystal lattice is known as the first Brillouin zone and unit vectors in reciprocal space (denoted with an asterisk) are related to the real space primitive lattice vectors as follows:

$$\mathbf{a}^* = \frac{2\pi(\mathbf{b}\times\mathbf{c})}{\mathbf{a}\cdot(\mathbf{b}\times\mathbf{c})}, \quad \mathbf{b}^* = \frac{2\pi(\mathbf{c}\times\mathbf{a})}{\mathbf{b}\cdot(\mathbf{c}\times\mathbf{a})}, \quad \mathbf{c}^* = \frac{2\pi(\mathbf{a}\times\mathbf{b})}{\mathbf{c}\cdot(\mathbf{a}\times\mathbf{b})}. \tag{5}$$

Note that $\mathbf{a}\cdot\mathbf{a}^* = \mathbf{b}\cdot\mathbf{b}^* = \mathbf{c}\cdot\mathbf{c}^* = 2\pi$. These definitions will become important later. A great deal of information can be obtained from X-ray data, from inter-atomic spacings and crystal structure to coherent domain lengths and strain evaluation. The methods used to extract such information will be explained below.

Consider an X-ray beam as a collection of coherent monochromatic electromagnetic waves. The incident and scattered wavevectors are $\mathbf{k_i}$ and $\mathbf{k_f}$, respectively. Only elastic scattering will be considered, thus their magnitudes are equal and related to the X-ray wavelength, λ, as follows: $|\mathbf{k_i}| = |\mathbf{k_f}| = 2\pi/\lambda$. The incident wave can be modeled as a plane wave, $\psi \approx e^{i\mathbf{k_i}\cdot\mathbf{r}}$ and in general, is scattered by a scattering center as a spherical wave. However, here two important assumptions can be made: (1) multiple scattering between atoms is negligible (such that the scattered wave only interacts with an isolated scatterer) and (2) the outgoing wave can be considered as a plane wave. This is the first Born approximation. As a result, the fundamental

variable in X-ray diffraction is the momentum transfer vector, $\mathbf{Q} = \mathbf{k_f} - \mathbf{k_i}$.

It is instructive to begin with a simple case, an arbitrary assortment of N atoms uniformly illuminated by the incoming beam. The scattered amplitude, A, can be written as follows:

$$A(\mathbf{Q}) = A_o \sum_i^N f_i(\theta, E) e^{i\mathbf{Q}\cdot\mathbf{r_i}}. \tag{6}$$

Here $f_i(\theta, E)$ is the atomic form factor for the atom located at position $\mathbf{r_i}$. Atomic form factors are specifically calculated according to each atom's electron density and are well known, tabulated functions. Note that scattered intensity increases with the number of electrons associated with a given atom and therefore grows with atomic number, Z. A_o is simply a constant normalized to the flux of the incident beam. This will be set to 1 for most of the following discussion, with a thorough treatment of the relevant experimental constants and variable parameters to come later.

Now, rather than using arbitrary atomic positions, consider a rigid crystal structure. It is customary to define lattice positions using the primitive crystal lattice vectors as follows:

$$\mathbf{r_i} = m_{1i}\mathbf{a} + m_{2i}\mathbf{b} + m_{3i}\mathbf{c}. \tag{7}$$

Here, $\mathbf{r_i}$ represents the set of lattice points, $\mathbf{a}$, $\mathbf{b}$, and $\mathbf{c}$ are the primitive lattice vectors, and the m_ns are integers. Each lattice point is then decorated by a basis of atoms, for which atomic positions, $\rho_\mathbf{n}$ can be defined:

$$\rho_\mathbf{n} = u_n\mathbf{a} + v_n\mathbf{b} + w_n\mathbf{c}. \tag{8}$$

Similar to equation 6, the scattering amplitude can be written:

$$A(\mathbf{Q}) = \sum_{i,n} f_n(\theta, E) e^{i\mathbf{Q}\cdot(\mathbf{r_i}+\rho_\mathbf{n})} \tag{9}$$

and separating sums,

$$A(\mathbf{Q}) = \left[\sum_n f_n(\theta, E) e^{i\mathbf{Q}\cdot\rho_\mathbf{n}}\right] \sum_i e^{i\mathbf{Q}\cdot\mathbf{r_i}}. \tag{10}$$

The term in brackets is defined as the crystal structure factor, $F(\theta, E)$, and is usually the quantity sought after in diffraction experiments. The scattered intensity, $I = AA^*$ can thus be written:

$$I(\mathbf{Q}) = |F(\theta, E)|^2 \sum_{i,j} e^{i\mathbf{Q}\cdot(\mathbf{r_i}-\mathbf{r_j})}. \tag{11}$$

The remaining summation term on the right is known as the interference function, $\Im(\mathbf{Q})$. Now imagine that the crystalline sample is divided up into N_1, N_2, and N_3 unit cells in three orthogonal directions, $\mathbf{x}$, $\mathbf{y}$, and $\mathbf{z}$. The interference function can be broken up along these directions:

$$\Im(\mathbf{Q}) = \sum_{m_{1i},m_{1j}=0}^{N_1-1} e^{iQ_x a(m_{1i}-m_{1j})} + \sum_{m_{2i},m_{2j}=0}^{N_2-1} e^{iQ_y b(m_{2i}-m_{2j})} + \sum_{m_{3i},m_{3j}=0}^{N_3-1} e^{iQ_z c(m_{3i}-m_{3j})}. \tag{12}$$

and, using a key mathematical identity: $\sum_{n=0}^{N-1} x^n = \frac{1-x^N}{1-x}$, each of the three terms in this expression can be simplified as:

$$\frac{(1-e^{iQ_x aN_1})(1-e^{-iQ_x aN_1})}{(1-e^{iQ_x a})(1-e^{-iQ_x a})}.$$

After applying a few trigonometric identities, all three terms can be recombined:

$$\Im(\mathbf{Q}) = \left[\frac{\sin^2(\frac{1}{2}N_1\mathbf{Q}\cdot\mathbf{a})}{\sin^2(\frac{1}{2}\mathbf{Q}\cdot\mathbf{a})}\right]\left[\frac{\sin^2(\frac{1}{2}N_2\mathbf{Q}\cdot\mathbf{b})}{\sin^2(\frac{1}{2}\mathbf{Q}\cdot\mathbf{b})}\right]\left[\frac{\sin^2(\frac{1}{2}N_3\mathbf{Q}\cdot\mathbf{c})}{\sin^2(\frac{1}{2}\mathbf{Q}\cdot\mathbf{c})}\right]. \tag{13}$$

When large values of N_i for $i = 1, 2, 3$ are used (as is the case with any macroscopic sample), each bracketed term is strongly peaked if the $\mathbf{Q}\cdot\mathbf{a_i}$'s are integer multiples of 2π. In an infinite crystal, $N_i \to \infty$ such that these terms reduce to Dirac delta functions:

$$\Im(\mathbf{Q}) = \delta(\mathbf{Q}\cdot\mathbf{a} - 2\pi h)\delta(\mathbf{Q}\cdot\mathbf{b} - 2\pi k)\delta(\mathbf{Q}\cdot\mathbf{c} - 2\pi\ell) \tag{14}$$

and the scattered intensity, $I(\mathbf{Q}) = |F(\theta, E)|^2\Im(\mathbf{Q})$ is zero unless $\mathbf{Q}\cdot\mathbf{a} = 2\pi h$, $\mathbf{Q}\cdot\mathbf{b} = 2\pi k$, $\mathbf{Q}\cdot\mathbf{c} = 2\pi\ell$. These three constraints are called the *Laue condidtions* for diffraction. These conditions are met when:

$$\mathbf{Q} = \mathbf{g_{hkl}} = h\mathbf{a}^* + k\mathbf{b}^* + \ell\mathbf{c}^*. \tag{15}$$

Here $\mathbf{g_{hkl}}$ is a reciprocal lattice vector and $\mathbf{a}^*, \mathbf{b}^*$, and $\mathbf{c}^*$ are the reciprocal space primitive lattice vectors defined in Eq.(5). Thus, maximum scattering occurs at the reciprocal lattice points, which can be directly obtained by the real space crystal lattice structure.

5.1.2 Scattering at Surfaces

The previous section provided a very broad, general explanation of scattering from a 3D bulk material. Now the focus will be on surface scattering. Most surface science techniques, such as LEED (discussed in Chap. 4), get their surface sensitivity from the attenuation of the incident probe due to strong interactions with the material. X-rays, on the other hand, have weak interactions with the material being studied. In order to make an X-ray experiment surface sensitive, one often uses grazing incidence geometry to take advantage of the low Q_z and reduced Debeye-Waller effects. In addition, the scattering is done far from the Bragg points to increase the relative surface to bulk scattering intensity. This targets the top layers of a sample and removes much of the strong background from the bulk structure.

A few adjustments must be made to the kinematic scattering theory when studying surfaces. The treatment of all three crystal dimensions approaching infinite length is no longer valid - at least not for the **z** direction. (It will be assumed that the crystal is oriented such that the surface normal points in **z**.) For the crystal planes parallel to the surface (along directions **a** and **b**), the number of unit cells N_1 and N_2 may still be considered to tend towards infinity. However, perpendicular to the surface, N_3 is now finite. This will affect the expression developed for the scattered intensity, as the $\sin^2$ form in Eq.(13) is not the most appropriate for the truncated dimension (as it will not be converted to a Dirac delta function anymore.) Now, a better expression for the scattered intensity is:[118]

$$I(\mathbf{Q}) = I_o|F(\theta, E)|^2\delta(\mathbf{Q}\cdot\mathbf{a} - 2\pi h)\delta(\mathbf{Q}\cdot\mathbf{b} - 2\pi k)\frac{1-\cos(N_3\mathbf{Q}\cdot\mathbf{c})}{(1-\cos(\mathbf{Q}\cdot\mathbf{c})} \qquad (16)$$

It is clear that the in-plane Laue conditions are maintained; intensity is only observed if $\mathbf{Q} \cdot \mathbf{a} = 2\pi h$, $\mathbf{Q} \cdot \mathbf{b} = 2\pi k$. Therefore, the *surface* reciprocal lattice vector, $\mathbf{g_{hk}}$ must obey:

$$\mathbf{Q}_{\parallel} = \mathbf{g_{hk}} = h\mathbf{a}^* + k\mathbf{b}^* \tag{17}$$

such that the maximum allowed intensity will still occur for all Q_z. This means that rather than reciprocal lattice points that coincide with diffracted intensity maxima, the relaxed condition for the third dimension results in surface diffraction *rods* that rise up perpendicular to the surface. The rod positions in reciprocal space are designated by Eq.(17). This is shown schematically in Fig. 26. The diffracted intensity along the rod is modulated according to stacking features of the crystal planes near the surface and will be affected by surface reconstructions, defects, or substrate steps. Peak intensity will still occur at the third, out of plane Laue condition: $Q_z c = 2\pi\ell$. These diffraction rods are commonly referred to in the literature as *crystal truncation rods* (CTR).

Note that a constant term, I_o was inserted back into the the expression for diffracted intensity, Eq.(16). For X-rays this should include the following factors:[118]

$$I_o = E_o^2 \left[\frac{e^2}{mc^2 D}\right] P \tag{18}$$

This comes largely from the Thomson formula for scattering measured at a distance D from a single electron. e and m are the charge and mass of the electron, respectively. E_o is the electric field intensity of the incident photon and P is the polarization factor for the incident radiation. If the sample is geometrically aligned such that the polarization of the incident radiation is normal to the scattering plane, then $P = 1$. However, if the polarization lies in the scattering plane, then

$$P = \cos^2(2\theta_{pol}). \tag{19}$$

θ_{pol} is defined as the angle between the polarization vector of the beam and the

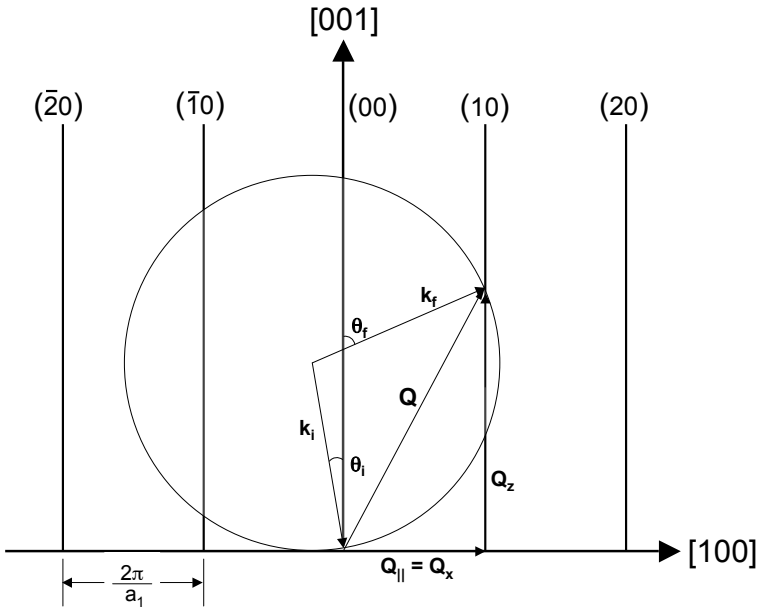

Figure 26: Surface diffraction rods normal to the (Q_x, Q_y) plane. As noted in the text, the rods are separated by $2\pi/a_1$ in the $\mathbf{a_1}$ direction. Diffraction occurs whenever the Ewald sphere intersects a surface diffraction rod at $Q_{||} = 2\pi h/a_1$. Taken from [118].

observation direction.[120] This is important because synchrotron beams are polarized in the plane of the electron orbit.

Additionally, there are geometric corrections that must be considered. These include an active area correction, which evaluates the fraction of the beam footprint incident on the sample, and the determination of the Lorentz factor, a correction that comes about when converting the integration volume from real space to reciprocal space. These will be explained in the appendix. For a thorough treatment, see the work of Vleig.[120]

This section and the previous one should provide enough background to aid understanding of the X-ray experiments performed during the characterization of epitaxial graphene. Later in this chapter, each experimental technique will be described in detail. At this point the X-ray instrumentation used for EG studies will be described.

5.2 Synchrotron X-ray Diffraction

All of the X-ray diffraction experiments performed for this work were carried out using synchrotron radiation at Argonne National Lab's Advanced Photon Source (APS.) The end stations used were the 6ID-B & -C-μCAT (Midwest Universities Collaborative Access Team) beam lines and the photon energy used was always fixed at 16.2 keV. The instrumentation at this facility will be thoroughly outlined in this section.

5.2.1 Advanced Photon Source at Argonne National Lab

The APS at Argonne National lab boasts the highest brilliance X-rays in the western hemisphere. For many experiments the *flux* of the X-ray beam, the total number of photons per second in a 0.1% energy bandwidth, is the fundamental quantity.[121] But, for X-ray diffraction the important quantity is *brilliance*, the "photon flux per unit transverse phase-space area."[121] This is essentially a measure of how tightly a coherent beam can be focused. This is clearly of great importance for surface scattering. Additionally, the APS is capable of producing X-rays on the hard (highly penetrating) end of the spectrum, compared to soft X-ray sources such as the Advanced Light Source (ALS) located at Lawrence Berkeley National Lab.[122]

X-rays at the Advanced Photon Source are produced in five basic stages.[122] Facilities for each stage may be seen in Fig. 27, an aerial photograph of the site. First, electrons are accelerated from a hot cathode in a linear accelerator ("LINAC") using alternating high voltage electric fields. From here, the electrons (already at 450 MeV) are injected into a "booster synchrotron," which uses radio-frequency electric fields and focusing magnets to ramp the electron energy up to 7GeV, with electrons velocities at 99.999999% the speed of light. These relativistic, high energy electrons are then inserted into the much larger storage ring, which has a 1104m (about 7/10 of a mile) circumference. A complex network of bending magnets and insertion devices

Figure 27: An aerial view of the Advanced Photon Source facility. Taken from [122].

(undulators) maintain a well focused electron beam within a circular vacuum chamber track. There are 35 straight segments of this track that are equipped to divert portions of the stored beam for production of the X-ray radiation used at 35 beamlines. Either bending magnets or undulators can be used for X-ray beam production, although undulators are particularly well suited for the focused high brilliance beams needed for surface scattering.

An undulator is made up of a periodic network of dipole magnets with characteristic wavelength λ_u which produce a standing magnetic field.[123] This is illustrated in Fig. 28. When relativistic electrons enter this field they oscillate, and thereby produce radiation. The tighter spacing of the magnets used for undulator design (compared to that of a wiggler insertion device) result in a highly concentrated radiation cone.

The final stage of X-ray beam production occurs when the radiation produced by the undulator enters the experiment hutch at a designated end station. At the μCAT end stations, the (3-40 keV) beam is focused using a vacuum enclosed double crystal Si(111) monochrometer. The first crystal can be oriented to select the correct Bragg angle for a desired beam wavelength such that the outgoing beam is monochromatic.

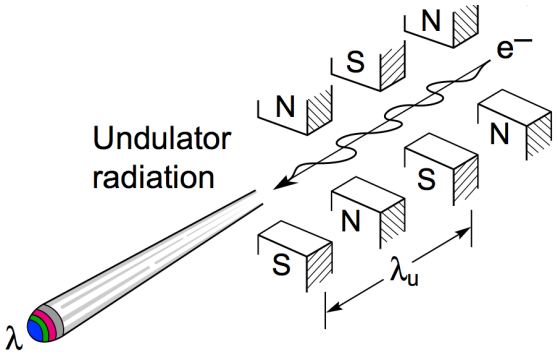

Figure 28: A schematic model of an undulator insertion device. A relativistic electron beam is sent through a periodic structure of dipole magnets. This results in a very intense radiation cone concentrated in narrow energy bands. Taken from [123].

The second crystal reorients the outgoing beam to be in the original beamiline direction. The wavelength and energy selected for all epitaxial graphene experiments were $\lambda = 0.765334$Å and 16.2keV, respectively.

The X-ray beam enters into and travels through both experimental hutches enclosed in a tube filled with gaseous helium to prevent air scattering. For normalization purposes, the beam passes through a series of ion chambers placed both before and after the sample. The ion concentration is controlled by the user and generally fixed for the duration of an experiment. Ion scattering rates monitor intensity fluctuations in the beam that may arise due to mechanical drift or a number of other experimental factors. The monitor that records the diffracted radiation can be normalized using the readings obtained up the beam from the sample. The X-ray beam size can be adjusted in both systems by pairs of horizontal and vertical slits. In most experiments the vertical beam was set at 0.2mm and the horizontal dimension was fixed at 0.4mm.

5.2.2 Instrumentation: μCAT X-ray Diffractometers

All experiments were carried out using two diffractometers located at the 6ID-B & -C-μCAT beam lines. The B station houses an in-air Huber six-circle psi diffractometer. The C-station features a UHV surface scattering chamber that incorporates a six-circle psi diffractometer, as well as LEED and Auger spectroscopy systems. Both

systems will be described below.

In-air Six-Circle Diffractometer

A Huber six-circle diffractometer is used in the 6ID-B endstation. The "six-circle" psi designation comes from the four degrees of freedom available for sample orientation and the two degrees of freedom for detector orientation. This can be seen in Fig. 29. ϕ, χ, η, and μ are angles by which the sample can be rotated, while δ and ν move the detector arm. The sample is carefully aligned such that a central point on its surface is at the center of rotation for all axes. The sample is shown oriented with the scattering surface in the same plane as the beam polarization (not pictured.) This is referred to as "in-plane" sample orientation. Another possible sample orientation involves rotating $\chi = +90°$. This is called the "out-of-plane" sample orientation and is always used with this diffractometer. The choice of sample orientation is largely based on the ability of the stepper motors to rotate to certain parts of reciprocal space that must be covered. Precise angle positions are obtained to within 5/1000 of a degree.

A vacuum sample stage is outfitted with a ~ 6 inch tall beryllium cap in order to maintain a low vacuum ($\sim 10^6$ torr) near the sample. Beryllium is chosen because, due to its low Z value, it has a low scattering cross section. A Displex cryostat can then also be used to cool the sample down below 50K. All data taken for this work was collected using a Cyberstar point detector, outfitted with adjustable guard slits that block out most of the problematic background radiation. Alignment is generally done using a simple photodiode detector.

The majority of the epitaxial graphene experiments described in this thesis were performed in the B-hutch at room temperature, using the apparatus described above. Although the sample was at room temperature, the cryostat was used to cryopump the vacuum within the Be cap, which was almost always used to minimize surface

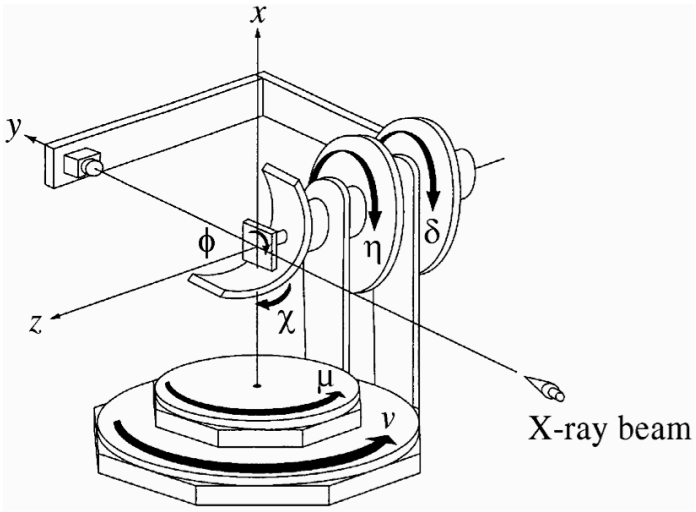

Figure 29: A schematic drawing of the '4S+2D' diffractometer. The sense of rotations, laboratory frame, and incoming X-ray directions are shown as arrows. Taken from [124].

oxides that were found to form during X-ray exposure (see Sec. 5.4.4.) For one set of experiments, including the C-face reflectivity measurement (Sec. 5.4.2) and the first graphene azimuthal scan taken on the furnace grown material (Fig. 45), data was taken in the C-hutch. Therefore, a brief description of that apparatus will be included below.

Surface Scattering Chamber

The 6ID-C end station houses a UHV surface scattering chamber uniquely designed for X-ray diffraction. This system is also equipped with a six-circle diffractometer, as described in the previous section. Here the sample orientation is "in-plane," thus there is no need to account for the polarization factor in the analysis (it is always equal to 1.) The X-ray beam enters and exits the chamber through a large beryllium window, specially designed for this chamber. It is shown in Fig. 30. It allows for a large angular range, providing access to more of reciprocal space. The χ arc here is mounted in vacuum and has a range of 100°. Detection was accomplished using a Bicron point detector with adjustable guard slits. The UHV base pressure was approximately 1×10^{-10} torr.

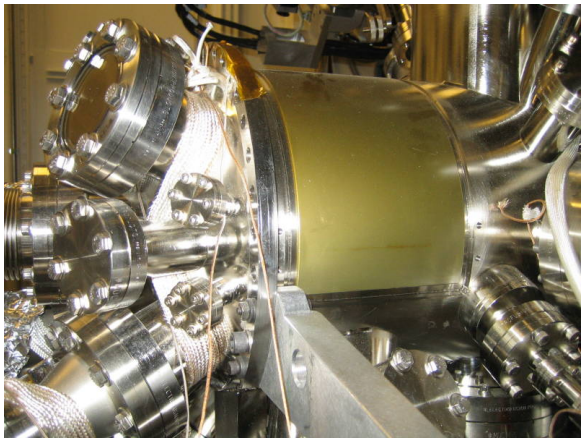

Figure 30: A photograph of the surface scattering chamber highlighting its large beryllium window. The detector arm can be seen in the background. A larger, labeled image of the entire diffractometer can be found in [125.]

5.3 X-ray Diffraction Applied to Epitaxial Graphene

5.3.1 General Model for the EG/SiC System

To bring some coherence to subsequent discussions of X-ray data taken on both Si-face and C-face epitaxial graphene and their respective interfaces with SiC, it is necessary to define a standard model for the graphene/SiC system, along with a few key parameters. This model is the result of a rough consensus of many experiments. It is shown in Fig. 31. It consists of bulk SiC, where the last bulk SiC bi-layer may or may not be relaxed. Black circles represent carbon atoms, open circles represent silicon atoms and grey circles could be either atom type. Between the bulk SiC and the graphene film is a reconstructed interface layer that we will refer to as "layer-0". Although depicted as possibly being up to three layers, this is a bit misleading. The X-ray data, which will be discussed thoroughly in coming sections, consistently fits this "layer 0" with atom densities and layer spacings more reflective of a single corrugated layer or one layer plus an adatom structure. The first graphene "layer-1" is a distance D_o above the topmost atom in the interface layer. D_1 is the spacing between the first and second graphene layers and D_{G} is the average spacing between subsequent layers (note that D_{G} is not necessarily equal to the bulk graphite spacing

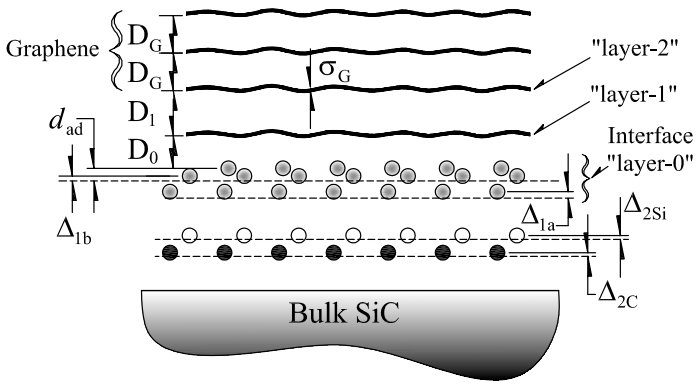

Figure 31: A schematic model of multi-layer graphene grown on the 4H-SiC(0001) substrate. Dashed lines are the bulk SiC lattice planes before interface relaxation (Δ's). The 5^{th} plane of atoms (adatom) is displaced d_{ad} from the topmost atom plane in the interface. ($\bullet$) are carbon atoms and ($\circ$) are silicon atoms. The shaded circles in the interface ("layer-0") can be either carbon or silicon atoms. The graphene layers above the interface layer are referred to as "layer-1", -2, -3, etc. σ_{G} is the rms height variation in the graphene layer.

$c_{\text{G}}/2$). σ_{G} is defined as the rms height variation of a graphene layer, which includes both height variations due to a reconstruction in the interface and any roughness in the graphene film. The SiC substrate roughness (e.g due to steps, etc.) σ_{SiC} is not shown in the figure. Note that the (0001) termination was used in the figure, but the same model and parameters will be used for the $(000\bar{1})$ face. The only difference is that the last SiC bilayer atoms must be reversed.

5.3.2 EG/SiC in Reciprocal Space

Throughout any discussion of X-ray diffraction data it is also helpful to have in mind a simple reciprocal space map of the system. Figure 32 is this kind of schematic for the EG/SiC system. Both graphene and SiC have a hexagonal (2D) Brillouin zone. Depicted in the schematic are open circles, which represent the (1×1) diffraction pattern from an unreconstructed SiC surface and filled, slightly elongated circles which are the $(1 \times 1)_G$ pattern for a graphene film. The graphene structure is rotated azimuthally by 30° ($R30°$) relative to the SiC (1×1) cell. The diffuse ring through the $(1 \times 1)_G$ graphene spots mimics the (1×1) LEED pattern from a graphene film with rotational disorder. The notation $(h, k, \ell)_G$ identifies a reciprocal-space point in units

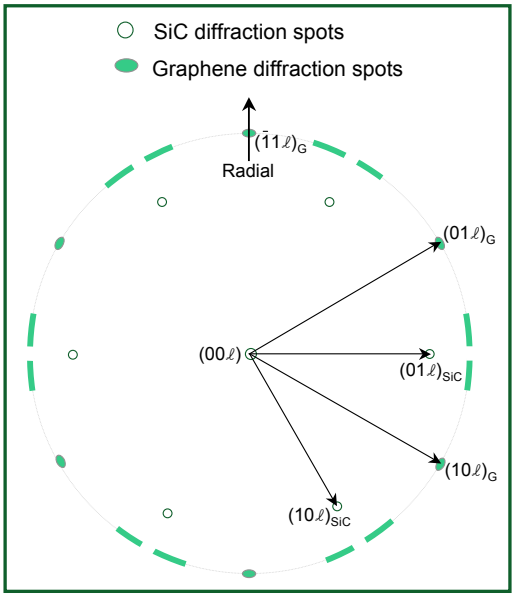

Figure 32: A schematic model of the 2D graphene/SiC Brillouin zone. Open circles represent the (1×1) diffraction pattern from an unreconstructed SiC surface and filled, slightly elongated circles represent the $(1 \times 1)_G$ diffraction pattern for a graphene film. A diffuse ring with peaked intensity is also shown at the graphene radius, similar to what is observed on C-face EG samples. Many of the graphene and SiC surface diffraction rods are labeled for reference.

of the graphite hexagonal reciprocal lattice basis vectors: $a_G^* = 2.9508\mathring{A}^{-1}$ and $c_G^* = 1.8829\mathring{A}^{-1}$. Unsubscripted reciprocal-space coordinates (h, k, ℓ) refer to the substrate 4H-SiC hexagonal reciprocal lattice units: $a^* = 2.3552\mathring{A}^{-1}$ and $c^* = 0.6230\mathring{A}^{-1}$. The measured SiC lattice constants were: $a_{\mathrm{SiC}} = 3.0802 \pm 0.0006$Å, $c_{\mathrm{SiC}} = 10.081 \pm .002$Å for doped samples and $a_{\mathrm{SiC}} = 3.0791 \pm 0.0006$Å, $c_{\mathrm{SiC}} = 10.081 \pm .002$Å for un-doped samples. These are within error bars of published values.[44]

The schematic shown is more representative of the C-face graphene films, as the Si-face films do not have any rotational disorder and sharp graphene spots with a complex reconstruction pattern are seen in the LEED data. Nonetheless, this schematic will be referred to as a general model when both faces are discussed.

5.4 Surface X-ray Dfiffraction on Epitaxial Graphene: Results

5.4.1 Average Domain Size Characterization

Early on in the investigation of epitaxial graphene produced at Georgia Tech, detailed information on the structural order of the samples was acquired by surface X-ray scattering. This was achieved by measuring the width of the graphite $(00\ell)_G$ and $(1\bar{1}\ell)_G$ rods on both RF furnace grown C-face and UHV grown Si-face samples. Figure 33 shows radial scans across the graphene $(1, \bar{1}, 1.5)_G$ crystal truncation rod (for orientation, see Fig. 32) for both the Si- and C-face samples. The Si-face samples have a radial width of $\Delta q_r \sim 0.022\text{Å}^{-1}$ corresponding to a graphene mean coherent domain size[126] $L = 2\pi/\Delta q_r \sim 290\text{Å}$. This is very similar to the graphite domain size observed by Charrier *et al.*[57] and is typical of the quality of graphite grown under UHV conditions on the SiC(0001) surface reported to date in the literature. Although the particular surface treatment used in this study was different from that applied to GT samples, (they applied a Si flux as a pre-treatment during the first heating stage to remove oxygen) the fact that the domain sizes are similar suggests a limit on the graphite quality other than the presence (or lack) of such pre-treatments.

In contrast, graphite grown on the C-face has much larger domain sizes demonstrated by the smaller radial widths in Fig. 33: $\Delta q_r \sim 0.003\text{Å}^{-1}$, corresponding to $L \sim$ 2100Å. So while the LEED patterns show azimuthal disorder in the C-face graphene, the coherent graphene domains are more than 3 times larger than for the Si-face graphene. The C-face Δq_r's do not change for films between 7–13 layers. This improved structural coherence correlates with the much higher carrier mobility measured for C-face graphene compared to that measured on Si-face graphite films.[42] The difference in film thickness may play a role in the long range order of the films. There is also little difference in the long range order of 1-2 layer graphene films on

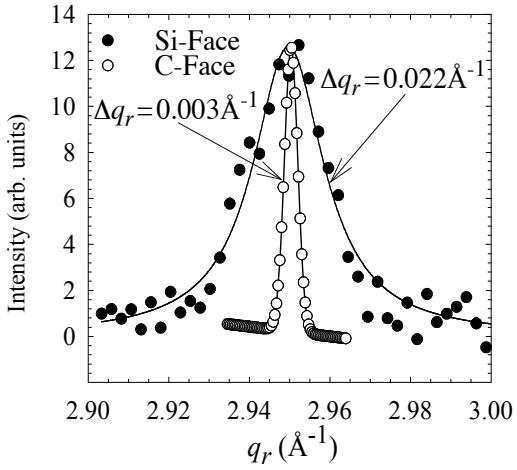

Figure 33: Radial scans through the graphene crystal truncation rod $(1, \bar{1}, 1.5)_G$ for both 2-layers of graphene grown on a UHV-grown Si-face sample (•) and 7-layers of graphene grown on a furnace-grown C-face sample (○). Solid lines are Lorentzian fits.

the Si-face. In addition, growth of 4–5 graphene layers on Si-face requires temperatures above $\sim$ 1450°C where substrate disorder becomes increasingly problematic (see below).

The X-ray data also reveals a dramatic difference in the surface morphology of the SiC substrate after film growth. Transverse scans along the specular (00ℓ) rod were taken on both C- and Si-face graphitized surfaces. The transverse peak widths Δq_t are plotted in Fig. 34 versus ℓ (SiC units). These scans reveal a modulation of the width with ℓ that is very different for the C- and Si-face graphitized surfaces. The peak-width modulation is due to atomic steps.[126] In this case it is due to steps on the SiC substrate and not steps in the graphene. There are two reasons that this must be the case. First, if graphene steps were prominent, this would cause a width modulation of the graphene $(1, \bar{1}, \ell)_G$ rod that is not observed. Second, the modulation period $\Delta\ell$ seen in Fig. 34 is inversely proportional to the step height: $d_{step} = c_{SiC}/\Delta\ell$. For both C- and Si-face samples, $\Delta\ell$ corresponds to half of the 4H unit cell height (5.043Å) and not to the graphene step height (3.337Å) or any

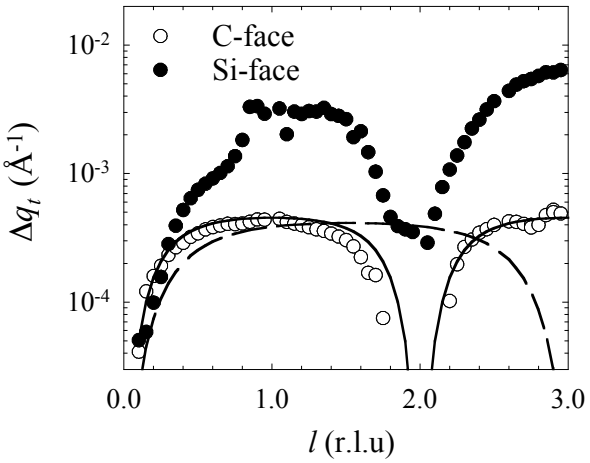

Figure 34: Comparison of the FWHM (Δq_t) of the $(00\ell)_G$ rod vs. $q_z = \ell c^*_{SiC}$ from (•) a 2-layer graphene film grown in UHV on the Si-face and (∘) an 8-layer film grown in a RF furnace on a C-face 4H-SiC substrate. Instrument broadening has been removed for clarification. The lines are fits to a geometric distribution of steps and step heights with either the (solid line) 1/2 4H-SiC step height or the (dashed line) graphene step height.

multiple. This is clearly demonstrated by the fits in Fig. 34. The fits are to a model of a geometric distributions of steps and step heights based on either the half 4H unit cell height or the graphene step height. It is clear that the graphene steps produce the wrong period.

The maximum width in Fig. 34 is inversely proportional to the mean distance between steps on the SiC substrate, D, $D = 2\pi/\Delta q_t$.[126] Because the modulation amplitude is much larger for the Si-face sample, the SiC step density is more than an order of magnitude greater than on the graphitized C-face. The starting SiC step density before graphitization was essentially the same for both samples. This is evidence that the substrate roughening that is quite problematic on the Si-face samples is far less on the C-face furnace grown samples.

Quantitatively, the C-face samples show that the mean terrace width of the SiC substrate is $D_C \sim 1.4\mu m$, while the Si-face samples have a terrace size of $D_{Si} \sim 0.2\mu m$. The higher step densities observed after graphitization on the Si-face substrate correlate with the poorer long range order of the graphite grown on this face. Whether

this is a cause or effect relation is still unclear.

5.4.2 Specular Reflectivity & Interface Characterization

In addition to the investigation of topography differences, there are more fundamental questions related to electron transport in EG films which can be addressed using surface X-ray diffraction. For instance, what can be inferred about the electronic properties of this system and the nature of the bonds involved in the interface region by the atom densities and displacements measured by SXRD? Transport measurements infer[11] and angle resolved photoemission spectroscopy (ARPES) measurements confirm the existence of a Dirac cone in both the band structure of single layer graphene films on the Si-face[37,38] and multi-layer graphene films on the C-face.[38] From a surface science perspective, the preservation of a delicate band structure is unexpected for an epitaxial system chemically bonded to a substrate. One would assume that the electronic structure of the graphene would be strongly influenced by the SiC and/or the interface region. The fact that the linear dispersion and 2D nature of graphene is maintained on both faces is remarkable. The nature of the graphene/SiC interfaces is important to understanding the electronic structure of epitaxial graphene and in turn, crucial to device applications.

Surface X-ray Diffraction is the only technique available which is capable of probing just the *structure* of the buried interface. For this purpose, X-ray specular reflectivity experiments on the structure of multi-layer graphene grown on both UHV grown 4H-SiC(0001) and RF furnace grown 4H-SiC($000\bar{1}$) surfaces have been performed. These measurements occur at the (00ℓ) ("specular") rod, seen in the center of Fig. 32. To date, reflectivity data has been taken on six Si-face samples and eight C-face samples.

Specular reflectivity only depends on the momentum transfer perpendicular to the surface. The data is collected by integrating rocking curves [see Fig. 35(a)] around

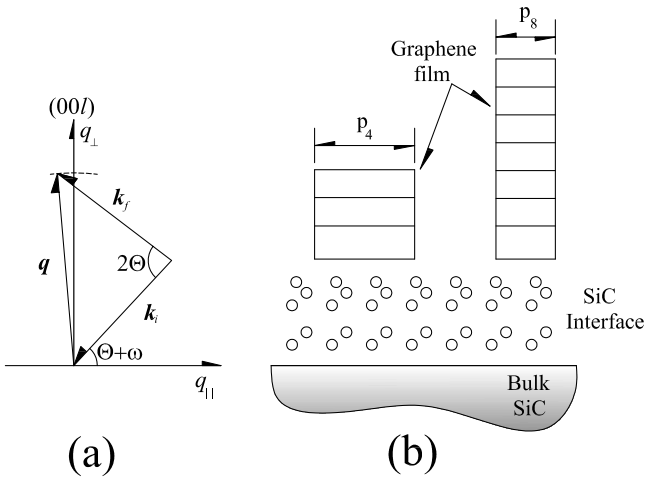

Figure 35: (a) Schematic drawing of the reflectivity geometry. Incident wave $\mathbf{k_i}$ strikes the sample surface at an angle $\Theta + \omega$. The diffracted wave, $\mathbf{k_f}$, is kept fixed at 2Θ from $\mathbf{k_i}$. $\mathbf{q}$ is "rocked" through the (00ℓ) rod by rotating the sample through an angle $\pm\omega$. (b) Model of multi-layer graphene islands grown on a SiC substrate with a reconstructed SiC interface layer. For specular reflectivity, all n-layers islands can be represented as one island with a fractional surface coverage parameter, p_n.

$\mathbf{q}_{\|} = 0$ for different perpendicular moment transfer vectors, $q_\perp = 2\pi\ell/c_{SiC}$, where $\mathbf{q} = \mathbf{k}_f - \mathbf{k}_i$. Since the reflectivity only depends on $q_\perp$, the data can be analyzed using a one-dimensional model where all lateral information is averaged over the 0.4×0.4mm X-ray beam. The scattered X-ray intensity $I(\Theta, \ell)$ is a result of a sum of three scattered amplitudes; the bulk $F_{\rm bulk}$, the interface region F_I, and the graphene $F_{\rm G}$:

$$\begin{aligned} I(\Theta,\ell) &= A(\Theta,\ell)e^{-4\gamma_{\rm SiC}\sin^2\pi\ell/2} \\ &\times \left|\frac{F_{\rm bulk}(\ell)}{1-e^{-2\pi i\ell}} + F_I(\ell) + \frac{\rho_{\rm G}}{\rho_{\rm SiC}}F_{\rm G}(\ell)\right|^2 . \end{aligned} \tag{20}$$

$A(\Theta, \ell)$ is a term that contains all corrections due to the experimental geometry.[117,120] (Also see the appendix of this thesis.) The exponential term accounts for the substrate roughness caused by half-cell step fluctuations in the SiC surface (the predominant step height on 4H samples; $c_{SiC}/2$). $\gamma_{\rm SiC}$ is the variance in the number of half-cell layers in the surface due to steps.[127] Roughly, $\gamma_{\rm SiC}$ is proportional to the SiC

step density. The first term in Eq.(20) is the bulk 4H-SiC structure factor, $F_{\rm bulk}(\ell)$,[43] modified by the crystal truncation term, $(1-e^{-2\pi i\ell})^{-1}$.[119] $F_{\rm G}(\ell)$ in Eq.(20) is weighted by the ratio of the areal densities of a 4H-SiC(0001) and a graphene (0001) plane; $\rho_{\rm G}/\rho_{\rm Si}$=3.132, to properly normalize the scattered amplitude from the graphene layer per 4H-SiC(0001) (1×1) unit cell.

$F_I(\ell)$ in Eq.(20) is the structure factor of the interface region between the bulk and the graphene film. Although we cannot obtain lateral information about the SiC(0001) $(6\sqrt{3}\times6\sqrt{3})$R30°or SiC $(000\bar{1})$ interface reconstruction structure from reflectivity data, the vertical shifts of atoms and layer density changes associated with them can be determined. To begin to understand this interface, we allow for a reconstruction by placing a SiC bilayer plus an interface containing up to three additional atomic layers between the bulk and the multi-layer graphene film [see Fig. 31]. We then write the interface structure factor as:

$$F_I(\ell) = \sum_{j=1}^{5} f_j(\ell)\rho_j e^{i2\pi\ell z_j/c_{\rm SiC}}, \tag{21}$$

where ρ_j is the relative atom density for the $j^{\rm th}$ interface layer ($\rho_j = 1$ for a bulk layer corresponding to 8.22×10^{-16}atoms cm^{-2}) at a vertical position z_j (the zero height is chosen as the last layer of atoms in the interface). $f_j(\ell)$ is the atomic form factor of C or Si. The fifth atom layer is added to explore the possibility of adatoms between the SiC and the graphene.

To be completely general the scattered amplitude from the graphene film takes into account the possibility of a lateral distribution of varying graphene layers. This is done by defining an occupancy parameter p_n as the fractional surface area covered by all graphene islands that are n graphene layers thick. p_n is subject to the constraint equation $\sum p_n = 1$, where p_0 is the fraction of area that has no graphene. The multilayer graphene structure factor can then be written in the general form:

$$F_G(\ell) = f_C(\ell) \sum_{n=1}^{N_{\max}} p_n \left\{ \sum_{m=1}^{n} F_m(\ell) e^{2\pi i l z_m / c_G} \right\}, \tag{22a}$$

$$z_m = \begin{cases} D_0 + (m-1)D_1 & m \leq 2 \\ D_0 + D_1 + (m-2)D_G & m > 2 \end{cases}. \tag{22b}$$

f_C is the atomic form factor for carbon and $N_{\max}$ is the number of layers in the thickest graphene film on the surface. D_0 is the spacing between the bottom layer of an island and the last atom layer in the interface. D_1 is the spacing between graphene layer-1 and layer-2, while D_G is the average layer spacing between graphene in subsequent layers [see Fig. 31].

Because STM studies of multi-layer graphene films grown on the Si-face indicate some buckling of the graphite layer,,[49,51,128] a small vertical height distribution in each graphene layer must be allowed. This gives rise to a structure factor, $F_m(\ell)$ in Eq.(22a), for each layer. A vertical modulation of the graphene layers can be modeled two ways. The simplest method is to assume an average, layer independent, random vertical disorder, σ_G, that will give rise to a Debye-Waller term for each layer, i.e. $F_m(\ell) = e^{-q_\perp^2 \sigma_G^2/2}$. Because the vertical modulation is known to decay quickly after the first graphene layer,[51] a more refined model uses the same average Debye-Waller term for the upper graphene layers but allows for a different distribution of carbon atoms in the first graphene layer such as those calculated in *ab intio* calculations.[129] In this case the the structure factor of the first layer, $F_1(\ell)$, needs to be known. Both models have been used for the Si-face fits and, as it turns out, give very similar results. This will be discussed further in the following section.

Si-face Reflectivity Results

Reflectivity data for a Si-face multi-layer graphene film is shown in Fig. 36. The main bulk 4H-SiC peaks occur at $\ell=4$ and $\ell=8$. The sharp peaks at $\ell=2$, 6 and 10

are the "quasi-forbidden" reflections of bulk SiC.[43] In SiC reciprocal lattice units, the graphite bulk reflections are nominally expected at $\ell \sim 3$, 6 and 9 (i.e., $\ell = \ell_G(c_{SiC}/c_G)$, where $\ell_G = 0$, 2, 4 etc.).

A number of structural models for the graphene/4H-SiC(0001) interface have been tested. While the majority of experimental studies point to a complicated interface structure, simple models consisting of a nearly bulk terminated substrate with the graphene on top are often proposed.[38] However, these type of models always give poor fits to the X-ray data. This is demonstrated in Fig. 36 where the best fit reflectivity is plotted for a bulk terminated surface where the $6\sqrt{3}$ interface layer is essentially a structural graphene layer. In this model, the interface layer-0 in Fig. 31 is replaced by a single carbon layer with a graphitic density. The last bulk bilayer density is kept constant at the bulk value while the bilayer spacings are allowed to relax (the relaxation from the bulk value are small; $\Delta_{2C} = -0.03$Å and $\Delta_{2Si} = 0.01$Å). The distance between the last SiC bilayer and the graphitic interface layer relaxes to a best fit value of 2.55Å and the distance between this layer and the next graphene layer is 3.62Å (i.e, much larger than the bulk graphite spacing of 3.354Å). All other parameters in Eqs. (21) and (22) are allowed to vary to achieve the best fit shown in Fig. 36. As can be seen, this model gives a very poor fit to the data at values of $\ell = 5$ and 9, the anti-Bragg points for SiC. This is typical of all bulk terminated models including those with a substantial modulation of the first graphene layer such as the calculated $(6\sqrt{3}\times 6\sqrt{3})$R30°surface of Varchon *et al.*[129] The calculated reflectivity from this theoretical interface, including a relaxed bulk surface and the structure factor $F_1(\ell)$ of the rippled first graphene layer, gives similarly poor fits to the reflectivity near the anti-Bragg positions.

Better fits can be obtained by an extended interface where an additional partial layer of adatoms is added to the simple relaxed bilayer model [see the schematic models in Fig. 36]. As demonstrated in Fig. 36, the additional density from the

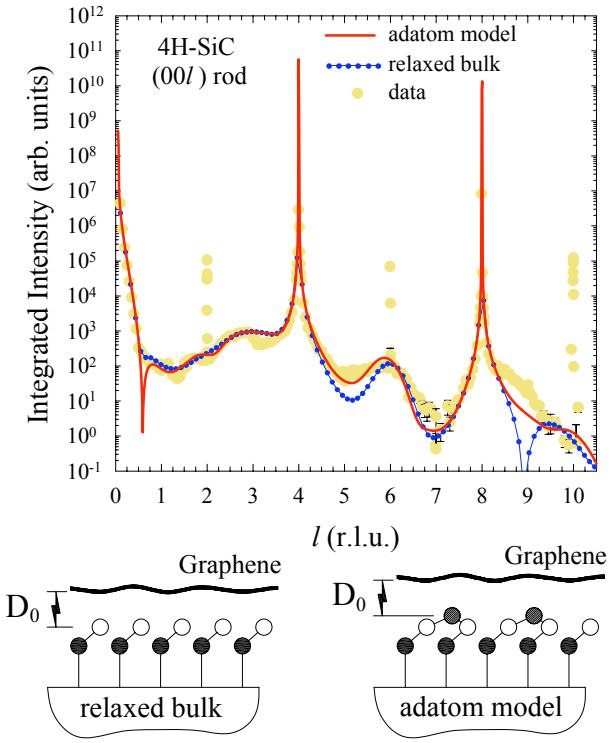

Figure 36: Specular reflectivity versus $q_\perp$ (in r.l.u.) for a graphitized 4H-SiC(0001) Si-face surface. Circles are the data. Fits to the two model structures in the figure are given. In the schematic models filled and open circles are C and Si atoms, respectively. Shaded circles are Si adatoms. Dotted blue line is a fit to a bulk terminated SiC(0001) surface with a single relaxed bilayer. Solid red line is a fit to a model similar to the relaxed bilayer but with the addition of a layer of Si-adatoms with $\rho_{\rm ad} = 0.21$.

adatoms begins to correct many of the deficiencies in the relaxed bulk model fit at the anti-Bragg points (especially near $\ell = 9$). Note that the adatom model used to fit the reflectivity is very similar to the model proposed by Rutter *et al.*,[128] including the Si adatom density which is $\rho_{\rm ad} = 0.21$ compared to 0.22 in their model.

The improvement in the calculated intensities by adding an adatom layer is due to the increased scattered intensity at the SiC anti-Bragg condition that is normally zero in a bulk terminated interface. Regardless, the simple adatom model cannot reproduce a number of features in the reflectivity data above $\ell > 4$. The inability of this model to fit the experimental data is a result of both an insufficient atomic density in the interface and the atomic gradient through the interface. Increasing the width of the interface adds an additional Fourier component in Eq.(21) that both

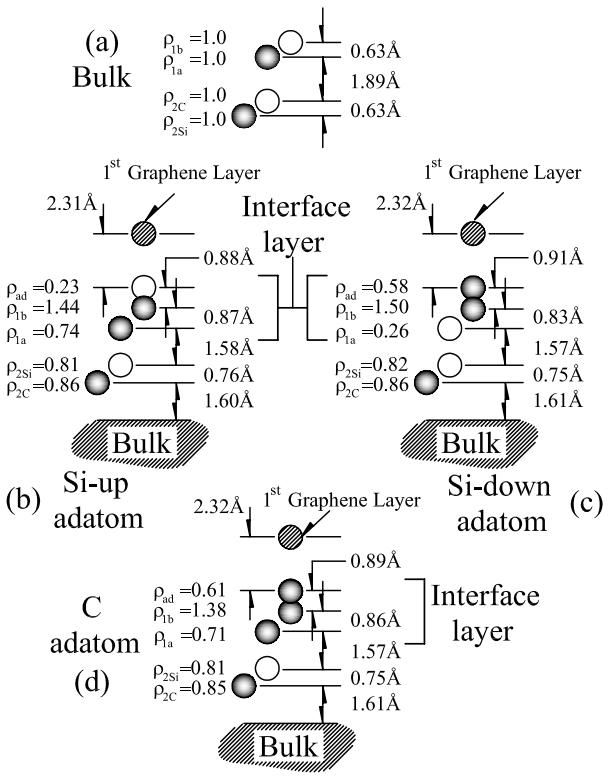

Figure 37: Three graphene/SiC interface ball models for graphene grown on the Si-face of SiC determined by surface X-ray reflectivity; (b) Si-up model, (c) Si-down model and (d) C-adatom model. Open circles are silicon atoms and shaded circles are carbon atoms. The densities ρ are relative to the densities of bulk SiC shown in (a).

broadens the fit near $\ell \sim 6$ and removes the interference minimum at $\ell \sim 9$. Therefore, to improve the fits, it is necessary to change both the atom distribution and the thickness of the interface layer. The need for an additional plane of atoms is also consistent with number of STM experiments of the SiC(0001) $(6\sqrt{3}\times 6\sqrt{3})$R30°interface. STM images of "trimer-like" structures suggest at least one additional partial layer of atoms.[49,51,111,128,130]

Adding a 5^{th} layer of atoms and changing the atom density in the interface layer-0 leads to a set of nearly identical structures that are shown in Fig. 37. These structures are distinguished by whether an atom plane in the interface is composed of carbon or silicon atoms. This is because in X-ray diffraction the ratio of atomic form factors of Si and C used in Eq.(21) is determined, to first order, by the ratio of their atomic

numbers 14/6 = 2.33. Therefore, the model calculation should give a similar fit if all silicon atoms are replaced by carbon atoms with 2.33 times the density (however, there is a substantial difference in the ℓ dependence of the Si and C atomic form factors that affects both the ρ's and z_j's in the final fits). While X-ray reflectivity data alone is unable to distinguish between different silicon and carbon compositions in the interface layer, spectroscopic data from a number of experimental groups place restrictions on the atomic makeup of layer-0 in Fig. 31.

Angle resolved photoemission spectroscopy (ARPES) studies by Seyller *et al.*[97] as well as X-ray photoemission spectroscopy (XPS) studies by Johansson *et al.*[93] conclude that the interface layer has a significant carbon concentration (at least 1.3 times more than the carbon in a bulk SiC bilayer) that rules out a purely silicon interface. In fact the X-ray diffraction also rules out a purely silicon interface because the density of silicon required to get reasonable fits to the reflectivity data is almost half the density required for an sp^3 silicon film, which is physically unreasonable. These spectroscopic constraints reduce the number of possible structures that are compatible with the reflectivity data to three: the "C-adatom", "Si-up", and "Si-down" models shown in Fig. 37.

The best reflectivity fit to the data is nearly identical for all three models and is shown in Fig. 38. Table 3 gives the fitting parameters for all models (uncertainty limits include variations from sample to sample). In the C-adatom model a carbon rich layer composed of three carbon layers is sandwiched between the graphene and a distorted SiC bilayer. The total density of these three interface layers is $\rho = 0.61 + 1.38 + 0.71 = 2.70 \pm 0.15$. This density is lower than the density of a graphene sheet ($\rho_G = 3.13$) but is 30% higher than a bulk SiC bilayer. The two Si models are similar to the C-adatom model in that they contain a carbon rich layer, although it is composed of two rather than three carbon layers sandwiched between the graphene. The total carbon density of the interface layers in the Si-up and Si-down models are $\rho = 1.44 + 0.74 = 2.18 \pm 0.15$,

Table 3: Best-fit interfacial structural parameters for graphene covered 4H-SiC(0001) Si-face. Data for the "Si-up", "Si-down" and "C-adatom" models give nearly identical fits. Parameters are defined in Figs. 31 and 37.

	d_{ad} (Å)	ρ_{ad} (Å)	Δ_{1b}(Å)	ρ_{1b} (Å)	Δ_{1a} (Å)	ρ_{1a}	Δ_{2C}(Å)	ρ_{2C}	Δ_{2Si}(Å)	ρ_{2Si}
Si-up	0.88	0.23	-0.23	1.44	-0.47	0.74	-0.29	0.86	-0.16	0.81
Atom Type		silicon		carbon		carbon				
Si-down	0.91	0.58	-0.28	1.50	-0.48	0.26	-0.28	0.86	-0.16	0.82
Atom Type		carbon		carbon		silicon				
C-adatom	0.89	0.61	-0.25	1.38	-0.48	0.71	-0.28	0.85	-0.15	0.81
Atom Type		carbon		carbon		carbon				
uncertainty	0.04	0.08	0.04	0.08	0.04	0.1	0.05	0.1	0.05	0.08

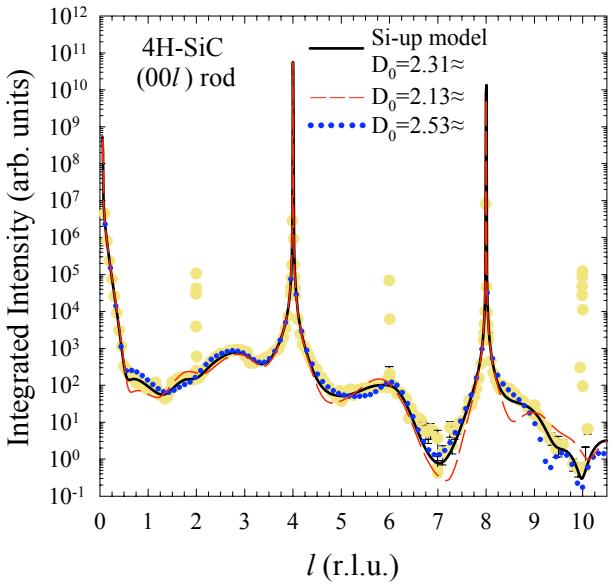

Figure 38: Specular reflectivity versus $q_\perp$ (in r.l.u.) for a graphitized 4H-SiC(0001) Si-face surface. Circles are the data. Solid black line is the best fit to the Si-up model in Fig. 37(b) with $D_0 = 2.31$Å(the C-adatom and Si-down model fits would be identical). Dashed red line is the same fit but with a smaller $D_0 = 2.13$Å. Dotted blue line is the same fit but with a larger $D_0 = 2.53$Å.

and $0.58 + 1.50 = 2.08 \pm 0.15$, respectively. These values are similar to the total bulk bilayer density ($\rho = 2.0$) needed to form a sp^3 bonded carbon layer. The two Si models are distinguished by a low density of Si atoms either atop or below the carbon rich interface layer.

There are two similarities between all three models. First, the carbon densities in all three models suggest a complicated carbon bonding geometry that is neither like bulk SiC or like graphene. This has also been noted by both Emtsev *et al.*[38] and Johansson *et al.*[93] who studied the $(6\sqrt{3}\times 6\sqrt{3})$R30° reconstruction that forms before graphitization and is known to persist after a true graphene layer has formed. The ARPES data of Emtsev *et al.* shows that the interface layer has σ bands (although shifted to higher energy) but no π bands. This suggests that the carbon concentration is high enough to at least locally support a sp^2 bonding geometry. In addition, the XPS studies of both Johansson *et al.*[93] and Emtsev *et al.*[38] find two surface related C

1s core level shifts. As a result both studies conclude that the $(6\sqrt{3}\times 6\sqrt{3})$R30° surface contains a large amount of non-graphitic carbon in inequivalent surface sites in spite of the σ bands.

The second similarity between these models is that, unlike the SiC$(000\bar{1})$ C-face (to be discussed in the following section,) the Si-face interface reconstruction extends deeper into the bulk. The bilayer between the interface layer and the bulk is substantially altered from a bulk bilayer in both density and bonding. This deep reconstruction on the (0001) surface is consistent with the prediction of Johansson *et al.* based on relative intensity ratios of surface to bulk XPS peaks. Regardless of the model, the bond lengths between this bilayer and both the bulk and the interface layer are contracted by $\sim$17% from the bulk Si–C bond length making them similar to the bonds in diamond (1.54Å).[131]

The main difference between the "C-adatom" and either the "Si-up" or "Si-down" models is the low density Si layer in the interface region. While X-ray data alone cannot discriminate between an all carbon interface and a carbon rich interface with silicon, spectroscopic measurements strongly favor the two models with silicon in the interface. XPS and photoemission spectroscopy (PES) experiments conclude that, after graphene has formed, a significant fraction of Si remains at the interface.[93,111,132] The complete XPS study by Johansson *et al.* finds that in addition to two surface related C 1s core level shifts, there are also two surface related Si 2p core level shifts. This is consistent with a Si adatom layer in the interface and a modified Si-C bond between the interface and the bulk-like bilayer below. Additionally, the bonding configuration of the Si-up model is very similar to a model proposed from STM images of the $(6\sqrt{3}\times 6\sqrt{3})$R30° interface structure below a layer of graphene.[128] The model of Rutter *et al.*[128] suggests an adatom density of $\rho_{\mathrm{ad}} = 0.22$; within error bars of the X-ray value in Table 3. At the moment, however, there is no experimental data that can exclude either of the two Si models.

The most important result of this data is that the interface layer for Si-face graphene is not a simple relaxed bulk termination of the SiC surface. This has a bearing on how to interpret electronic structure calculations of the graphene-SiC interface. To date, *ab initio* electronic structure calculations of the EG/SiC(0001) system have started from a flat graphene layer placed above an idealized bulk terminated SiC surface that is allowed to relax into a slightly distorted bilayer.[128,133,134] These calculations use an artificially contracted graphene sheet that is commensurate with a small SiC cell to allow for reasonably fast calculation times. Rutter *et al.*[128] looked at a Si adatom model but, as with other calculations, used a simple relaxed bulk SiC bilayer below the adatoms. The result of all these calculations is that the first graphene layer above the relaxed bulk SiC bilayer acts as buffer that partially isolates the electronic properties of the next graphene layer from the substrate.[133,134] While these calculations are an important first step in predicting the existence of a buffer layer, their ability to predict the structure of the interface and thus its electronic properties is a concern given that the X-ray results show a much more substantial reconstruction that has few characteristics of a bulk SiC bilayer. Further experimental evidence for a buffer layer comes from ARPES, where a carbon-rich layer with substantial sp^2-bonding is found without any indication of π bands characteristic of graphene.[38,93] ARPES measurements also clearly show π-bonded graphene layers above this carbon-rich layer, although there are different interpretations of spectral structure very close to the K-point of the graphene Brillouin zone for the first of these structural graphene layers.[135,136] It is possible that the first graphene layer in the *ab initio* results mimics, to some extent, the properties of the interface layer-0. In fact, recent *ab initio* calculations by Varchon *et al.*,[129] using a full $(6\sqrt{3}\times 6\sqrt{3})$R30° cell, find that the first graphene layer is significantly distorted from a flat graphene sheet and does not show the dispersion characteristic of an isolated graphene sheet. The calculated modulation amplitude is 1.23Å, a value not far from the $\sim$1.8Å interface

layer width measured for all the structural models in Fig. 37. These results suggest that the assumption of a distorted thick carbon-rich layer acting like a buffer layer may be correct. A more realistic interface calculation will be necessary to test this assertion.

In addition to the interface structure, the reflectivity data provides additional evidence supporting conclusions based on STM and LEED that the $(6\sqrt{3}\times 6\sqrt{3})$R30° reconstruction observed after graphitization is a true reconstruction of the graphene film. Since the discovery of the $(6\sqrt{3}\times 6\sqrt{3})$R30° LEED pattern, it has been suggested that it is a moiré pattern due to the near commensuration of graphene with SiC.[45,50] However, recent STM experiments directly imaged the $(6\sqrt{3}\times 6\sqrt{3})$R30° structure and shown that the graphene has a vertical modulation with this lateral periodicity.[51,128] As mentioned above, recent *ab initio* calculations, using a full $(6\sqrt{3}\times 6\sqrt{3})$ R30° cell, find that at least the first graphene layer above the SiC has a substantial modulation amplitude.[129] The X-ray reflectivity data supports these recent experiments and confirms that there is a vertical modulation of graphene grown on the Si-face. This can be seen by comparing the C-face and Si-face graphene layer roughness or corrugation, σ_G, from Eq.(22a) [see Table 6, at the end of the reflectivity discussion]. σ_G is much larger on Si-face grown graphene than on C-face furnace grown graphene. σ_G is determined almost solely by the intensity decay of the graphite Bragg points as a function of ℓ. Because of the exponential form in Eq.(22a), a finite σ_G manifests itself as a decay in the graphite Bragg peak intensities at ℓ=6 and 9. This is demonstrated in Fig. 39 where a comparison is made between a graphene film with $\sigma_G = 0$Å and a film with $\sigma_G = 0.3$Å. From the current experiments $\sigma_G = 0.16$Å for Si-face graphene. We can interpret σ_G as originating from an actual modulation of the graphene film, but the value of 0.16Å is considerably smaller than the value of 0.6Å measured by STM for the first graphene sheet above the interface layer.[128] This difference arises because STM is measuring a modulation in the electron density of

states instead of an actual structural modulation but more importantly, because the X-ray value is an average over all the graphene layers in the film. Riedl *et al.*[51] have shown that the vertical modulation amplitude decays by approximately a factor of two from the first to the second graphene layer. Therefore, thicker graphene films weight the average σ_G to lower values.

The first graphene layer modulation, $\sigma_G^{(0)}$, can be estimated from the measured mean modulation σ_G if we assume that the modulation decays in subsequent layers as $\sigma_G^{(n)} = \sigma_G^{(0)} \exp[-\lambda D n]$ where $\lambda D = 1/\ln(2)$ (the factor of $\ln(2)$ assumes the amplitude decay measured by Riedl *et al.*[51] is correct). To calculate $\sigma_G^{(0)}$ we only need to know the relative amount of graphene that is thicker than N layers, P_N. P_N is calculated from the areal coverage, p_n's in Eq.(22a); $P_N = C \sum_{n=N}^{N_{max}} p_n$ (C is a normalization constant). Then $\sigma_G^{(0)}$ is given by;

$$\sigma_G^{(0)} = \sigma_G \sum_n P_n / \sum_n P_n \exp\left[-\lambda D n\right]. \tag{23}$$

The measured distribution of graphene layer thickness, p_n, for a nominally 2-layer graphene film is shown in the layer height histogram in Fig. 40. The average number of graphene layers is 1.9 ± 1.5. The distribution is very wide, in part reflecting the spatial average over the large X-ray beam footprint (the footprint is bigger than the sample width of 3mm when $\ell < 1.8$). In particular the high areal fraction not covered by graphene (18%) can be associated with slow growth kinetics at cooler substrate regions near the edge of the sample caused by non-uniformity in the e-beam heater. These wide distributions are also seen in low energy electron microscope (LEEM) images.[100] Using this measured distribution, $\sigma_G^{(0)}$ estimates range between 0.5-0.8Å reflecting the uncertainty in the measured value of σ_G. This result is in very good agreement with the STM value of 0.6Å.[128]

The thickness of the first layer has also been estimated using a model of a modulated first graphene layer on-top of the Si-up adatom model. $F_1(\ell)$ in Eq.(22a) is

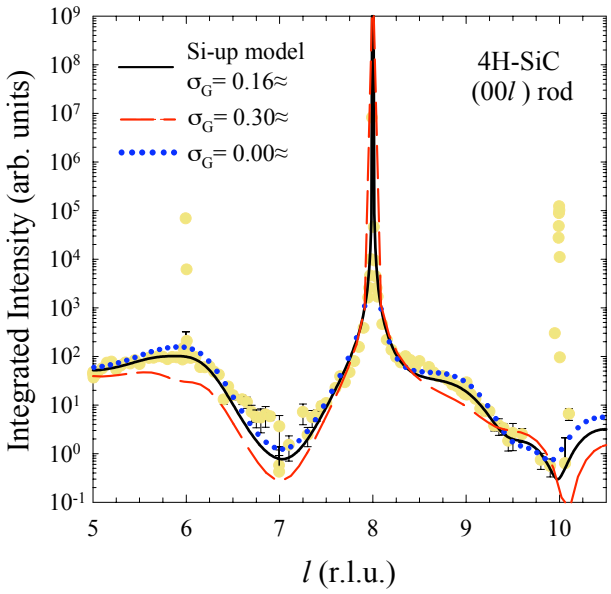

Figure 39: Specular reflectivity versus $q_\perp$ (in r.l.u.) for a graphitized 4H-SiC(0001) Si-face surface. Circles are the data. Solid black line is the best fit to the Si-up model with $\sigma_G = 0.16$Å. Dashed red line is the same fit but with $\sigma_G = 0.0$Å. Dotted blue line is the same fit but with a larger $\sigma_G = 0.30$Å.

calculated using the graphene structural coordinates of Varchon *et al.*[129] The modulation of higher graphene layers is included using the rms roughness in the standard model. While the relative vertical carbon positions are maintained in the first graphene layer, the absolute positions are scaled by a multiplicative constant so that the peak-to-peak amplitude can be varied. The best fit structure to the reflectivity data gives the first graphene layer amplitude to be 0.82Å, which is slightly larger than than the range of $\sigma_G^{(0)}$ estimated above.

It is worth comparing the graphene thickness measured by SXRD and an estimate from the simpler AES method discussed in Sec. 4.4[53,54,80] in which the ratio of the Si(LVV)/C(KLL) peak area was used, along with proper electron mean free paths and excitation cross sections, to estimate of the number of graphene layers. This is a model dependent calculation, so the use of a suitable interface model is crucial. This was explained in Sec. 4.4. Most groups use an interface model consisting of a bulk terminated substrate with graphene above. While this is clearly inconsistent

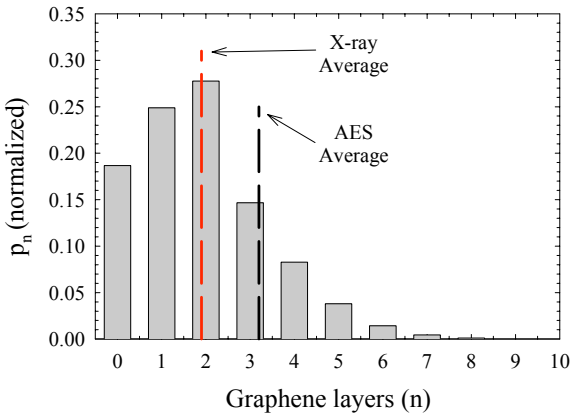

Figure 40: The normalized probability, p_n, of a n-graphene layer stack from a UHV grown Si-face film as determined by X-ray reflectivity. The X-ray average is 1.9 ± 1.5 graphene layers while the AES estimate of the average is approximately one layer thicker (3.2 layers).

with the both models in Fig. 37, it can still be used with the proviso that it will overestimate the film thickness by $\sim$1 layer because the measured C(KLL) intensity includes a contribution from the dense non-graphitic interface carbon layer in Fig. 37. AES measurements on the same sample as the data for Fig. 40 estimate the average graphene coverage to be 3.2 layers compared to 1.9 by X-rays, consistent with the lack of a realistic interface layer in the AES calculation.

C-face Reflectivity Results

Reflectivity data for a C-face multi-layer graphene film are shown in Fig. 41. As on the Si-face, the main bulk 4H-SiC peaks occur at $\ell = 4$ and $\ell = 8$ and the sharp peaks at $\ell = 2$, 6 and 10 are the "quasi-forbidden" reflections of bulk SiC.[43] The graphene bulk reflections are again expected at $\ell \sim 3$, 6 and 9. While there are many variables in Eqs. (20)-(22) that eventually must be fit, a number of the parameters are quite unique and insensitive to the exact structural model used for the EG/SiC $(000\bar{1})$ interface. For instance, because the graphene Bragg points are intense and narrow in ℓ on this face, the mean spacing between graphene layers, D_G, is determined with high accuracy relative to the known SiC lattice constant. Similarly, the graphene layer roughness or corrugation, σ_G, is determined almost solely by the intensity decay of the

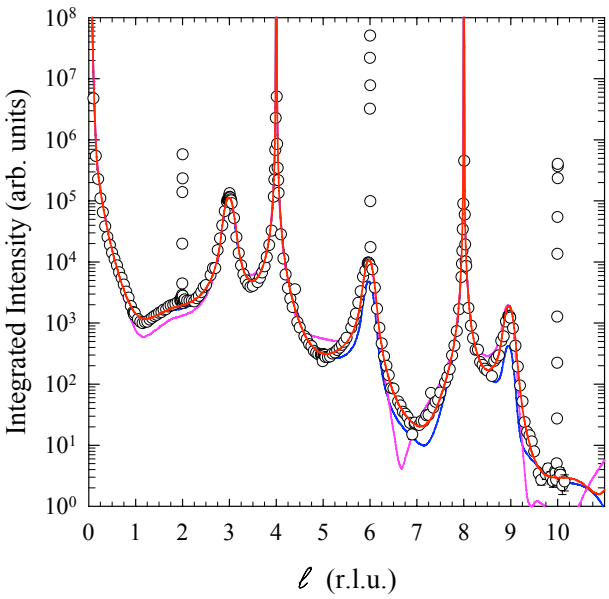

Figure 41: Specular reflectivity vs. $q_\perp$ (in r.l.u.) for a graphitized 4H-SiC(000$\bar{1}$) C-face surface with 9 graphene layers. Solid lines are best fits to the structural models described in the text. Red solid line is the best fit to the structural model with a smooth graphene layer ($\sigma_G = 0.0$Å). Blue solid line is the best fits with a corrugated graphite layer ($\sigma_G = 0.25$Å). Magenta line is the best fit if the graphene substrate distance D_0 is reduced 10%.

graphite Bragg points as a function of ℓ. As will be seen, the roughness on the C-face is far less than the comparable quantity on the Si-face, so only the simpler fit of σ_G was used in this analysis. (This uses an average, layer independent vertical disorder for σ_G that was described in the above introduction of the reflectivity discussion.) Once these two nearly model-independent parameters are determined, they are fixed so that different structural models of the interface can be compared without relying on adjusting larger numbers of parameters.

A number of structural models for the EG/4H-SiC(000$\bar{1}$) interface have been tested. As on the Si-face, simple relaxations of the top SiC bi-layers always give poor fits to the data. Attempts to make a carbon rich phase that extends many layers into the bulk, a model that has been proposed in the literature,[45,47,137] was not compatible with the data. An important note, however is that all of these cited studies are on UHV grown C-face films, which could potentially have a different interface structure because they grow at much lower temperatures (1250°C vs. 1420°C.)

Table 4: Structural parameters for graphene grown on 4H-SiC(000$\bar{1}$) C-Face. Parameters are defined in Fig. 31

	D_0 (Å)	D_1 (Å)	D_G(Å)	σ_G (Å)
fit value	1.62	3.41	3.368	0.00
uncertainty	0.08	0.04	0.005	0.05

The best fit model is a distorted bilayer between the graphene and bulk SiC. A schematic of the model was shown in Fig. 31. For the C-face system, the first bilayer above the bulk is slightly relaxed. However, the next bilayer (immediately below the graphene) has a significant relaxation. As shown below, two similar versions of this model structure give nearly identical fits to the data.

Before looking at the details of these models, we point out a few important model-independent parameters for the graphite film. First, the average graphene inter-layer spacing is found to be $D_G = 3.368 \pm .005$Å. This and other graphene film parameters are given in Table 4. The value was determined from samples with films ranging from 9-13 graphene layers (averaged over the beam footprint). As mentioned above the inter-layer spacing is nearly independent of all other fit parameters and can be determined with high accuracy because it is fixed by the ℓ position of the three strong graphite Bragg peaks in Fig. 36. The inter-layer spacing is larger than bulk crystalline graphite (3.354Å)[14] but smaller than the lattice spacing of turbostratic graphite ($D_{TG} = 3.440$Å).[138,139] The larger spacing is due to stacking faults between adjacent layers caused by interference between π^* states that give rise to a larger repulsive interaction between adjacent graphene sheets.[138] This phenomenon will be fully explored in the following sections.

Another parameter that is insensitive to the details of the interface model is, σ_G, in Eq.(22a). This parameter can be interpreted two ways: either as a finite width of a graphene layer due to buckling of carbon atoms in the layer, or as an RMS roughness of a graphene layer due to vertical disorder over the coherence length of the X-ray beam ($\sim 2\mu$m). It was found that $\sigma_G = 0.0 \pm 0.05$Å (see Table 4). Because of the

exponential form in Eq.(22a), a finite layer width manifests itself as a rapid decay in the graphene Bragg peak intensity at high ℓ. This is demonstrated in Fig. 36 where a comparison is made between a flat graphite film and a film with an RMS thickness of $\sigma_G = 0.25$Å. The finite layer width severely reduces the graphite peak intensities at ℓ =6 and 9.

Fits to the reflectivity show that two similar model structures for the interface region between the bulk and the graphene represent the experimental data equally well. These models have been labeled as the"Carbon-corrugated" and "Carbon-rich" models. In both cases the SiC bilayer immediately above the bulk in Fig. 31 remains "bulk-like" in terms of both density and inter-layer spacing. The two models are distinguished by the structure of the next three layers just below the graphene film. Ball models of the two structures are shown in Fig. 42 and the detailed fitting parameters are given in Table 5. Structural values were determined for three different samples. The fitting parameter variations from sample to sample are included in the uncertainty limits of Table 5.

In the C-Corrugated model the last SiC bilayer is contracted inwards towards the bulk by 0.11Å to give a slightly smaller Si–C bond length. In the uppermost bilayer the carbon is buckled into two equal density layers. The density of both the Si layer (ρ_{1a}) and the sum of the buckled carbon layers ($\rho_{ad} + \rho_{1b}$) in this bilayer are each $\sim 2/3$ of the bulk value. It is unlikely that the last layer is a carbon adatom. If it were, the density required to saturate the dangling bonds in the carbon layer below would be $\rho_{ad} = \rho_{1b}/3$ instead of being equal. For this reason this model is refered to as a corrugated surface. We note that the fits are very sensitive to the Si density, ρ_{1a}, in the last bilayer. If the last bilayer is forced to have the same Si atom density as in the bulk, the best fit model cannot reproduce the data. This is demonstrated in Fig. 43 where a best fit to the "C-Corrugated" model is shown where ρ_{1a} was forced to be the bulk denisity. Similarly, removing the buckling in the carbon layer

Table 5: Best-fit interfacial structural parameters for graphene covered 4H-SiC(000$\bar{1}$) (C-Face). Data for both the "C-Corrugated" and "C-Rich" models give nearly identical fits. Parameters are defined in Figs. 31 and 42.

	δ_{ad} (Å)	ρ_{ad} (Å)	Δ_{1b}(Å)	ρ_{1b} (Å)	Δ_{1a} (Å)	ρ_{1a}	$\Delta_{2C} = \Delta_{2Si}$(Å)	$\rho_{2Si} = \rho_{2C}$
C-corrugation	0.66	0.36	0.18	0.38	-0.14	0.64	-0.03	0.94
Atom Type		carbon		carbon		silicon		
C-rich	0.63	0.77	0.11	1.29	-0.33	1.47	-0.04	0.94
Atom Type		carbon		carbon		carbon		
uncertainty	0.04	0.08	0.04	0.08	0.04	0.10	.04	.05

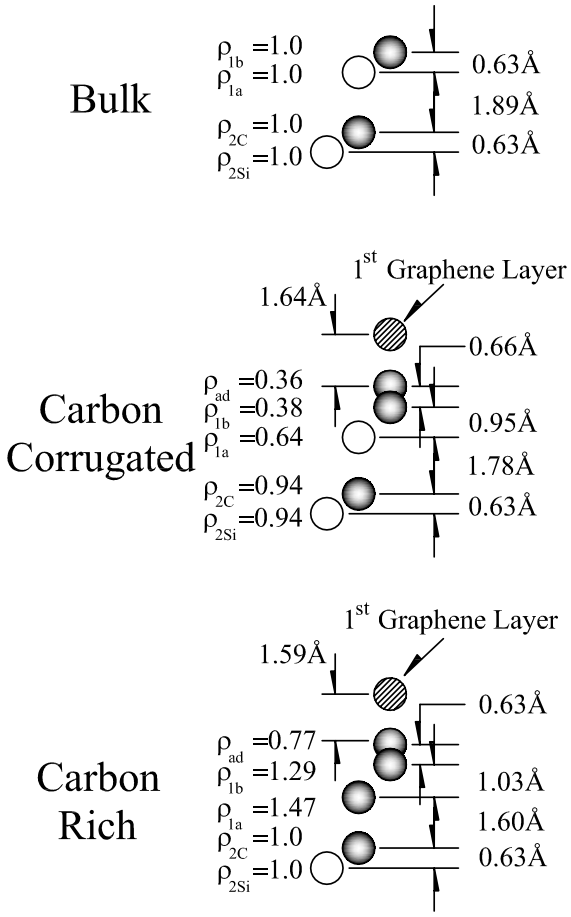

Figure 42: Schematic ball models of bulk, C-Corrugated and C-Rich interface layers between the substrate and the graphene film. (•) are carbon atoms and (∘) are silicon atoms. Hatched atoms are carbon atoms in the first graphene layer. Interlayer spacings and densities (relative to bulk SiC) are shown.

("Smooth C-layer" model) while keeping the total density the same cannot reproduce the reflectivity modulation between $0.5 < \ell < 2.5$ (see Fig. 43).

As mentioned in the previous section, to first order the ratio of the atomic form factors for Si and C, f_{Si}/f_C in Eq.(21), is determined simply by the ratio of their atomic numbers $14/6 = 2.33$. Thus, the model calculation gives a similar fit if the Si atoms in the top SiC bilayer are replaced by carbon atoms with 2.33 times the density ($\sim 2.33 \times 0.64 = 1.49$). This replacement gives the "C-rich" model shown in Fig. 42 with densities and layer spacings adjusted to give the best fit to the data. In Fig. 42 the best fit parameters show that there are two main differences

between the C-Corrugated and C-Rich models. First, the layer spacings between bilayers is considerably shorter (1.60Å) and second, the densities in the last layers are higher. The bilayer spacing measured in the C-rich model is slightly larger than the bond length of diamond (1.54Å).[131] The higher carbon layer densities have a similar significance in that they lie half way between the SiC density ($\rho = 1.0$) and that of graphene ($\rho = 3.13$). In fact, the first C-layer in the bilayer has a density close to the atom density of a (111) diamond plane, 1.51.

While it may seem reasonable to expect that as Si sublimates from the surface a carbon rich interface forms with some diamond-like character, we should caution that there are other ways to interpret these results. First of all, the spacing between planes in the bilayer is much larger, 0.63-1.03Å, while in diamond they should be much lower, 0.51Å. The C-Rich phase is also considerably different from the "extended diamond phase" proposed in the literature because it does not extend beyond the first bilayer.[45,47,137] In both models the relaxation of the bilayer above the bulk is small, contrary to what might be expected if there were significant density changes in that layer. These small changes from the model are not due to an insensitivity to either the layer spacings or the layer density. This is shown in Fig. 44 where calculated best-fit reflectivities are compared when either the Si density ρ_{2Si} is reduced or the Si–C spacing Δ_{2Si} is changed from the ideal value. As can be seen, inter-planar spacing changes of less than 5% (< 0.1Å) lead to obviously poor fits. Similarly, reducing the Si atom density in this layer by more than 25% makes the fit much worse. Therefore, the interfacial layer does not extend much beyond the top-most SiC bilayer. Note also that the total layer density of the last three interface layers is $\rho = 1.47 + 1.29 + 0.77 = 3.53$. This density is slightly larger than the density of a graphene sheet ($\rho = 3.13$). Rather than thinking of this layer as an ideal diamond like layer, it may be more appropriate to view it as a buckled graphene sheet with a mixture of sp^2 and sp^3 bonded carbon.

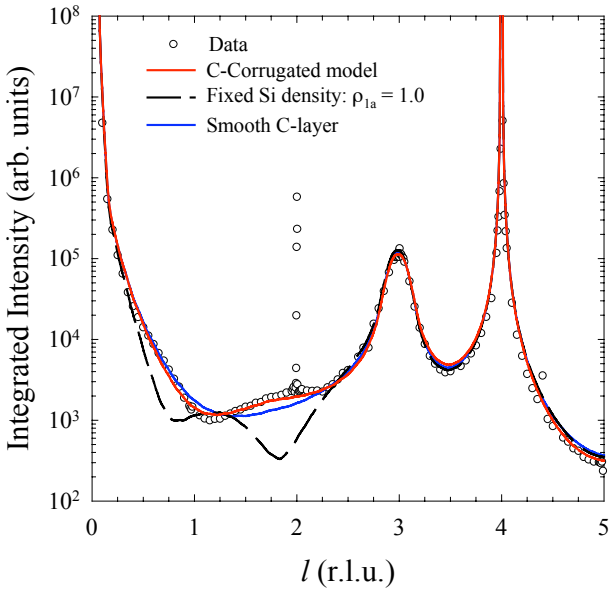

Figure 43: Specular reflectivity for a graphitized 4H-SiC(000$\bar{1}$) C-face surface. (○) are the data. Red line is the best fit to the Carbon-corrugated top layer. The black dashed line shows the fit for the same model if the Si layer density is fixed at the bulk value ($\rho_{1a} = 1$). The blue line is a fit when the carbon corrugation in the top layer is removed but the total density remains the same ("Smooth C-layer").

Arguably the most important finding from this reflectivity work is that the first graphene layer sits above the last bulk carbon layer at a distance of $D_0 = 1.62 \pm 0.08$Å. This value is, within error bars, insensitive to which structural model is used and can be determined with reasonable sensitivity as demonstrated in Fig. 36. The figure shows that 10% variations in D_0 from its optimal value lead to very poor fits to the data. The very short bond distance measured suggests that the first graphene layer is not simply bonded to the substrate with Van der Waal's bonds but instead has a much stronger interaction with the substrate.

As shown above, the X-ray reflectivity data shows that the interface between epitaxial graphene and the 4H-SiC(000$\bar{1}$) substrate is sharp. The interface is comprised of no more than 1–2 SiC bi-layers. The graphene that grows is flat (i.e. $\sigma_G = 0$Å) except for a small potential buckling of the first layer. There are two key structural parameters that deserve special attention. The first is the inter-layer spacing between graphene sheets that is much larger than expected for *AB...* stacked graphene layers

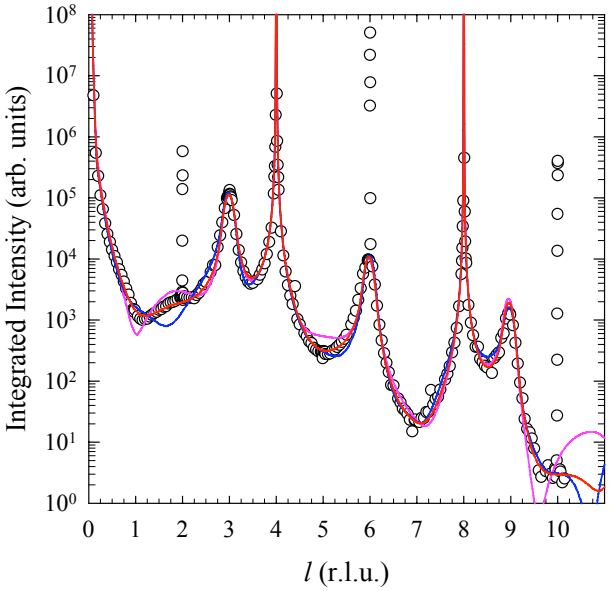

Figure 44: A comparison of the calculated reflectivity vs. $q_\perp$ (in r.l.u.) for different first SiC bilayer models. (Here the "first" bilayer is defined as the first one depicted in Fig.42 above the SiC bulk.) Red line is the best fit structure with bulk bilayer parameters. Blue line is a fit with ρ_{2Si} fixed at a value 25% less than the bulk. Magenta line is a best fit with the both Δ_{2Si} andΔ_{2C} relaxed towards the bulk by 5%.

and points to a significant stacking fault density in the film. As mentioned above, because stacking faults cause interference between π^* states in adjacent layers, these layers have a larger spacing. The mean layer spacing can, therefore, be used to estimate the stacking fault density.[138] If we define the probability, γ, that any two adjacent sheets are faulted, then the inter-layer spacing will range from that of $AB...$ stacked graphite (3.354Å) when $\gamma = 0$ to that of turbostratic graphite (3.44Å) when $\gamma = 1$. In that case the average inter-layer spacing for some finite number of stacking faults is approximately;[138]

$$D_G = 3.44 - 0.086(1 - \gamma^2). \tag{24}$$

Using the measured $D_G = 3.368$Å, gives $\gamma = 0.4$ for these C-face films. In other words, after every $1/(1 - \gamma) = 1.6$ graphene sheets, a stacking fault occurs in the film. The fact that there are frequent stacking faults is not surprising since

there is significant rotational disorder of graphene layers grown on this surface,[55] as thoroughly discussed in the following section. A pair of graphene sheets that are rotated with respect to each other would lead to regions of local *AB...* stacking separated by regions with other stacking arrangements. The mean graphene interlayer spacing would then be determined by the degree of rotational disorder. The existence of a large stacking fault density has an important bearing on the results of conductivity experiments on C-face grown multi-layer graphene films. This will be addressed in the following sections.

It is significant that the RMS layer width of the graphene is essentially zero, σ_G in Eq.(22a). On the Si-face, we saw that σ_G can represent either a random film roughness or a RMS corrugation of the graphene that is commensurate with the substrate. Because it is zero on the C-face, it can be concluded that beyond the buffer carbon layer the graphene layers are flat and must be very weakly interacting with any substrate potential. This explains why C-face graphene films can be rotationally disordered but have large domain sizes. The energy cost per atom to rotate a graphene sheet on a flat graphene substrate is very low (< 50meV/atom).[140,141] At the growth temperatures of 1400°C, and given the low registry forces implied from these experiments, growing graphene sheets can rotate freely, rather than becoming polycrystalline as suggested by Forbeaux *et al.*[55] On Si-face multi-layer graphene films the situation is different. As discussed above, there is a $(6\sqrt{3} \times 6\sqrt{3})\mathrm{R}30^0$ reconstruction in the first 2-3 graphene layers on this surface.[45,54] The graphene has a nonzero corrugation of about 0.16Å that could be enough to lock the growing film into registry. Step boundaries or other defects in the substrate can put domain boundaries in the graphene that are not easily removed by rotating large areas of the film. As will be seen below, this freedom for films to rotate results in truly unique properties for these C-face films.

Table 6: Structural parameters for graphene grown in UHV on 4H-SiC(0001) Si-face and those from furnace-grown 4H-SiC(000$\bar{1}$) C-face graphene. Parameters are defined in Fig. 31

	D_0 (Å)	D_1 (Å)	D_G(Å)	σ_G (Å)	γ_{SiC}
Si-Face	2.32 ± 0.08	3.50 ± 0.05	3.35 ± 0.01	$0.16(-.05/+.02)$	0.7 ± 0.1
C-face	1.62 ± 0.08	3.41 ± 0.04	3.368 ± 0.005	< 0.05	0.03 ± 0.01

Si-face & C-face Reflectivity Results: A Comparison

After looking at the data on each of the polar faces separately, it is worth pointing out a number of important structural differences between Si-face grown graphene and C-face grown graphene. Table 6 shows a comparison of structural parameters determined from X-ray reflectivity data for graphene grown on the SiC(0001) and (000$\bar{1}$) surfaces. The first major difference is seen in the parameter D_0. The distance between the first graphene layer and the interface for a UHV grown Si-face graphene film is $D_0 = 2.3 \pm 0.08$Å. Figure 38 shows the sensitivity of the Si-face fit to either increasing or decreasing the value of D_0 by 9%. For the furnace grown C-face films, D_0 is even smaller, 1.62 ± 0.08Å. Similarly, the magenta line in figure 41 shows a significant deviation from the data when the value of D_0 is varied by 10%. On both faces the measured value of D_0 is large compared to the bilayer distance in bulk SiC (1.89Å) and at the same time less than the graphite interplanar spacing of 3.354Å.[14] Note that the best fit value of D_0 on the Si-face is similar to the value of 2.5Å measured by STM.[128] The difference in D_0 measured for these polar faces implies that the graphene is more strongly bound to the C-face interface. This is also consistent with *ab initio* electronic calculations.[133,134] It should be noted that a publication based on recent ARPES experiments suggested that the C-face graphene grown in UHV is in fact less tightly bound to the interface compared to the Si-face,[38] contradicting the conclusion of previous inverse photoemission, PES and XPS experiments.[55,104,107] Yet, one should be careful when comparing the above X-ray data with other studies, as it is quite possible that UHV and RF furnace grown C-face films have different interface structures. UHV C-face graphene used in previous

studies[38,55,104,107] grows nearly 200°C lower in UHV compared to graphene grown in the RF furnace. This temperature difference, as well as what is present in the ambient atmosphere, may influence the interface structure or order.

D_1, the spacing between graphene layer-1 and layer-2, is another interesting parameter that exhibits a difference on the two polar faces. It is shown in Table 6 to be larger than the spacing between all other graphene layers (for both Si-face and C-face graphene). As D_0, this value is slightly larger for the Si-face films.

D_G is yet another inter-layer spacing parameter that is dependent on which polar face is being studied. In fact, although the variance seems small, ($D_G = 3.35 \pm 0.01$Å and 3.368 ± 0.005Å on the Si- and C-faces, respectively) it results in vast differences between the electronic structure of films grown on each of the polar faces. This is because the Si-face graphene is Bernal stacked and the C-face graphene has a high density of stacking faults. This particular aspect of the C-face films is the topic of the next section. Note that the error bar on D_G is significantly larger on the Si-face than C-face graphene films. This is because furnace grown C-face graphene films are much thicker than UHV grown Si-face films. Thinner films broaden the graphene Bragg peaks at $\ell = 3$, 6, and 9, making the peak position and thus the layer spacing more difficult to measure.

Table 6 also shows that the roughness of the SiC surface is more than an order of magnitude larger for Si-face graphene than for C-face graphene (the surface roughness is proportional to γ_{SiC}). This is consistent with the Si-face substrate roughness observed in many STM and AFM images.[42,51,97,98] This may also affect the difference in graphene layer corrugation (σ_G) seen, again to be an order of magnitude greater on the Si-face. Variance in σ_G is also likely due to the roughness (and periodicity) of the Si-face interface structure and may in turn impact the freedom for rotational disorder in the C-face graphene.

Finally, the fits to the interface region on each polar face can be compared. Immediately apparent from LEED data is the absence of an ordered interface reconstruction on the C-face, compared to a periodic reconstruction in the Si-face. This indicates that although it may be quite complex, there must be some type of regular structure underneath the Si-face graphene that is energetically favorable over the entire surface of the material. The C-face, on the other hand, does not exhibit a periodic bonding structure (or it is very poorly ordered.) A surface reconstruction has been observed prior to graphene formation,[104,107] but the atoms lose their ordered periodic arrangement as the graphene overlayers form. Both faces have multiple interface models which fit the X-ray reflectivity data equally well. On each face one of the possibilities is an interface made up of only carbon atoms, while the other options involve a carbon rich layer with silicon adatoms either above or below. In all cases, the interlayer spacings within the interface region relax to look like a single corrugated layer or one layer with an adatom structure.

The models compatible with the Si-face data all have comparable total atomic densities, being slightly lower when silicon atoms are present than when the interface is all carbon. It is interesting that the C-face fits change so much in overall atomic density when silicon atoms are used (compared to an all carbon interface.) When Si is present, the density of atoms in the interface is considerably less than that of a SiC bilayer and less than half of a graphene sheet. Yet, when the interface is entirely carbon, the atomic density is more than twice as great, in fact more than that of a single graphene layer. Further work needs to be done to investigate the possible bonding mechanisms which could lead to such atomic densities, as it is possible that *ab initio* calculations could rule out one configuration or another. Particular attention should be also be given to the tight bonding on both faces with the first structural graphene layer and the effects such bonding could have on the stacking of the subsequent graphene planes.

One last major difference in all of the the fits to the Si- and C-face interface regions is the extent to which it extends into the bulk SiC. Note that the final SiC bilayer in both of the C-face fits is quite bulk-like, with near bulk densities and inter-layer spacings. On the Si-face this is not the case. The densities are substantially less than in the bulk and the spacing within the bilayer is expanded. This demonstrates that the Si-face graphene growth affects structure farther into the bulk, a phenomenon that is likely linked to the increased surface roughening on the Si-face.

5.4.3 Crystal Truncation Rod Analysis

Probably the most significant difference between C-face graphene and Si-face graphene is its epitaxial order with respect to the SiC substrate. Evidence for this difference has been seen in LEED data and in the reflectivity data described above. In this section yet another kind of data will be explained which addresses this difference more directly.

It was originally thought that the azimuthal streaking in LEED images similar to that seen in Fig. 23 was due to HOPG type graphite consisting of azimuthally disordered *AB..* stacked domains. The evidence presented below indicates that this is not the case and that the LEED patterns are instead the result an unusual stacking order that is forced by the graphene/substrate interaction.

Although it may not be clear from the LEED images, a detailed look at the diffraction shows that the source of these streaks is not random rotational disorder. This is demonstrated in Fig. 45, where a SXRD azimuthal scan (ϕ scan) around $\phi = 0°$ is taken at the radial position of a graphene rod. This particular data was taken on the same sample from which the LEED pattern in Fig. 23(a) was taken. The scan shows intensity peaked at $\phi = \pm 2.2°$ with widths of $\sim 2.7°$. The significance of the $\pm 2.2°$ preferred rotation is two-fold. As seen in Sec. 2.3.1, graphene is commensurate with the SiC substrate when a 13×13 graphene unit cell is rotated 30° from SiC.

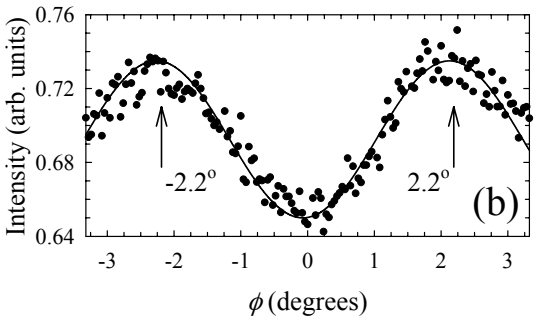

Figure 45: X-ray azimuthal scan of the diffuse graphite arc around $\phi = 0$ as defined in Fig.23. The scan was taken on the same sample for which LEED data is shown in Fig.23(a).

The 13×13 cell is $\sim 0.14\%$ smaller than a SiC $6\sqrt{3} \times 6\sqrt{3}$ $R30°$ cell. But, remember that there are two other ways to orient a 13×13 graphene sheet that have the same commensurabilty with the SiC $6\sqrt{3}\times6\sqrt{3}$ $R30°$ structure. These occur when graphene is rotated $\pm2.204°$ relative to SiC. As the LEED image in Fig. 23(a) clearly shows, all three rotated phases can appear in C-face grown multilayer graphene. The two spots near $\phi = 0$ are indexed as the $(8/13, 7/13, \ell)$ and $(7/13, 8/13, \ell)$ graphene rods. For simplicity they will be referred to as the $R2^{\pm}$ rods.

The significance of these three phases is even greater if it is recognized that two stacked graphene sheets can be rotated relative to each other in a number of ways that make the two sheets commensurate.[141] The lowest energy commensurate rotation angles are precisely $\phi = \cos^{-1}(11/13)$ or $\cos^{-1}(23/26)$ i.e, $30 \pm 2.204°$. This bi-layer structure corresponds to a graphene $\sqrt{13}\times\sqrt{13}$ $(R \pm 46.1°)$ cell. A schematic of such a fault pair is shown in Fig. 46.

While the observation of three rotational phases is interesting, it will be seen that it is their stacking order that bears directly on the film's electronic properties. The purpose of this section is to demonstrate via SXRD that $R30$ and $R2^{\pm}$ graphene sheets are interleaved to produce a high density of $R30/R2^{\pm}$ fault pairs instead of occurring as AB stacked $R30$ or $R2^{\pm}$ isolated domains. The existence of these particular kind of stacking faults is responsible for decoupling individual graphene sheets and is thus crucial for identification of these films as *multi-layer graphene*. These concepts will

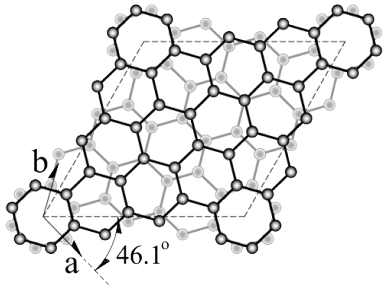

Figure 46: Schematic $\sqrt{13}\times\sqrt{13}$ $R46.1°$ fault pair unit cell (dashed line). Outlined circles are $R30$ C atoms (**a** and **b** are graphene unit vectors). Gray circles are C atoms in the $R2^+$ plane below, rotated 32.204° from the top plane.

be covered thoroughly in the remainder of this thesis.

Figure 47(a) shows X-ray radial scans through the graphene $(1, 0, \ell)$ rod ($R30$ rod) for different values of $q_z = 2\pi\ell/c$. The two peaks correspond to a normal graphene $(1, 0, \ell)$ surface rod and the other to a graphene surface rod $(1 + \Delta h, 0, \ell)$ with a compressed in-plane lattice constant ($R30$ compressed rod). The peak separation corresponds to an in-plane compression of $\Delta a/a = -0.28 \pm 0.01\%$. It is emphasized that the strain is not due the graphene-SiC lattice mismatch, which would *increase* the in-plane lattice constant. Note also that the compressed and uncompressed $R30$ rod widths are the same, meaning that the ordered domain size of both types of graphene sheets are similar (> 3000Å). Note that this domain size is a lower limit on the graphene quality because graphene grows over the SiC steps, destroying the effective X-ray coherence length. Estimates from Raman and transport measurements indicate that graphene domains are much larger, $4000 - 10,000$Å[11,69] (STM evidence of this will also be shown in the following chapter.) This clearly demonstrates that the compressed graphene is not due to lateral domain boundaries. Proof that the compressed graphene occurs at the rotational stacking fault boundaries is presented below. Note that the $R2^{\pm}$ rod widths [see Fig. 47(b)] are the same as the $R30$ rods, indicating large sheets of this phase as well.

To confirm that the $R2^{\pm}$ rotated and compressed graphene layers are interleaved

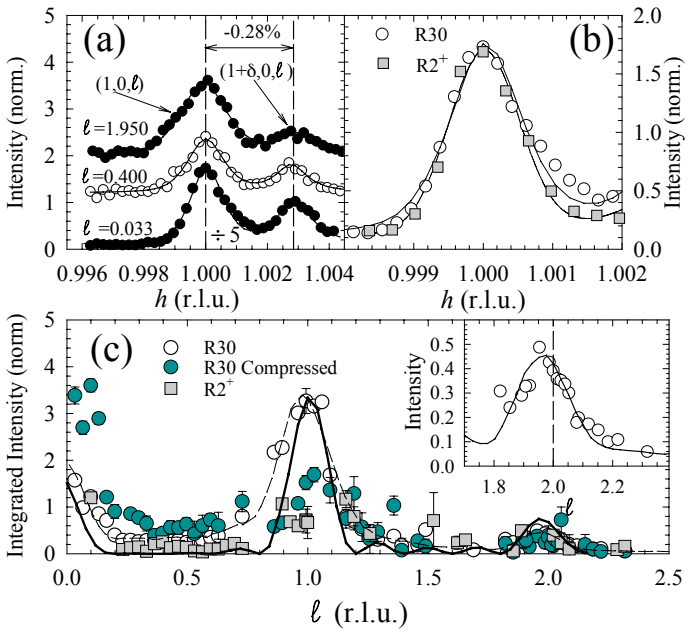

Figure 47: (a) Radial (h) scans through the graphite ($h = 1, 0, \ell$) rod for different ℓ (see Fig. 32). Scans show two peaks corresponding to the normal graphene $(1, 0, \ell)$ rod and a compressed graphene $(1+\Delta h, 0, \ell)$ rod. (b) comparison of radial scans through the $R30$ and $R2^+$ rods at $\ell = 0.1$. (c) Integrated intensity of the $R30$, $R30$-compressed and $R2^+$ rods. Solid line is a fit for 10 AB... stacked graphene layers. Dashed line is a fit for 10 graphene layers with a random rotational fault model. Inset is an expanded view near $\ell = 2$ showing a shift to smaller ℓ (larger interlayer spacing).

in the $R30$ stack, the graphene stacking has been investigated via crystal truncation rod (CTR) analysis. If the different rotational phases existed as isolated domains, we would expect them to be AB stacked. Figure 47(c) shows integrated (radial and azimuthal) intensity modulation of the $R30$, $R30$ compressed and $R2^{\pm}$ rods as a function of ℓ. The modulation period and amplitude are due to the stacking arrangement of films at each respective position in reciprocal space, which is clearly different for each rod. For comparison the expected instrument corrected intensity for a 10-layer AB stacked film (solid line) is shown in Fig. 47(c). While the $R30$ rod may have some characteristic of AB stacking, the $R30$ compressed and $R2^+$ rods do not. This data shows conclusively that the graphene grown on the C-face has rotated graphene sheets interleaved in a multi-layer graphene film.

A better fit to the $R30$ rod intensity can be made using a model where random

rotational faults are introduced into the AB stack with a probability γ. To describe all the data, both an in-plane lattice contraction (the source of the compressed $R30$ rod) and an interplanar expansion of ϵ (with respect to the bulk spacing) is allowed at each fault pair boundary. The interplanar expansion is revealed in the inset of Fig. 47(c) where the experimental peak near $\ell = 2$ is seen to be shifted to a slightly lower value. This expansion ($1.8 \pm 0.3\%$) is similar to azimuthally disordered turbostratic graphite (described in Chap. 2), where rotational faults cause significant interference of π^* states between rotated planes.[14] Note that the C-face graphene films are not turbostratic since their domain sizes are much larger than the best turbostratic graphite samples ($\lesssim 1000$Å) and are not randomly oriented.[142] Also note that the interplanar expansion coupled with the in-plane contraction at the fault is consistent with graphite's negative in-plane and positive out-of-plane thermal expansion.[143] A weaker bond caused by the interlayer expansion at the fault allows the in-plane bonds to contract.[143,144]

A fit to the $R30$ rod intensity with $\gamma = 0.38 + .07/- .03$ and $\epsilon = 0.06 \pm 0.02$Å for a 10-layer film is shown in Fig. 47(c). This model fits the data better than simple AB stacking. γ has also been estimated from the relative intensities of all three rods at $\ell = 0$. This is because in a random model at $\ell = 0$ the diffraction intensity is proportional to the square of the probability of finding each type of rotated layer: $I_{R30}/I_{R30\text{comp}} = 4(1-\gamma)^4/\gamma^4$ and $I_{R30}/I_{R^-} = (1-\gamma)^2/\gamma^2$. This method gives slightly higher fault densities, $\gamma = 0.5 \pm 0.06$. Measurements from samples with graphene films thicknesses of 8, 10 and 30 layers give consistent values of γ ranging from 0.45-0.6.

Yet another type of fit to the inter-layer expansion that uses a random turbostratic fault model[138] to estimate γ found that $\gamma = 0.4$. In other words, after every $1/(1-\gamma) = 1.6$ graphene sheets, a stacking fault occurs in the film. This is within the error bars of the fit in Fig. 47(c) described above.

Not to worry, this is not the end of the story for rotational domains in graphene

on SiC. The R30, $R2^-$ and $R2^+$ phases will be revisited in the following chapter, when convincing real-space STM evidence regarding their existence is presented. Although these structures were the first commensurate cells to be observed on C-face graphene and thus provided a great starting place for further studies, by now many other commensurate cells have been observed. These intriguing structures will be the focus of the remaining chapters.

5.4.4 Other Results

Tilted Bulk Rods

One discovery made during X-ray studies of EG samples that isn't necessarily publishable on its own merit is nonetheless worth mentioning. Highly tilted surface rods are observed on EG/SiC samples that were not H_2 etched. They appear as narrow peaks that pass through radial scans around the graphene in-plane lattice position as well as through specular reflectivity scans. It was possible to track these tilted diffraction rods up ℓ in both types of data. They were found to lean at angles of $\sim 14°$ from the surface normal. A plot following the position of one such tilted rod as it moves up in ℓ (Q_r vs. Q_z) is shown in Fig. 48. The degree of tilt for this rod is 14.3° from the surface normal and was the same measured on other samples. The presence of these tilted rods indicates that the unetched samples have a high density of SiC surface facets. While the graphene film itself is most likely not effected by this disorder, dangling SiC bonds associated with these defects should influence the charge transfer between the SiC interface and the first few graphene layers.[109]

Surface Oxides After X-ray Exposure

Subsequent to X-ray beam exposure, all samples studied exhibit an intense silicon oxide peak in AES scans and increased diffuse scattering in LEED data. These effects seemed to be slightly less pronounced in samples that were exposed to X-rays under UHV conditions and *later* exposed to air than in samples exposed to the X-ray beam

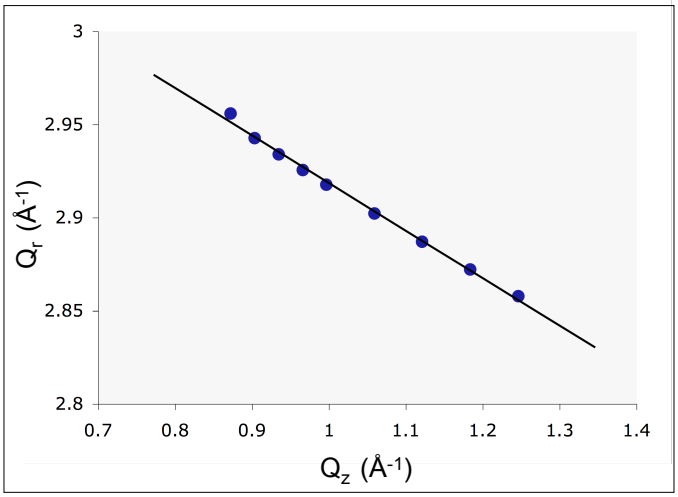

Figure 48: A plot following the radial position (Q_r) of a tilted bulk SiC surface diffraction rod as it moves up in Q_z. The degree of tilt is 14.3° from the surface normal.

for extended periods of time in air at atmospheric conditions. X-rays are known to produce ozone in air. It is possible that the presence of ozone at the surface may actively leach out Si from the SiC bulk or interface region. The resulting surface material is most likely SiO_2. This could be an accelerated version of a similar oxide-producing process that occurs when EG samples are exposed to air for long periods of time. A set of AES scans taken before and after X-ray exposure are shown in Fig. 49. In order to attain a surface scan without any trace of this oxide, the samples were heated to a minimum of 1120°C under UHV conditions. This is phenomenon is important to take notice of now, as the characteristic evolution of these surface contaminants over time must be understood and addressed before reliable, lasting devices can be produced.

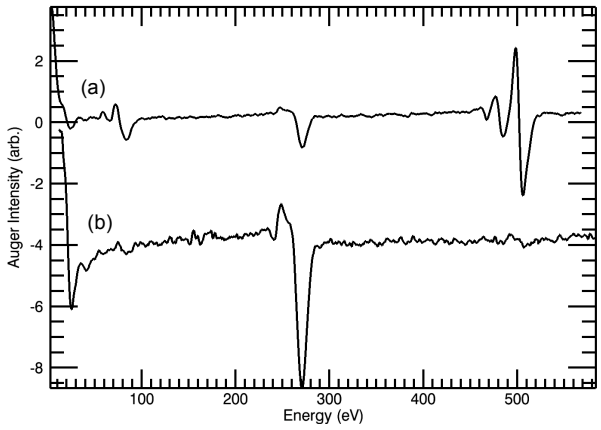

Figure 49: Auger electron spectroscopy scans taken before (b) and after (a) exposure to synchrotron X-rays. The carbon peak at 270 eV remains at the same position, but decreases significantly in amplitude. After exposure a sizable, shifted Si peak is seen at 83eV. The usual Si position is near 92eV, but a known to shift to lower energies occurs when it is part of an oxide compound. A large O peak is also seen at 506eV. In this particular sample, it appears that trace silicon oxides may have been present before X-ray experiments, but that is not always the case.

CHAPTER VI

SCANNING TUNNELING MICROSCOPY ON EPITAXIAL GRAPHENE

6.1 Introduction to STM

The development of the scanning tunneling microscope (STM) was an exciting step in the world of surface science. It provided novel real space images of individual surface atoms within a crystal lattice. Although the ability to attain atomic resolution was realized by Binnig *et al.*[145] in 1983 (and earned them the 1986 Nobel Prize in Physics), evidence of quantum tunneling in a metal-vacuum-metal system was presented as early as 1971.[146] Today, commercial scanning tunneling microscopes are commonplace in surface science research groups. It is generally advantageous to operate an STM in UHV where it is possible to have clean surfaces and tips, however in-air and even in-liquid commercial apparatuses are available.

6.1.1 Theory of Operation

Scanning tunneling microscopes employ quantum mechanical tunneling to establish an electrical current between a clean, conductive surface and atomically sharp metal tip. Quantum mechanics predicts the wavelike nature of the electron, which has a wavefunction that decreases exponentially with distance from its associated parent atom.[147] If an electron on an atom at the surface of a metal tip is held close to a planar conducting surface, there is a small, but finite probability that the electron will tunnel across the vacuum barrier. If a small bias voltage is applied between the tip and surface, the probability of tunneling increases and a directional path is provided such that an electrical current will flow. The amount of tunneling current is

exponentially dependent on the physical separation of the tip and sample, as described by the following one dimensional relation (as in Tersoff and Lang[148]) :

$$I \propto e^{-2\kappa Z} \tag{25}$$

where Z is the barrier width and the parameter κ is defined by:

$$\kappa^2 = \frac{2m(V_B - E)}{\hbar^2}. \tag{26}$$

Here, V_B is the potential barrier, E is the energy of the electron state, and m is the electron mass. For simplicity, V_B can be considered as constant across the gap and if no bias voltage is applied, equal to the vacuum level. In this case, for electron states at the Fermi level, $(V_B - E)$ is the work function for the material (on either side of the barrier.) This is shown schematically in Fig. 50(a). The Fermi levels of the tip and sample are shown, with a vacuum barrier between them. In Fig. 50(b), a bias voltage, V has been applied between the sample and tip. Emission can occur for electrons in the shaded region, as those filled states have available empty states to tunnel into. Although not explicitly mentioned in Eq.(25), this aspect of the diagram indicates the dependence of tunneling current on the local density of states near the surface of the probed material. The tip will tunnel into available states and map the electron density. Because electrons are (for the most part) localized around atoms, scanning the tip at a fixed tunneling current will result in topographic imaging as the tip adjusts its height to maintain constant current. The exponential relationship between tip height and tunneling current is what makes the atomic scale resolution possible. Usually κ is ~ 1Å, which, by Eq.(25), leads to over an order of magnitude change in current with 1Å of tip height variation.[148]

The diagrams in Fig. 50 only illustrate the scenario for *electron* tunneling, although *hole* tunneling can occur in a similar way. When a positive sample bias is applied, electrons tunnel from tip to sample and an "empty state" image is taken, whereas a negative sample bias results in "filled state" imaging because electrons flow

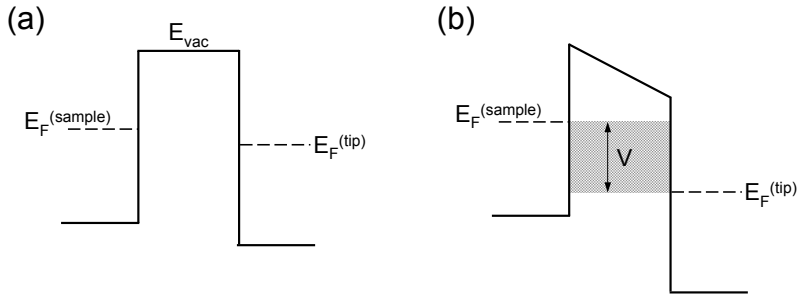

Figure 50: A schematic of potential barriers between tip and sample for vacuum tunneling. (a) When no bias is applied, the difference in Fermi levels (E_F) is simply the difference in the work functions of the materials. (b) A voltage is applied and there is a corresponding voltage bias across the tunneling gap. The shaded region indicates where tunneling can occur. Taken from [148].

from sample to tip. It is often advantageous to try both kinds of imaging and even ramp through a series of positive to negative bias voltages. This is referred to as bias dependent imaging and can provide information about changes in the density of states at various energies away from the Fermi level.

One must be extremely careful when interpreting STM images, as there are many possible sources of noise and false imaging. Noise can be greatly reduced by ensuring that the apparatus is mechanically and electronically isolated. Mechanical vibrations generally appear as low frequency noise in the tunnel current, usually due to contact between some part of the sample stage and the rest of the experimental system. Electronic noise often has a frequency of 60Hz (or another harmonic) and can be due to local electromagnetic fields from nearby laboratory equipment. Depending on the frequency of the noise, it can sometimes be misinterpreted as atomic corrugations or other periodic features on the surface. Another possible source of false imaging is a multiple tip. An ideal STM tip is sharpened down so that there is a single atom at the apex of the tip. Such perfection is difficult to achieve and one often ends up with tips that have two or more sharp terminations. If more than one of these is close enough to the sample surface to induce an appreciable tunnel current, multiple

imaging can occur.

Although suitable for the scope of this thesis, the theory described above has been summarized from well established and accessible literature on principles of STM operation. For a more thorough and rigorous treatment, the reader is referred to the following reviews: Stroscio *et al.*[148] and Golovchenko,[147] as well as seminal experimental[145] and theoretical[149] STM publications.

6.1.2 Instrumentation: RT System

The room temperature STM that was used to acquire all data taken for this thesis is a homemade instrument that was constructed as part of the thesis work of Paul Quesenberry.[79] Extensive detail regarding the design of all mechanical components and electronic circuits that make up the STM can be found in his dissertation, but a brief overview will be given here. The tip scanner and sample mount reside on an isolated stage attached to an 8-inch Conflat flange. There are two vibration damping stages, each equipped with suspension springs and magnetic plates held close to planar conductors. These steady any motion of the sample stage via internal resistance in the conductors that respond to motion-induced eddy currents.

The tip scanner is comprised of two concentric cylindrical piezoelectric tubes that sit inside an insulating block. It is responsible for rastering the tip across the sample during imaging. The outer tube controls the z-motion of the tip (extension and contraction along the tip axis) and the inner tube controls the x, y motion in the plane of the sample surface. The user inserts the 1mm tungsten tip shank into a socket on the scanner using one of the UHV chamber wobble sticks. The x, y and z tip movement is then activated by voltages applied to the tubes by computer control.

A mounted sample can be inserted into wire arms attached to the stainless steel sample block using the wobble stick as well. The sample block is mounted on three tungsten carbide balls which enable sliding over the flat stainless steel base. Once

the sample is inserted into the holder, a piezo-actuated Burleigh inchworm attached to a copper slab is used to bring the sample block close to the tip. Coarse motion is controlled by a handheld joystick, but the final approach is run by a computer program that cycles between small forward steps and holds for tunneling signal detection. Once an approach is complete, the inchworm steps the copper slab back such that there is no longer any electrical or mechanical contact. The sample then remains in place throughout the experiment as the tip moves during data collection.

All STM data acquisition is managed by an electronic circuit called the STM servo. This is truly the "bread and butter" of the microscope operation because it is responsible for maintaining a desired tunnel junction between the tip and sample. Via a feedback loop, the servo monitors the tunnel current and correspondingly adjusts the tip-sample separation. Thus, the result is a topographic image, as described in the previous section. This explains STM operation in *constant current* mode, which was always used for data taken in this work. The servo is also capable of holding the tip in place at any time (during image acquisition or not) and ramping the bias voltage to record a tunneling spectrum. Known as scanning tunneling spectroscopy (STS), this technique will be the focus of Sec. 6.4.

Tip Preparation

Access to sharp STM tips is crucial to high quality tunneling data. All STM tips used for this work were made of fine (0.004 to 0.010 inch diameter) polycrystalline tungsten wires spot welded to 1mm diameter tungsten shanks. Once the spot weld was secure, tips were transferred to a tip etching station. This included an optical microscope for magnified viewing, a wire loop on which a thin bubble of 1M KOH solution was mounted, a metal tip holder, and small power supply. The wire loop/KOH bubble served as one electrode and the tungsten tip was the other. Once the tungsten wire was carefully inserted in the center of the loop, a voltage was applied and

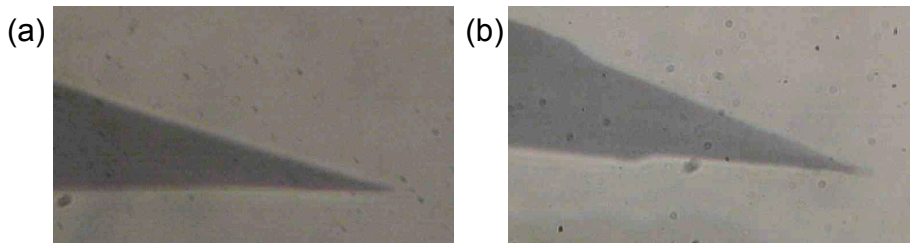

Figure 51: Optical micrographs (400x magnification) of tungsten tips made via KOH chemical etching. Tip (a) is of poorer quality; it only exhibited field emission spots at an 800V threshold. Tip (b) is a sharper tip that exhibited a 300V threshold. Note the inability to focus on the end of tip (b). This is a good indicator of a sharp tip.

chemical etching of the tungsten occured. This very closely follows the method of Melmed[150] and a detailed diagram can be found there. For this work, the thin tungsten wire was quickly etched all the way through at a higher voltage setting to cut the wire down to an appropriate length ($\leq \frac{1}{2}$ inch). The resulting dull termination was etched off by (1) the nearby formation of a "neck" in the tungsten wire and (2) low voltage etching coordinated with physically pulling the KOH drop away from the tip. Because the thinnest tungsten region etches fastest, this resulted in sharp tip formation.

Two examples of tips made by this method are shown in Fig. 51. Optical micrographs at 400x magnification enable the comparison of tip quality. The tip seen in (b) is a sharper tip than the one in (a). An indicator of a good tip is the inability to optically focus on the end of the tip, such that it always looks a bit blurry. This is demonstrated in Fig. 51(b). Once inserted into the UHV chamber, tips were heated via electron bombardment and their field emission threshold voltages were checked. This involved pointing the tip at a microchannel-plate image intensifier and applying a negative high-voltage bias to the tip. Sharper tips have a higher concentration of electric field lines normal to the end of the tip and will therefore emit electrons at lower threshold voltages. Electron emission is detected as electrons strike the image

intensifier and make a bright spot. Tips that have field emission threshold voltages below 1kV are useable, but it is ideal to have a tip that emits below 500V. The tip in Fig. 51(a) had a threshold voltage of 800V, while the one in (b) exhibited a 300V threshold. Scanning could sometimes improve the threshold voltages of tips, but it was more often the case that extended use made them dull. In that case, tips could be transferred out of the chamber and re-sharpened at the etching station by the formation of a new neck and following the directions above.

Now that the STM apparatus and components have been explained, the emphasis throughout the rest of this chapter will be on STM data taken on epitaxial graphene.

6.2 Topography of Epitaxial Graphene

Chapter 4 focused on the initial characterization of EG/SiC samples using a few standard, relatively quick surface science techniques: LEED, AFM and AES. In this section, further surface characterization attained via Scanning Tunneling Microscopy (STM) will be outlined for all sample types. Because STM is a very localized probe, the focus will be on atomic scale structures.

6.2.1 Si-face (0001) Topography

UHV Grown Graphene

The vast majority of literature available on epitaxial graphene focuses on the Si-face UHV grown material. The true epitaxy observed makes this material attractive to researchers, despite significant growth challenges. As mentioned during the discussion of AFM data, a large number of substrate pits form during graphitization. This can be seen in Fig. 52, a large scale STM topograph illustrating the degree of substrate roughening. Essentially all of the steps seen on this scale are SiC steps. In this image there are two particularly deep pits visible. Atomic scale defects found in this

material have been characterized by Rutter *et al.*[151]

The largest continuous graphene domains seen on the Si-face UHV-grown material are generally anywhere between 500 - 1000Å in the longest dimension. No matter the extent of the continuous domain, the graphene films grow continuously over other graphene sheets and features in the SiC surface. This can be seen in the work of Seyller *et al.*[97] and Rutter.[34] In general, the largest area domains reside on the top of the surface, so that graphene layer terminations are always observed underneath larger continuous sheets. Step edges between the first graphene layer ("layer 1") and the reconstructed SiC surface ("layer 0") are frequently observed, but layer 2 terminations atop layer 1 have not been observed. Instead, layer 2 tends to flow uninterrupted over the more common layer 1/layer 0 edges, transforming the feature to a layer 2/layer 1 boundary such that one graphene layer is shoved under the larger top graphene sheet.

It is possible to identify different numbers of Si-face graphene layers by carefully inspecting the corrugation of the surface.[34,51,102,128] Layer 0 is perhaps the most obvious to identify, as it has a semiconducting gap and must be imaged at higher bias voltages. Lowering the tip-sample bias will result in a tip crash, rather than imaging of the honeycomb lattice. There is a characteristic SiC (6×6), 18Å periodicity of this layer that matches the "quasi cell" shown in Fig. 7. It is linked to the $(6\sqrt{3}\times6\sqrt{3})$R30° reconstruction described at length in Sec. 4.2. Layer 1 is also corrugated with this 18Å periodicity, but to a lesser degree. Riedl *et al.*[51] suggest an approximate 50% decrease in corrugation amplitude for each successive graphene layer. Imaging layer-1 graphene at low bias voltages should result in observation of the unmistakable graphene honeycomb lattice. Successive layers display the graphene lattice more prominently and the (6×6) corrugation becomes less and less discernible.

Angle Resolved Photoemission Spectroscopy has been performed on the UHV grown Si-face material by a number of research groups.[37,97,136] This technique uses

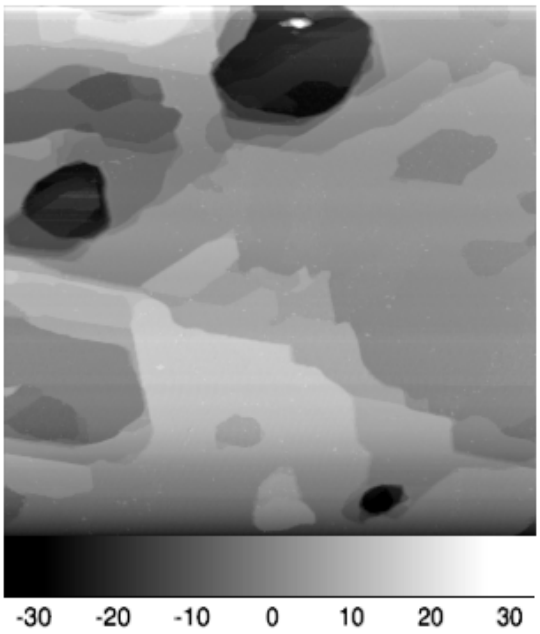

Figure 52: A large scale (300nm × 300nm) STM topograph of 1-2 layer epitaxial graphene grown under UHV conditions on a 6H-SiC(0001) substrate. The sample bias and constant tunneling current were -3V and 100 pA, respectively. Note the prevalence of substrate steps and pits over the entire surface The scale bar displays shading contrast with height in Å.

synchrotron radiation to induce electron emission. Measurements of the outcoming electron energy and direction provide information about the band structure of the probed material. In regions of the sample dominated by layer 1 graphene, a linear dispersion relation is observed for majority carriers at the K-point of the Brillouin zone. This is the band structure expected for an isolated sheet of graphene. As soon as a second layer of graphene grows, the dispersion relation becomes parabolic, as expected for AB... stacked bilayer graphene. The X-ray data presented in the previous chapter is consistent with this conclusion.

In the literature there are many claims made regarding the ability to distinguish different stacking arrangements in STM topographs. It is often asserted that single layer (non-AB... stacked) graphene is characterized by the six carbon atoms in the honeycomb lattice being imaged symmetrically. It then follows that if the A and B

sublattices are imaged with different intensities, the film is classified as mulitilayer graphene (AB... stacked). While there is a correlation between the type of imaging seen and the type of stacking present, it is not this simple. There is a bias dependence involved in the type of imaging seen, such that the different symmetries only come out at lower bias voltages. Above a certain threshold bias, all epitaxial graphene can be imaged as a symmetric honeycomb lattice.[101] This is an area that deserves further experimentation, but for a current, thorough treatment of this and other Si-face graphene phenomena, the reader is referred to the thesis work of Greg Rutter[34] and Nikhil Sharma.[102]

Furnace Grown Graphene

Over the past year or two, increased attention has been given to Si-face graphene growth in the RF furnace. This material was initially charaterized in Sec. **??**. Much larger SiC substrate terraces are observed when this growth method is used and the pits that litter the UHV grown Si-face are completely absent (see the AFM scan presented in figure 19.) Continuous graphene domains up to $1\mu m$ have been observed,[102] two orders of magnitude larger than what was seen on the UHV-grown material. Atomic scale in-plane defects are still observed on this surface, but with lower frequency.[102]

A new, possibly problematic feature appears on the surface of these films. The "tiger stripe" features mentioned in chapter IV can be examined more closely with STM. Figure 53 is a 120 nm $\times$ 120 nm STM topograph of one of these features. in AFM images, the "stripes" appear to be larger, continuous structures, but here seem to be made up of small clusters of amorphous carbon, possibly in a precursor stage before island nucleation. Some preliminary work has been done indicating that heating these samples in UHV causes reduction of these features.[102] Further experiments are planned to investigate whether this is indeed the case.

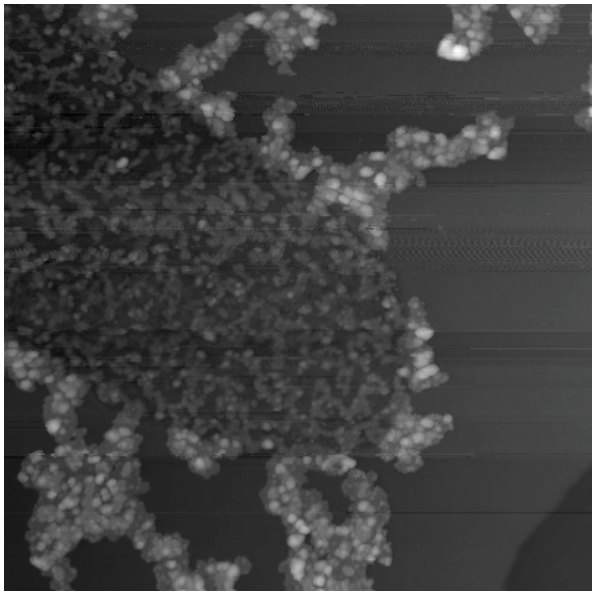

Figure 53: A 120nm × 120nm STM topographic image of 1-2 layer epitaxial graphene grown in the RF furnace on a 4H-SiC(0001) substrate. The sample bias and constant tunneling current were +3V and 100pA, respectively. The sample was annealed at 1075°C in UHV before STM data was taken.

Collaborators at the University of California, Berkeley have performed ARPES measurements on graphene samples made in the RF furnace as well. They found that, just as with the UHV grown material, single layer regions exhibit linear dispersion, but multilayer films show parabolic dispersion. The only difference between the two growth methods was that the lineshapes observed for the furnace grown material were sharper, consistent with larger, more ordered graphene domains. All studies to date indicate that the interface region of the furnace-grown Si-face material is the same as the UHV-grown Si-face material, although careful comparisons have yet to be performed.

6.2.2 C-face $(000\bar{1})$ Topography

UHV Grown Graphene

STM images were displayed in Fig. 21 taken from a typical UHV-grown C-face film produced by Varchon *et al.*[109,152] Imaging on this material can often be difficult due to the presence of the large pleats mentioned earlier, as well as nanocap and tube structures that are often prominent.[80,153,154] A replica of Fig. 21 with enhanced contrast in the graphene plane is presented in the rotational stacking section below, as it shows evidence that the rotated graphene layers exist on the UHV grown C-face material as well.

Furnace Grown Graphene

The quality of C-face furnace grown graphene is far superior to any other type of epitaxial graphene made to date. As mentioned in Sec. 4.3.2, the original substrate step density is preserved and continuous graphene films as large as 20μm have been observed.[81] In agreement with X-ray data, STM surface topographs show that these films are extremely flat. Figure 54 is a $0.4\mu m \times 0.4\mu m$ STM topograph that illustrates a tiny height variation (about 0.6Å) over this large area. Many images like this were taken throughout experiments done for this thesis. It was difficult to find graphene domain terminations, as most steps observed were SiC substrate steps covered with continuous sheets of graphene. One example of this is seen in Fig. 55, a 3D-rendered STM topograph of atomically resolved graphene growing over a 30Å SiC step. This corresponds to three SiC unit cell heights for the 4H polytype. (The image shown does not display the top of the step, but the full step height was measured other topographs.)

On this material, carbon atoms within the honeycomb lattice sometimes image as three-fold symmetric and sometimes image as six-fold symmetric. This is surprising in light of the unique rotational stacking that decouples individual graphene sheets.[48]

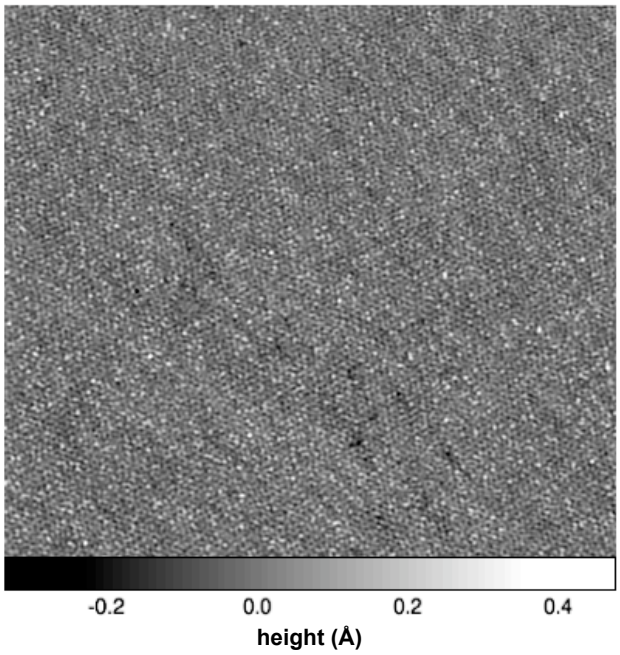

Figure 54: A 0.4μm $\times$ 0.4μm STM topograph on 4H-SiC(000$\bar{1}$) furnace-grown EG with only a 0.6Å height variation over the entire image. The sample bias and constant tunneling current were +3V and 100 pA, respectively. The periodic structure seen is not the atomic graphene lattice; it has a much larger 55Å period. This may be a superstructure due to independently rotated graphene sheets or could possibly be an interface reconstruction. A zoom-in taken on this terrace is displayed in Fig. 57.

One would expect that if the symmetry of the lattice is conserved, only six-fold symmetric imaging would occur. As of now, there have not been any studies targeted at understanding this discrepency, but it could mean that sometimes an AB... stacked bilayer appears at the surface. In the cases that six-fold symmetry is seen, the top layer would instead be a rotated layer. An example of the six-fold symmetric honeycomb imaging is shown in Fig. 56. Note the similar level of intensity seen at each corner of the graphene hexagons. For comparison, look to Fig. 58(c) in the next section, where three of the six carbon atoms in the honeycomb lattice are imaged with far greater intensity than the others. This indicates that the A and B graphene sublattices are distinguishable, despite the fact that there is a clear evidence that a

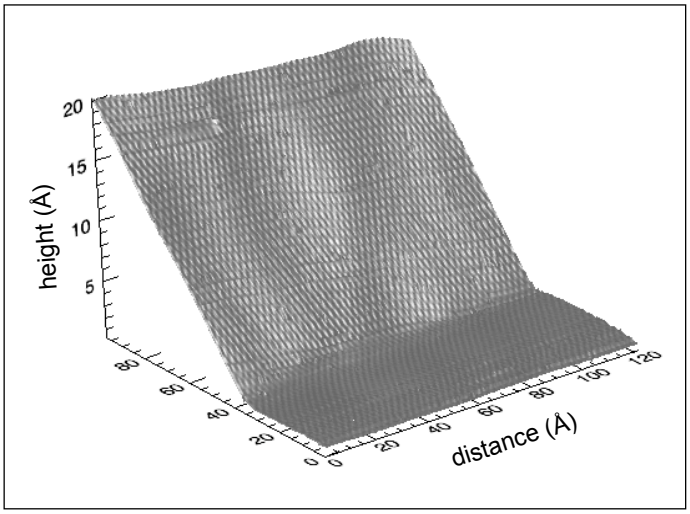

Figure 55: 3D rendered atomically resolved STM topograph of C-face furnace grown graphene growing over a 30Å SiC step. (This image does not display the top of the step, but the full step height was measured other topographs.) The sample bias and constant tunneling current were -0.6V and 100 pA, respectively.

rotated layer is present near the surface. (Unique superstructures which indicate the presence of rotated sheets are the topic of the next section.) As suggested above, this may mean that the top bilayer is AB... stacked, with a rotated layer three down from the surface.

Very little is known about the buried EG/SiC interface of this material. No real space images of single or few layer graphene on the SiC$(000\bar{1})$ face have ever been published, likely because thin films are hard to grow. As explained in Chap. Ch:PR, graphene grows very quickly on the C face so it is difficult to halt growth at fewer than five layers. Nonetheless, some of the STM images taken on furnace-grown graphene exhibit fairly disordered long range periodic structures that could be part of an interface reconstruction. An example of such a structure is seen on a large scale in Fig. 54 and at higher resolution in Fig. 57. When a Fourier transform is performed on the large scale image, a six-fold symmetric structure becomes clear. It

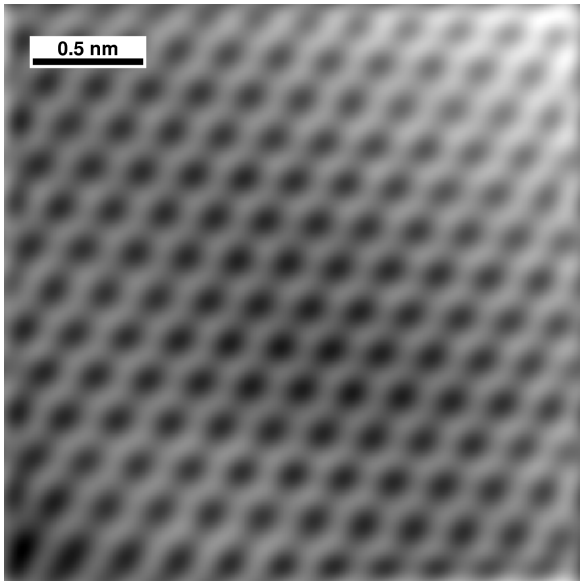

Figure 56: A 4nm × 4nm STM topograph of the graphene honeycomb lattice taken at +0.5V sample bias and 100 pA constant current. The sample was RF furnace-grown on 4H-SiC(000$\bar{1}$).

has a 55Å periodicity. In the high resolution image the atomic corrugation is seen superimposed on the subsurface structure. The periodicity of the subsurface structure is not so evident on this scale, but the centers of the raised circular features are indeed approximately 5.5nm apart. It is possible that this image was taken on a region of the surface that had fewer graphene layers. Although the distributions of layer heights measured on the furnace grown C-face samples are far broader than on the Si face, some thin layers still exist. For example, more than 25% of one furnace-grown film with an average of 5.85 layers contains domains with two graphene layers or less.

The most fundamental difference between Si- and C-face graphene films grown via both methods is their stacking character. C-face films always exhibit a unique kind of stacking, characterized by interleaved rotated layers. Clear STM evidence of this is presented in the following section.

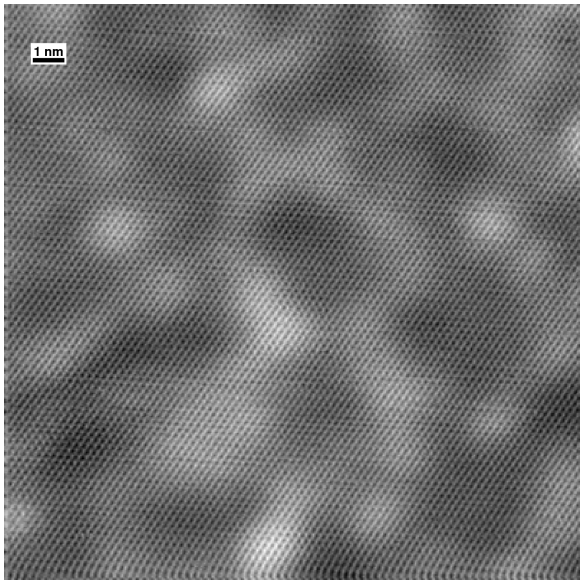

Figure 57: A closer look at the terrace shown in Fig. 54. A 20nm ×20nm STM topograph taken at +0.5V sample bias and 100 pA constant current.

6.3 Rotational Stacking

X-ray diffraction data was presented in the previous chapter which demonstrated the existence of unique stacking faults on the C-face material. In this section additional evidence will be presented that supports this conclusion in the form of real space STM images.

6.3.1 STM Evidence of Rotational Stacking

As was explained in Sec. 5.4.3, C-face EG is comprised of rotated graphene sheets interleaved every two to three layers throughout the film. If this is the correct stacking model for these samples, then a rotated fault pair should often occur near the surface of the graphene. STM scans should be able to provide evidence of the rotations because commensurate cells give rise to superstructures with periodicites defined by the commensurate cell length. An example of one of these superstructures was shown in Fig. 46 and is reproduced here in Fig. 58(a). The pattern seen in the figure is called a Moiré pattern, a term generally used to describe interference patterns created when two structures with different periods are overlayed. Technically speaking, the

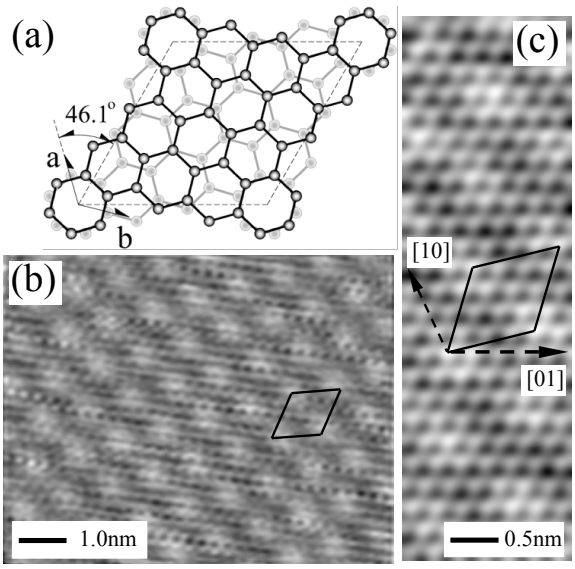

Figure 58: (a) The schematic $(\sqrt{13}\times\sqrt{13})_{\mathrm{G}}\mathrm{R}46.1°$ superlattice formed by a $\beta = 32.204°$ rotated fault pair unit cell (dashed line) seen in Figure 46. (b) STM image of C-face graphene showing a periodic superlattice with a $(\sqrt{13}\times\sqrt{13})_{\mathrm{G}}$ cell. (c) High resolution STM image (100 pA constant current, -0.8V sample bias) of the $(\sqrt{13}\times\sqrt{13})_{\mathrm{G}}\mathrm{R}46.1°$ unit cell (solid line) and the principle graphene directions (dashed lines). For display, Gaussian smoothing was used in (b) to reduce the atomic corrugation (15-20pm peak-to-peak in the raw data) relative to the superlattice ($\sim 8pm$ peak-to-peak). From [48].

STM is not able to see through the top layer of atoms, so a true "Moiré" pattern is not observed. However, superstructures that arise due to high coincidence positions in the commensurate cell *should* appear. Indeed, these characteristic features are seen all over the C-face furnace grown material. The exact source of the image contrast is not yet well understood.

Figure 58(b) and (c) show STM topographs that exhibit the kind of superstructures described above. The supercell is outlined in black and the dashed lines indicate the principle graphene directions. In fact, the 8.9Å supercell period and 46.1° angle between the supercell and top graphene lattice are precisely those expected for a graphene bilayer pair with one layer rotated 30° and the other layer rotated +2.2° (or −2.2°) from the SiC substrate. They therefore have a 32.2° (or 27.8°) rotation with

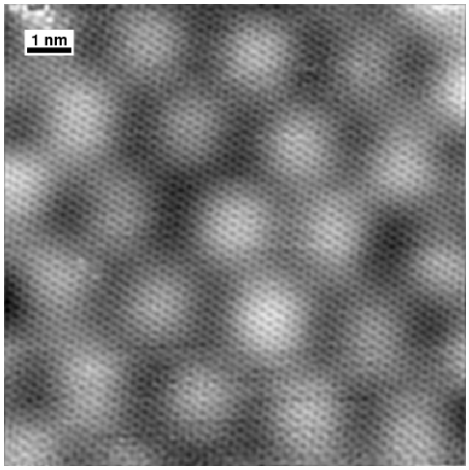

Figure 59: A 12nm × 12nm STM topograph of another Moiré-like pattern taken at +0.6 sample bias and 100 pA constant current. The sample was RF furnace-grown on 4H-SiC(000$\bar{1}$).

respect to one another. This matches the angles measured by SXRD and provides further evidence that there is some registry with the SiC substrate. It is important to emphasize that this particular structure is associated with commensurate cells formed by both a graphene-graphene rotation *and* a graphene-SiC rotation. This could be a condition that guides the selection of rotation angles. The following chapter focuses on possible rationale for the observed angles.

In STM we are searching for graphene-graphene commensurate cells because only features of the first couple of layers can be detected. The 46.1° cell illustrated in figure 58 and discussed at length during the X-ray data analysis was the first supercell observed, but to date many more have been discovered. The following additional supercell periods have been measured on various terraces on two different samples: 25Å, 30Å, 40Å, 55Å, and 60Å(±2Å.) The 8.9Å supercell had the smallest cell area of any observed so far. An image taken on the next largest cell (25Å superperiod) is shown in Fig. 59.

A total of 13 continuous graphene domains $\geq 1\mu m$ in length were studied on two different furnace-grown C-face samples for this work. Seven of the domains exhibited clear superstructures like those seen in Figs. 58 and 59. The other six showed

subsurface structure; three with ordered subsurface features (as seen in Figs. 54 and 57) and three with seemingly random subsurface features. Therefore, a little more than half of the domains studied exhibited Moiré-like superstructures. In most cases, the continuous domains were so large that their edges were not encountered during a standard 1-3 day run (single tip approach.) There were two exceptions: in one case a region without any superstructures became one that did exhibit superstructure as the graphene flowed over a SiC step. The other involved the only grain boundary found during these experiments. On one side of the grain boundary there was a 30Å superperiod and on the other side a 25Å superperiod.

Moiré-like supercell patterns are also seen on UHV-grown C-face graphene, although the continuous domains are far smaller, causing an abundance of grain boundaries. This indicates that there is something inherent in the structure at the interface and/or SiC bulk termination that allows the rotation of graphene films as they grow. The same STM topograph displayed in Sec. 4.3.1 is reproduced in Fig. 60, but with enhanced contrast in the graphene surface plane. Superperiod structures characteristic of rotational stacking are seen in approximately half of the domains in the field of view, a similar ratio measured on the furnace-grown material.

6.3.2 Rotational Stacking on HOPG surfaces

It should be noted that superperiod patterns attributed to rotational stacking have also been observed on freshly cleaved highly oriented pyrolytic graphite (HOPG) surfaces. It is believed that the cleaving process can tear single sheets of graphene, overlaying them in rotated orientations. Thus, the major difference is that on HOPG these features are due to a surface rotation only, whereas the rotational stacking faults on EG are seen throughout the graphene stacks. A great number of studies were performed on these cleaved structures in the 1990's. For further information the reader is referred to the extensive topical review by Pong and Durkin.[155]

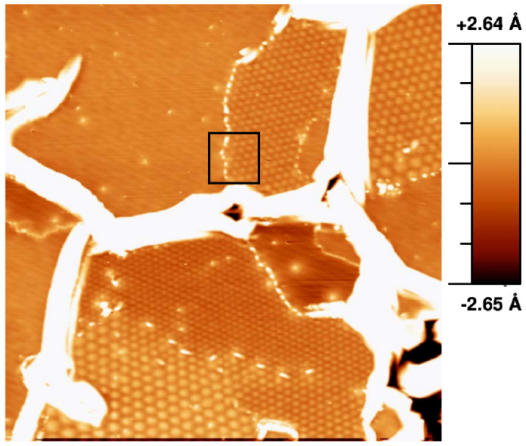

Figure 60: 150nm ×150nm scanning tunneling microscopy image acquired on a 6H-SiC(000$\bar{1}$) EG sample taken at 1.0V sample bias and 100 pA tunneling current. This topograph was also displayed in Fig. 21, but here there is an enhanced contrast in the plane. Note the abundant grain boundary features and various periodic superstructures. Taken from [109].

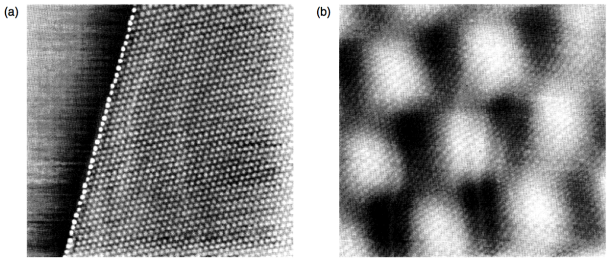

Figure 61: (a) 160 nm×160 nm scanning tunneling microscopy image acquired on a freshly cleaved HOPG sample. The bright spots correspond to a 38Å superperiod structure. (b) 10 nm × 10 nm STM image displaying both the atomic lattice and the larger superperiod. Taken from [155].

6.4 Scanning Tunneling Spectroscopy (STS) on Epitaxial Graphene

6.4.1 STS Basics

As mentioned in section 6.1.2, the STM servo is capable of a hold and voltage-ramp procedure that results in the acquisition of a tunneling spectrum. This is known as scanning tunneling spectroscopy (STS). For the system used in this work, data was taken in the form of an I-V measurement and later differentiated using a Savitzky-Golay algorithm[156] to obtain dI/dV curves. The ratio of the differentiated

conductance and the measured conductance, $\frac{dI/dV}{I/V} = \frac{d\ln I}{d\ln V}$ corresponds closely to the sample's local density of states.[157] Therefore, theoretical DOS calculations can be compared to STS data and local band structure information can be obtained. This was done with data taken on a furnace-grown C-face EG sample and the preliminary results are explained in the following section. One important note is that in this type of analysis, the tunneling transmission probability has not been taken into account. The result is that electronic sample states that do not overlap with tip sample states (for example, states localized near atomic cores) are not probed.[157]

6.4.2 STS Experiments on C-face EG

Although preliminary, STS experiments done for this thesis have provided interesting results. An STM tip was placed in the center of a large continuous graphene domain on a furnace-grown C-face sample. Imaging in the region revealed a ~ 60Å Moiré-like superstructure across the entire domain (with symmetric imaging of all six honeycomb atoms,) so it can be assumed that a rotated stacking fault was close to the surface. The servo was programmed to take STS spectra at six programmed z-direction tip extensions. Recording spectra at many z positions covers a larger energy range of the local density of states, in this case allowing the sample bias to span from -3V to +3V in each set of spectra. Over 200 sets of spectra taken on a small portion of the graphene domain were averaged to attain the $d\ln I/d\ln V$ spectrum displayed in Fig. 62(a). When compared to calculations of the density of states of graphite,[158] it is clear that basic features are similar. Figure 62(b) is taken from a study by Campanera *et al.*[158] in which *ab initio* density of states calculations are performed on graphite stacks with different surface bilayer stacking faults. While the small differences between different stacking terminations are beyond the resolution of room temperature STS (see comparisons made in [158],) it is encouraging to see that theory and experiment share most prominent features. The two large peaks have been identified as Van Hove

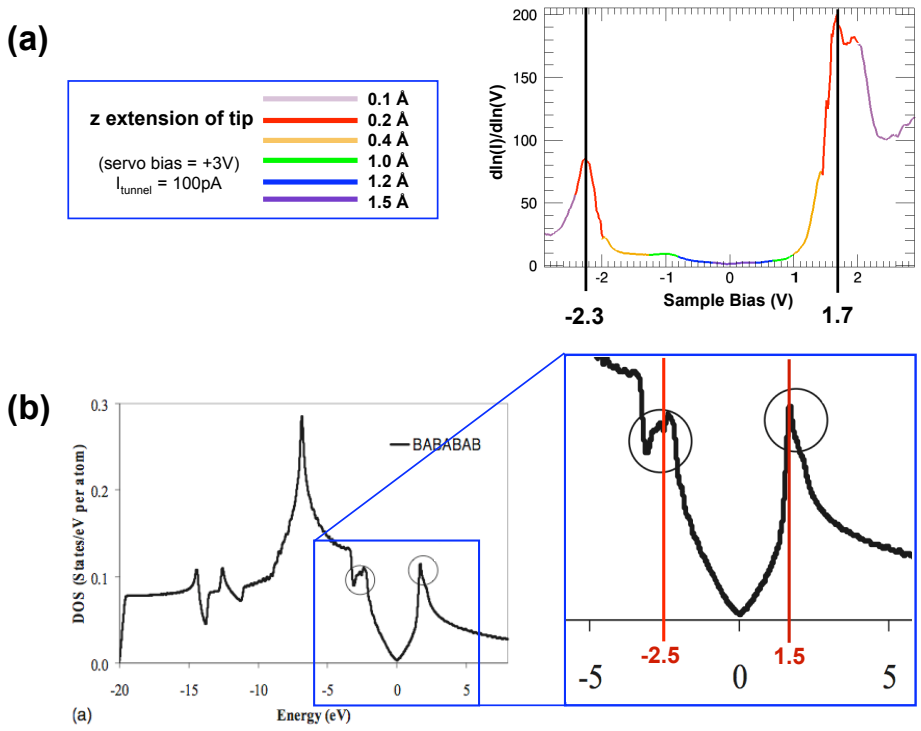

Figure 62: (a) Average STS spectrum acquired on furnace-grown C-face graphene. A series of z-direction tip extensions allowed a large range of bias voltages to be probed and stitched together. (b) *Ab initio* density of states calculation performed on graphite, taken from [158]. Note the similar large scale peaks observed, which have been identified as Van Hove singularities. There is an unexplained shift in both peak positions from theory to experiment.

singularities, predicted to appear in graphite, which correspond to broadening of the band structure away from the K-point.

The differences observed between theory and experiment are worth noting. There is an unexplained, but identical shift in both peak positions. This could possibly be attributed to tip effects, which are generally not well understood. It was, in fact, a goal of this particular data set to seek out any influences of the tip. There is also a noticeable kink in the STS spectrum near a sample bias of -1V which is not seen in the theoretical calculation. The fact that the data was taken on epitaxial graphene, rather

than HOPG, could certainly be a source of differences. Finally, thermal broadening is evident in the experimental data due to the spectra being taken at room temperature.

Further STS experiments on varied stacking terminations on Si- and C-face epitaxial graphene and other graphites could provide interesting information regarding differences in electronic structure. Hopefully this work can provide a point of reference for such future studies.

CHAPTER VII

ANALYSIS OF OBSERVED EPITAXIAL GRAPHENE ROTATION ANGLES

This chapter takes a comprehensive look at the different angles of rotation observed on C-face epitaxial graphene. Two types of commensurate structures are considered, graphene-graphene cells and graphene-SiC cells.

7.1 Commensurate Structures

7.1.1 Graphene-Graphene Commensurate Cells

There are a large number of graphene-graphene commensuration angles other than $30\pm2.204°$. All commensurate rotations can be calculated when the vector $n\mathbf{a}_{\mathrm{G}}+m\mathbf{b}_{\mathrm{G}}$ in one sheet equals the magnitude of the vector $n_1\mathbf{a}_{\mathrm{G}}+m_1\mathbf{b}_{\mathrm{G}}$ in the second sheet (n, m, n_1 and m_1 are integers). Defining $\ell=n^2+m^2-nm$, the relative rotation angle β of these commensurate sheets is given by:

$$\cos\beta(\text{mod. } 60°) = \frac{2m_1m+2n_1n-m_1n-mn_1}{2\ell}. \tag{27}$$

The commensurate structure formed by the rotated sheets is a $(\sqrt{\ell}\times\sqrt{\ell})_{\mathrm{G}}\mathrm{R}\theta$ unit cell where θ is the angle between the super cell formed by the rotated pair and the $(1\times1)_{\mathrm{G}}$ graphene unit cell. θ is given by:

$$\cos\theta(\text{mod. } 60°) = \frac{2m_1-n_1}{2\sqrt{\ell}}. \tag{28}$$

Remember that a rotation angle of $\beta=60°$ gives a $AB..$ graphene pair. Figure 63 shows a set of commensurate rotations when $\ell<64$. The rotation angles are plotted for display purposes using an arbitrary metric; their inverse unit cell size $(\ell\sqrt{3}/2)^{-1}$. The actual energy cost of these rotated pairs has only been estimated for two of the

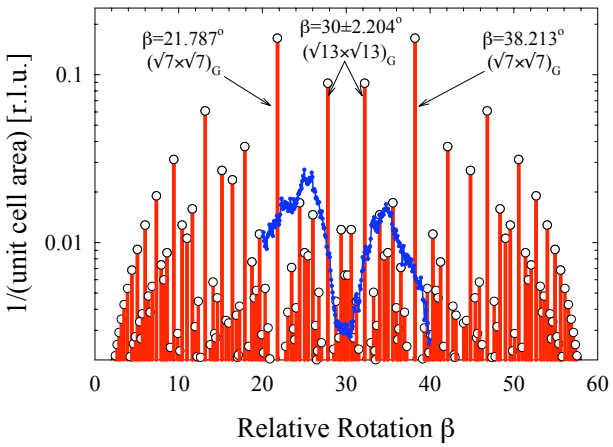

Figure 63: Commensurate graphene-graphene rotations for $\ell < 64$. The rotations are ranked according to the inverse of their $(\sqrt{\ell} \times \sqrt{\ell})_{\rm G}{\rm R}\theta$ unit cell area; $(\ell\sqrt{3}/2)^{-1}$. The $(\sqrt{13} \times \sqrt{13})_{\rm G}$R46.1° cell ($\beta = 30{\pm}2.204°$) and the $(\sqrt{7} \times \sqrt{7})_{\rm G}$R49.1° cell ($\beta = 30{\pm}8.213°$) are marked. (red lines and circles) an SXRD experimental distribution of rotations for a 25-layer C-face graphene film.

many commensurate cells: $(\sqrt{13} \times \sqrt{13})_{\rm G}$R46.1° cell and the $(\sqrt{7} \times \sqrt{7})_{\rm G}$R49.1° cell in Fig. 63. Theoretical calculations find that the larger $(\sqrt{13} \times \sqrt{13})_{\rm G}$R46.1° cell has the lower energy of the two by about 0.2-0.3meV/atom.[141,158] An experimental distribution of rotation angles, measured by SXRD, is shown for comparison. Note that the experimental distribution shows a preference for angles slightly larger and smaller than 30°.

As discussed in the previous two chapters, SXRD and STM experiments have shown that multilayer graphene grown on the C-face has a high density of rotational stacking faults consisting of these commensurate graphene sheet pairs.[48] Figure 58(b) and (c) showed STM images of $(\sqrt{13}\times\sqrt{13})_{\rm G}{\rm R}(\pm 46.1°)$ modulation of the graphene lattice from a C-face film. SXRD experiments determined that the stacking structure is not *AB..* stacked. Rather, the films contain many rotational fault pairs interleaved in the multilayer graphene film (approximately one fault every 1.6-2.5 layers).[48] This is consistent with the additional X-ray reflectivity estimates described above.[66] The majority of these graphene-graphene faults are rotated approximately 30° apart.

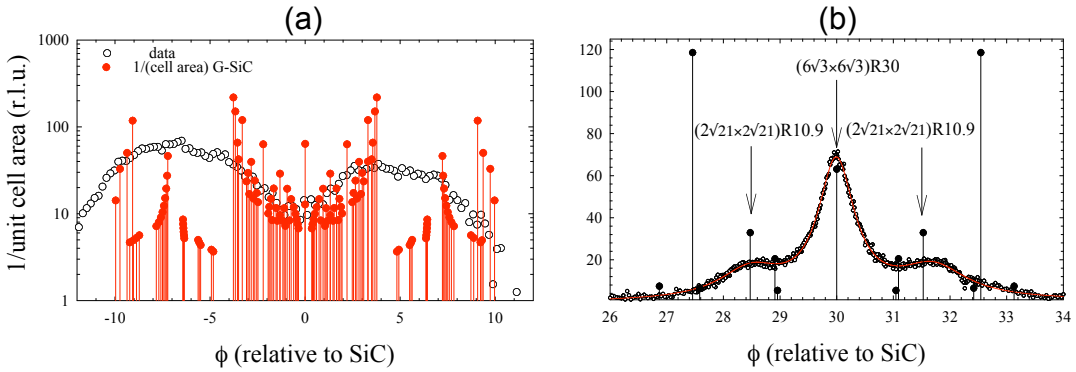

Figure 64: Commensurate graphene-SiC rotations near (a) $\phi = 0$ and (b) $\phi = 30$. The rotations are ranked according to the inverse of their commensurate unit cell area. SXRD experimental distributions of rotations for a 25-layer C-face graphene film are overlaid in both plots. The X-ray data was taken on the same sample for which LEED data is shown in Fig 23(b). Note that in (a) a log scale is used for intensity & inverse cell area. The angle distribution near 30° is sample independent, but near 0° may depend on the step orientations on the starting substrate wafer (Refer to discission in Sec. 4.3.2.)

7.1.2 Graphene-SiC Commensurate Cells

As thoroughly covered in Sec. 2.3.1, there are *also* a great number of graphene-SiC (nearly) commensurate cells. One set of these structures was just reviewed as a graphene-graphene commensurate pair: the $(\sqrt{13}\times\sqrt{13})_{\mathrm{G}}\mathrm{R}(\pm 46.1°)$ fault pair is created when of two of the graphene-SiC commensurate pairs (30° and ±2.204° with respect to the SiC) stack on top of one another. In order to further evaluate the relevance of *additional* graphene-SiC commensurate structures, plots can be made similar the one shown in Fig. 63, but now with graphene-SiC commensurate cells plotted by the same inverse cell area metric. Such a plot is found in Fig. 64 for rotations near (a) $\phi = 0°$ and (b) $\phi = 30°$. All rotation angles, ϕ are defined as in Sec. 4.3.2.

Note that there are far fewer graphene-SiC commensurate cells near $\phi = 30°$ than near $\phi = 0°$. The X-ray data is also more symmetric and sharply peaked in the 30° region, with maxima centered on or near commensurate cells. In fact, the sum of the

area under the peaks at $\phi \approx 31.5°$ and $\phi \approx 28.5°$ is roughly equal to the area under the peak at $\phi = 30°$. The fact that the intensity aligns well with the few commensurate cells available is consistent with the notion that the SiC drives the selection of rotation angles. It is also interesting to note that the angle distribution observed near 30° is sample independent, which is not the case near $\phi = 0°$. Here the alignment between peak angles and commensurate cells is not so straightforward, likely because there are so many more graphene-SiC commensurate cells in this region. (Although they are not nearly as abundant as the graphene-graphene commensurate cells shown in Fig. 63.)

The X-ray scan overlaid in Fig. 64 was taken on the same sample from which the LEED pattern in Fig. 23(b) was recorded. It is again interesting to note how different the intensity distributions are near $\phi = 0$ when the more detailed X-ray azimuthal scans (Figs. 45 and 64(a)) from the different samples are compared. The data from Fig. 45, with clearly peaked intensity at $\phi = \pm 2.204°$, exhibits a definite link between the graphene-SiC commensurate cells and the chosen rotations. Additional experiments must be done to further analyze the rotational distributions on other samples taken from different SiC wafers. The step direction, edge termination, or step density could all be important factors.

There is still enough evidence to conclude that a highly directional graphene-SiC interaction makes production of these faults more ubiquitous, while somehow maintaining the flatness of the graphene sheets. How this is accomplished is not understood. Assuming that each new C-face graphene layer grows at the SiC/graphene interface as observed for Si-face films, it is possible that stoichiometry changes as successive SiC bi-layers are exposed during graphene growth act as new angular templates for the next graphene layer. Why rotations near 0° and 30° are selected has yet to be determined. It is interesting to note that all LEED images taken from UHV grown C-face films (see Fig. 20) show intensity not only near $\phi = 30°$ and 0°, but

also near $\phi = 15°$. At least one group saw a similar intensity distribution for C-face UHV grown graphene,[152] while yet another saw a more continuous ring peaked only at $\phi = 30°$ and $0°$.[154] As suggested during the examination of LEED images in Sec. 4.3.2, it is possible that SiC step edges influence the growth direction of a graphene layer. This may explain the asymmetry of the experimental distribution of angles in Figs. 63 and 64(a).

7.2 Effect on Electronic Structure

As discussed in Sec. 2.2.1, the electronic properties of graphite (and multi-layer graphene) depend on the precise stacking order of the graphitic films. It was long believed that the only way to maintain the unique 2D Dirac nature of the carriers in graphene was to physically isolate a single atomic layer. The work done for this thesis in conjunction with studies done by Georgia Tech collaborators[12,48] prove otherwise.

Far-infrared transmission measurements[12,159] on C-face films ranging from 3 to 60 graphene layers paradoxically show that these multilayer films behave like undoped single-layer graphene. This was initially very surprising, since graphitic *AB..* stacking breaks the equivalency of the carbon sublattice atoms in a graphene sheet.[28,33] While *AA..* stacking faults might explain these results, the SXRD data from furnace grown C-face films have shown that these types of faults are not present in any appreciable fraction in the multilayer film.[66] *AA..* or *ABC..* stacking faults produce inter-layer *contraction*,[17] contrary to the large average graphene inter-layer *expansion* measured by SXRD.[66] Thus, because of the presence of these unique stacking faults, the electronic properties of C-face multilayer films should be very different from those of *AA..*, *AB..* or *ABC..* graphite.

For the R30/R2$^{\pm}$ fault pair in Fig. 58(a) there are only 2 atoms/sheet out of 52 in the $(\sqrt{13}\times\sqrt{13})_{\mathrm{G}}\mathrm{R}(\pm 46.1°)$ cell that are in high symmetry positions, i.e. atom-over-atom sites. This suggests weak interplanar interactions in the fault pairs that help to

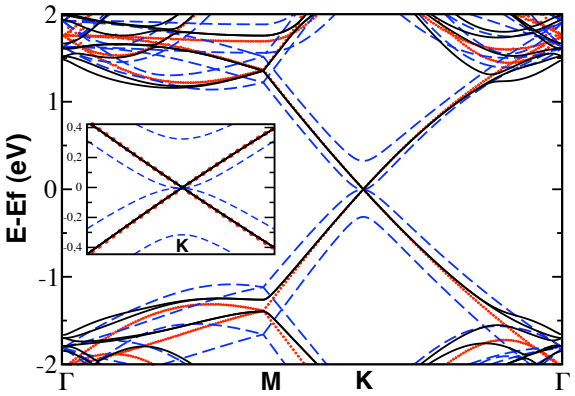

Figure 65: Calculated band structure for three forms of graphene. (i) isolated graphene sheet (dots), (ii) *AB..* graphene bi-layer (dashed line) and (iii) R30/R2$^+$ fault pair (solid line). Inset shows details of band structure at the K-point. From [48].

preserve the symmetry of the graphene sheet.[48,160,161] Figure 65 compares *ab initio* band structure calculations[48] for an isolated graphene sheet, a graphene bi-layer with Bernal $AB\ldots$ stacking and the exact bilayer rotational fault pair of Fig. 58(a). The Γ K M direction shown is the $(\sqrt{13}\times\sqrt{13})_{\rm G}{\rm R}\pm 46.1^\circ$ cell high symmetry direction. The main differences in the electronic structure of the three graphene forms show up in the dispersion curves near the K-points. The band structure for an isolated graphene sheet shows the linear gapless dispersion of the π bands at the K-point. The normal Bernal stacking of graphene breaks the sublattice symmetry, giving rise to splitting of the π bands with a corresponding change to a parabolic shape and a lower group velocity.[33] With the rotated fault, the linear dispersion is recovered near the K-points. This dispersion is identical to the graphene dispersion (same Fermi velocity) and clearly shows that in the rotated layers, the atoms in the A and B sublattices are identical. More recent work done by Latil *et al.*[161] demonstrates that even in an *ABA'..* stacked trilayer, (here the prime denotes a rotated film) linear dispersion is maintained near the K-point.

This type of *ab initio* theoretical calculation convincingly ties together the rotational stacking,[48] enhanced Dirac carrier signal for thicker films[12] and the superior mobilities measured in the C-face furnace grown material.[42] So, it turns out that

nature has chosen to stack abundant forms of graphite in the only two ways that do *not* maintain linear dispersion.

CHAPTER VIII

CONCLUSIONS

8.1 Summary of Results

Structural characterization of epitaxial graphene grown on the (0001) and (000$\bar{1}$) surfaces of SiC has shown that there are vast differences in film quality dependent on both the growth method and polar face selected. UHV growth induces a great deal of substrate roughening and leads to small coherent graphene domains. Evidence that supports this conclusion has been presented from surface X-ray diffraction (SXRD), scanning tunneling microscopy (STM), low energy electron diffraction (LEED), and atomic force microscopy (AFM) experiments. On the other hand, when SiC is heated for graphene growth in an RF induction furnace under low vacuum conditions, the substrate pits seen on the Si-face during UHV growth are no longer a problem and far larger graphene domains form on both faces. The reasons for such vast differences in graphene quality are not fully understood, but two factors have been identified that are certainly involved. One is the higher Si desorbtion temperature under furnace conditions. This results in a higher graphitization temperature on both polar faces, although the difference is far greater on the C-face. A later onset of silicon removal may allow for a more favorable ordering of the SiC surface before graphene forms. A second factor is the furnace environment, as the presence of O_2 (and possibly excess Si) likely aids in the removal of Si from the surface. Because the partial pressures of silicon oxides near the surface are far lower under UHV conditions, their removal is more disruptive in the UHV environment.

Vast differences in film quality on the two polar faces have also been addressed. Independent of the growth environment, graphene layers form far faster on the (000$\bar{1}$)

C-terminated surface. The furnace-grown C-face material is far superior to any other epitaxial graphene films grown to date. Continuous graphene domains are routinely measured at greater than 1μm. Because the kinetics of Si removal through the graphene film must be the same on each face, the differences must exist at the EG/SiC interface. The slower rate of graphene growth on the Si-face translates to rougher films because Si clusters can get trapped in the interface region, leading to twinning and defect structures. As discussed below, the interface structure on the opposing faces has been shown to be significantly different.

Epitaxial graphene has been demonstrated to be extremely robust. Transfer of samples in air does not substantially affect the film quality. On both polar faces of SiC and in both growth environments graphene grows continuously over SiC substrate steps and other graphene steps, much like a carpet lays atop and conforms to a staircase. SXRD and STM data indicate that epitaxial graphene exhibits about an order of magnitude larger surface corrugation on the Si-face, which is likely due to the roughness and periodicity of the interface, "layer-0". The graphene grown on the C-face in the RF furnace is extremely flat.

X-ray specular reflectivity measurements have shown that the EG/SiC interface region (also referred to as "layer-0") extends deeper into the bulk on the Si-face than the C-face. Both faces contain at least one highly corrugated layer *or* a bilayer/single layer plus adatom region. The possible Si- and C-face models can be found in Figs. 37 and 42, respectively. On the Si-face, the last SiC bilayer (directly below layer-0) is substantially altered from the SiC bulk densities and inter-layer spacings. On the C-face, this bilayer is much more bulk-like. The interface can be conclusively identified as carbon rich in both cases, but due to the fact that X-rays distinguish between different atoms only through their atomic form factors, it is possible to find more than one model that fits the reflectivity data by exchanging C and Si atoms and multiplying the atomic density by the ratio of their form factors. For this reason,

X-ray analysis alone cannot determine the final interface structure. The spacings and densities on both faces suggest the presence of a mixture of sp^2 and sp^3 bonded carbon.

Reflectivity results show that the first structural graphene layer is tightly bound to the interface region on both polar faces. D_o, the spacing between layer-0 and layer-1, is 2.32 ± 0.08Å on the Si-face and 1.62 ± 0.08Å on the C-face, in both cases far less than the spacing between planes of $AB..$ stacked graphite, ~ 3.35Å. These measurements indicate that layer-1 is more tightly bound on the C-face than the Si-face, consistent with *ab initio* electronic calculations[133,134] and previous inverse photoemission and XPS experiments.[55,104,107] The interface layer and possibly the tightly bound first graphene layer provide a buffer between the bulk SiC and the rest of the graphene film, thus allowing the graphene to be electronically isolated. Because the interface structure is not yet fully understood it remains uncertain which layer most fully exhibits the "buffering" characteristics.

One parameter that can be accurately measured via X-ray reflectivity is D_G, the average interlayer spacing between graphene planes (beyond layer-1.) On the Si-face, $D_G = 3.35 \pm 0.01$Å, the same as Bernal stacked graphite. This is consistent with ARPES[37] and STM[101] data that indicate Si-face EG grows as $AB..$ stacked graphite beyond the first layer. On the furnace-grown C-face samples, $D_G = 3.368 \pm 0.005$ Å, 0.42% larger than $AB..$ stacked graphite. While this difference sounds small, it has an enormous effect on the behavior of the graphene's electronic carriers. The expanded interlayer spacing translates to a stacking fault an average of every two to three layers in the C-face graphene films. These stacking faults decouple adjacent graphene sheets and allow the symmetry of an isolated graphene layer to be maintained.

The nature of the C-face stacking faults described above has been identified through SXRD crystal truncation rod (CTR) analysis and STM topography. By simply glancing at a C-face EG low energy electron diffraction (LEED) pattern, one can

tell that there are rotated graphene domains present. Surface X-ray analysis shows that on the furnace-grown material there are graphene domains rotated either near 30° or spread on either side of 0° with respect to the SiC lattice orientation. The 30° rotated stacks always appear along with graphene sheets that exhibit a contracted in-plane lattice constant. It is reasonable to expect that sheets with a contracted lattice will appear at stacking faults, as weaker out-of-plane bonds caused by the interlayer expansion can result in an contraction of the in-plane bonds. The continuous domain sizes for the contracted graphene, as well as the graphene at each rotated position are essentially identical. This, along with the expanded average interlayer spacing, implies that the rotated sheets are interleaved, rather than independent $AB..$ stacked regions.

However, there is further compelling evidence that the rotated films are interleaved. By measuring the diffracted intensity modulation of the graphene CTRs, information can be obtained about the stacking order of the graphene films. Data sets from different graphene domains (at two rotated positions and at the in-plane contracted lattice position) were compared to each other and to the calculated intensity modulation expected for $AB..$ stacked graphite. The results clearly show that *none* of the graphene domains are $AB..$ stacked and that they all have a distinctly different (and complex) stacking character. The final piece of evidence was the observation of real-space periodic superstructures characteristic of rotated bilayer pairs in STM topographs. Thus, due to: (1) the large rotated domains of similar size, (2) expanded average interlayer spacing, (3) non-Bernal stacking order, and (4) STM evidence of surface rotated layers, it is certain that furnace grown C-face graphene is comprised of interleaved rotated sheets.

Azimuthal X-ray scans and LEED patterns were examined in order to gain insight into any possible rationale for the rotation angles chosen by the C-face graphene sheets. When compared to the rotation angles that define commensurate rotations

between the SiC lattice and the graphene lattice, a loose correlation was found. Evidence of a connection was more convincing near the 30° rotated position, as all samples studied consistently lock into three angles that coincide with graphene-SiC commensurate cells.

Experimental studies have shown that C-face graphene grown under both UHV[38] and furnace[12,159] conditions exhibits linear electron dispersion and Dirac-like carrier behavior not only in the first graphene layer, but throughout the entire 3D film. Mobilities are also always much higher on the furnace-grown C-face graphene.[42] The interleaved rotated stacking described above explains how this is possible. In order to clearly link the two effects, *ab initio* band structure calculations were performed on a unit cell of one of the exact bilayer pairs observed by SXRD and STM.[48] Indeed, the results show that the band structure of a single isolated graphene sheet and a rotated bilayer pair are essentially indistinguishable.

Therefore, while Si-face graphene is truly epitaxial and always rotated 30° from the SiC lattice, beyond the first layer it grows as Bernal-stacked graphite. C-face graphene, on the other hand, is only loosely epitaxial and grows as interleaved, rotated stacks. This unique stacking decouples individual graphene sheets and preserves the Dirac-like linear dispersion relation, making EG electronics possible even for a multilayer material.

8.2 Areas for Future Study

The study of epitaxial graphene on SiC is still relatively new and thus full of opportunity for future experimentation. The vast majority of research being done still focuses on the (0001) Si-face, thus one popular direction is to attempt to improve the quality of these Si-face films. Very recent work has shown that Si-face furnace growth under an argon flux at atmospheric pressures leads to large graphene domains and ordered substrate step structure.[162] Trials with different furnace environments would

be interesting, as well as further attempts at UHV "cleaning" of RF furnace-grown Si-face films. Regarding the quality of RF furnace-grown C-face films, further STM studies of the pleats and/or tubes that form are important. If their structure is better understood, advances can be made in minimizing their formation.

Very little STM work has been done to characterize the interface structure of the C-face material. Because thinner films are difficult to grow, possible strategies for accessing the interface are (1) setting up a heating gradient across a sample surface such that graphitization increases steadily over the length of the sample or (2) mechanical removal of surface layers via peeling.

Experiments using other surface science techniques must be performed to nail down accurate interface models for each polar face. One technique that would provide interesting results is scanning Auger electron mapping. Instruments are now available with resolution on the order of 10nm. Auger peak height comparisons could be made between zero, one, and two layer films. Changes in Si and C peak size would enable identification of the ratios of chemical species in the interface. Such information would help to rule out certain X-ray interface models introduced in this thesis.

Further modeling must be done to narrow down the precise rotational stacking order of C-face films. More thorough characterization of rotation angles observed in STM topographs before X-ray analysis on each sample would help in this effort. A careful study of observed rotation angles along with wafer miscut angles may indicate a correlation between step density or surface stacking termination with preferred angles.

Finally, there are many further scanning tunneling spectroscopy studies that could be done to further the work begun in this thesis. Comparisons made between STS spectra taken on Moiré and non-Moiré regions would be interesting, as well as comparisons between bright and dark regions of the Moiré-like patterns. Conclusive explanations for the positioning of the imaging contrast have not yet been made.

There will no doubt be a great deal of exciting new research on epitaxial graphene in the years to come.

APPENDIX A

XRD GEOMETRY CORRECTIONS

A.1 Active Area Correction

When the X-ray beam is incident on a sample, there is a threshold angle at which the beam footprint begins to spill off of the sample. Consider the diagram in Fig. 66. x is the length of the sample, L is the length of the beam footprint, and $(d \times w)$ is the cross-sectional area of the incident beam. (w is not depicted, but goes into the plane of the page.) The active area, A, is defined as the sample area illuminated by the beam footprint. From the diagram it can easily be determined that the beam spills off the sample for $\sin\alpha < d/x$. Therefore, the active area can be described by the following:

$$A = \begin{cases} \frac{wd}{\sin\alpha} & \sin\alpha > d/x \\ xw & \sin\alpha < d/x \end{cases} . \tag{29}$$

These expressions will be useful in the following sections.

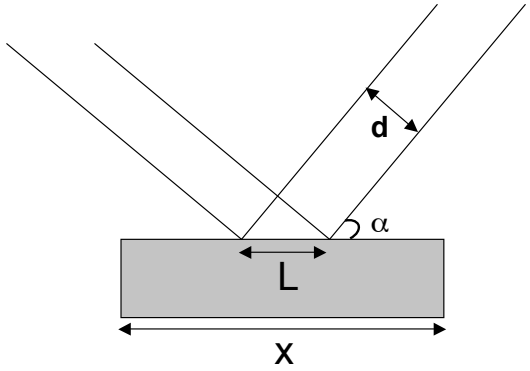

Figure 66: Schematic of the incident beam on the sample (grey.)

A.2 Lorentz Factor: Specular Geometry

The Lorentz factor correction arises when a conversion must be made from a real space integration window defined by the diffractometer to a reciprocal space integration window on a surface diffraction rod. The sources used as outlines for this derivation were Robinson[117] and Vlieg.[120] The geometry for the simpler case of the specular rod is depicted in Fig. 67. The integration window ($dQ_x\ dQ_y\ dQ_z$) must be expressed in terms of real space angles ($d\alpha\ d\beta\ d\gamma$):

$$dQ_x\ dQ_y\ dQ_z = dV = k^2(d\beta\ \times d\gamma)\cdot \mathbf{k}d\alpha = k^3 d\beta\ d\gamma\ d\alpha \sin(2\theta) \tag{30}$$

Note that $d\alpha$ is the angle by which the sample is rocked for reflectivity measurements. Using the above expression for dV, the experimental integrated intensity, E, can be written:

$$E \propto \int I d\alpha\ d\beta\ d\gamma = \frac{1}{k^3 \sin 2\theta} \int I dQ_x\ dQ_y\ dQ_z. \tag{31}$$

If $I(\mathbf{Q})$ is broken into its parallel and perpendicular components with respect to the scattering plane, then $I(\mathbf{Q}) = g(Q_z)\cdot f(\mathbf{Q}_{||})$. Insertion of fundamental leading constants leads to the following expression for E:

$$E = \frac{r_e^2 P|F|^2 A}{A_u k^3 \sin(2\theta)} \int g(Q_z)\ dQ_z \int\int f(\mathbf{Q}_{||})\ dQ_x\ dQ_y. \tag{32}$$

A is the active area defined in Eq.(29), A_u is the area of the crystal unit cell, r_e is the classical electron radius, and P is the polarization factor defined in eq.19. The desired quantity is F(h,k,ℓ), the crystal structure factor. In reflectivity experiments, $Q_z = 2k\sin(2\theta/2)$, so $dQ_z = 2k\cos(2\theta/2)\Delta(2\theta/2)$. Additionally, $\Delta(2\theta/2) = \Delta\gamma$, the acceptance angle of the detector. The function $g(Q_z)$ varies very slowly over the integration window of the detector, so it is possible to approximate:

$$\int g(Q_z) dQ_z \approx g(Q_z) 2k\cos(2\theta/2)\Delta\gamma. \tag{33}$$

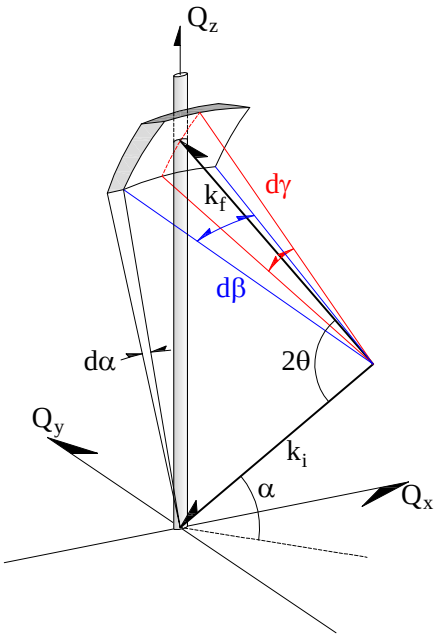

Figure 67: Schematic of the integration window for specular geometry.

After some algebra,

$$\int g(Q_z)dQ_z \approx g(Q_z)\frac{2k\sin(2\theta)\Delta\gamma}{2\sin(2\theta/2)} = g(Q_z)\frac{2k^2\sin(2\theta)\Delta\gamma}{Q_z}. \tag{34}$$

And, again, because $g(Q_z)$ is essentially constant over the integration window of the detector, it will be set equal to 1 for convenience. Therefore:

$$E = \left[\frac{r_e^2 P|F|^2 A}{A_u k}\right]\left[\frac{2g(Q_z)}{Q_z}\right]\Delta\gamma\int\int f(\mathbf{Q}_\parallel)\; dQ_x\; dQ_y. \tag{35}$$

Substituting in for the active area, A, defined in Eq.(29), gives:

$$E = \left[\frac{r_e^2 P}{A_u k}\right]|F|^2\int\int f(\mathbf{Q}_\parallel)\; dQ_x\; dQ_y \begin{cases} \frac{2kwd}{Q_z^2} & \sin\alpha > d/x \\ \frac{xw}{Q_z} & \sin\alpha < d/x \end{cases}. \tag{36}$$

The top expression is for the case that the entire footprint of the X-ray beam fits on the sample and in the bottom expression the beam spills over part of the sample. The term that is left to be integrated is simply a Gaussian or Lorentzian peak integration and is thus just a number. All remaining terms are constants or numbers from the experiment, other than $\mathrm{F}(h,k,\ell)$, the desired quantity.

A.3 Lorentz Factor: Non-specular Geometry

In this section the goal is the same as it was in the previous section, but for off-specular scans. Here, α is the incident beam angle relative to the sample surface and β is the outgoing beam angle relative to the sample surface. They are always held equal: $\alpha = \beta$. $Q_\parallel$ is the component of the momentum transfer vector that lies in the plane of the sample surface, as depicted in Fig. 68. As usual, Q_z is the component that is normal to the sample surface. $\Delta\chi$ is the vertical slit acceptance angle and $\Delta\psi$ is the analyzer acceptance angle. (Both are expressed in radians.) It can be shown that:

$$Q_\parallel = 2k\cos\alpha\sin(\xi/2) \tag{37}$$

And after some algebra, one can obtain:

$$dQ_x\ dQ_y\ dQ_z = dV = dQ_\parallel\ d\psi\ d\chi k^2\cos\alpha\sin(\xi/2) = dQ_\parallel\ d\psi\ d\chi(\frac{k}{2})|Q_\parallel| \tag{38}$$

And again, we would like an expression for E, the experimental integrated intensity. Inserting the proper constants:

$$E = \frac{2r_e^2PA}{kA_uQ_\parallel}\int|F|^2\ dQ_z\int\int f(\mathbf{Q})\ dQ_r\ dQ_t. \tag{39}$$

See the previous section for definitions of all of the constant terms. In this geometry it is convenient to break $\mathbf{Q}_\parallel$ up into Q_r and Q_t, the radial and transverse scan directions (rather than Q_x and Q_y.) Unfortunately, this time all of the angles rotate as scans are taken up the off-specular rods. This means that expressions must be obtained for ΔQ_z, ΔQ_r, and ΔQ_t. One can work through the geometry to obtain:

$$\Delta Q_z = \frac{\Delta\chi\cos\alpha Q_\parallel k}{[Q_\perp^2 + (\cos^2\alpha)Q_\parallel^2]^{1/2}} + \frac{\Delta\psi Q_\perp}{2} \tag{40}$$

$$\Delta Q_r = \frac{\Delta\chi kQ_\perp}{[Q_\perp^2 + (\cos^2\alpha)Q_\parallel^2]^{1/2}} + \frac{\Delta\psi\cos\alpha Q_\perp}{2} \tag{41}$$

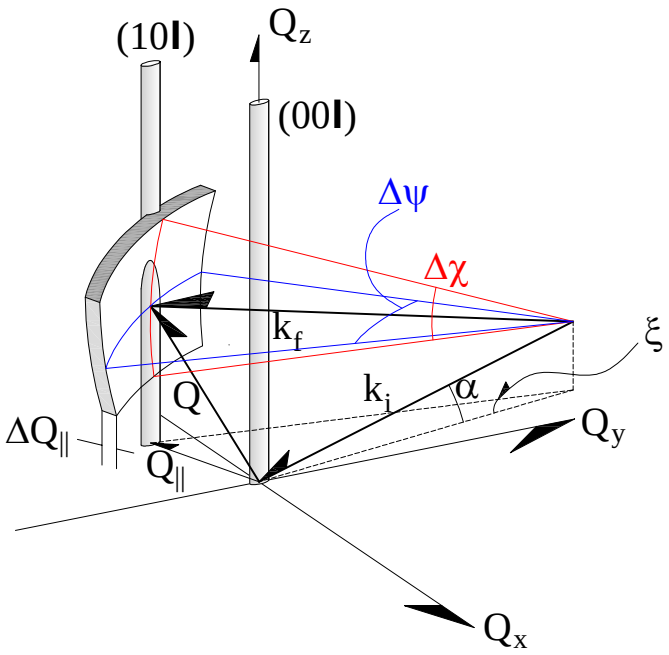

Figure 68: Schematic of the integration window for non-specular geometry.

$$\Delta Q_t = \frac{\Delta\psi}{4k}[-Q_\parallel Q_\perp + (4k^2 - Q_\perp^2)^{1/2}(4k^2 - Q_\parallel^2)^{1/2}] \tag{42}$$

It will also be necessary to address each of the integrals in Eq.39 separately. First, consider the dQ_z term, which is again slowly varying. By assuming $F(h,k,\ell)$ is essentially constant in Q_z, as was done in the previous section, the integral is simplified as seen below:

$$\int |F|^2 \, dQ_z \approx \sum_{\Delta Q_z} F^2 \Delta Q_z \approx F^2(Q_z)\Delta Q_z. \tag{43}$$

Fortunately, $f(Q_r)$ is a simply a peak which will be fit with a number, so it can be set to equal 1. That leaves $f(Q_t)$. Here only a small portion of the peak, ΔQ_t, is being measured over on any given scan and $f(Q_t) = f_o e^{-Q_t^2/2\sigma^2}$, where σ is the full width half maximum of the peak. Thus,

$$\int f(Q_t) \, dQ_t \approx [1/(\sqrt{2\pi}\sigma)]\Delta Q_z. \tag{44}$$

Finally, all of the pieces can be put together to attain E as a function of F^2:

$$E = \left[\frac{r_e^2 P \Delta\psi}{\sqrt{2\pi} 2k^2 Q_\parallel A_u} A\right] \left[-Q_\perp Q_\parallel + \{(4k^2 - Q_\perp^2)(4k^2 - Q_\parallel^2)\}^{1/2}\right] \times \left[\frac{k\Delta\chi \cos\alpha Q_\parallel}{(Q_\perp^2 + (\cos^2\alpha) Q_\parallel^2)^{1/2}} + \frac{\Delta\psi Q_\perp}{2}\right]^2 F^2(Q_z). \quad (45)$$

REFERENCES

[1] C. Berger, Z. Song, T. Li, X. Li, A. Ogbazghi, R. Feng, Z. Dai, A. Marchenkov, E. Conrad, P. First, and W. deHeer, "Ultrathin epitaxial graphite: 2D electron gas properties and a route toward graphene-based nanoelectronics," *Journal of Physical Chemistry B*, vol. 108, no. 52, pp. 19912–19916, 2004.

[2] J. Kedzierski, P.-L. Hsu, P. Healey, P. Wyatt, C. Keast, M. Sprinkle, C. Berger, and W. de Heer, "Epitaxial graphene transistors on SiC substrates," *IEEE Transactions on Elelctron Devices*, vol. 55, pp. 2078–2085, Aug 2008.

[3] K. Nakada, M. Fujita, G. Dresselhaus, and M. S. Dresselhaus, "Edge state in graphene ribbons: Nanometer size effect and edge shape dependence," *Physical Review B*, vol. 54, pp. 17954–17961, Dec 1996.

[4] K. Wakabayashi, M. Fujita, H. Ajiki, and M. Sigrist, "Electronic and magnetic properties of nanographite ribbons," *Physical Review B*, vol. 59, pp. 8271–8282, Mar. 1999.

[5] Y.-W. Son, M. L. Cohen, and S. G. Louie, "Energy gaps in graphene nanoribbons," *Physical Review Letters*, vol. 97, no. 21, p. 216803, 2006.

[6] M. Y. Han, B. Ozyilmaz, Y. Zhang, and P. Kim, "Energy band-gap engineering of graphene nanoribbons," *Physical Review Letters*, vol. 98, no. 20, p. 206805, 2007.

[7] K. S. Novoselov, A. K. Geim, S. V. Morozov, D. Jiang, Y. Zhang, S. V. Dubonos, I. V. Grigorieva, and A. A. Firsov, "Electric field effect in atomically thin carbon films," *Science*, vol. 306, no. 5696, pp. 666–669, 2004.

[8] Y. Zhang, Y.-W. Tan, H. L. Stormer, and P. Kim, "Experimental observation of the quantum Hall effect and Berry's phase in graphene," *Nature*, vol. 438, no. 7065, pp. 201–204, 2005.

[9] K. S. Novoselov, A. K. Geim, S. V. Morozov, D. Jiang, M. I. Katsnelson, I. V. Grigorieva, S. V. Dubonos, and A. A. Firsov, "Two-dimensional gas of massless dirac fermions in graphene," *Nature*, vol. 438, no. 7065, pp. 197–200, 2005.

[10] T. Ando, T. Nakanishi, and R. Saito, "Berry's phase and absence of back scattering in carbon nanotubes," *Journal of the Physical Society of Japan*, vol. 67, no. 8, pp. 2857–2862, 1998.

[11] C. Berger, Z. Song, X. Li, X. Wu, N. Brown, C. Naud, D. Mayou, T. Li, J. Hass, A. N. Marchenkov, E. H. Conrad, P. N. First, and W. A. de Heer, "Electronic

confinement and coherence in patterned epitaxial graphene," *Science*, vol. 312, no. 5777, pp. 1191–1196, 2006.

[12] M. L. Sadowski, G. Martinez, M. Potemski, C. Berger, and W. A. de Heer, "Landau level spectroscopy of ultrathin graphite layers," *Physical Review Letters*, vol. 97, no. 26, p. 266405, 2006.

[13] X. Wu, X. Li, Z. Song, C. Berger, and W. A. de Heer, "Weak antilocalization in epitaxial graphene: Evidence for chiral electrons," *Physical Review Letters*, vol. 98, no. 13, p. 136801, 2007.

[14] Y. Baskin and L. Meyer, "Lattice constants of graphite at low temperatures," *Physical Review*, vol. 100, p. 544, Oct 1955.

[15] R. R. Haering, "Band structure of rhombohedral graphite," *Canadian Journal of Physics*, vol. 36, no. 3, pp. 352–362, 1958.

[16] M. C. Schabel and J. L. Martins, "Energetics of interplanar binding in graphite," *Physical Review B*, vol. 46, pp. 7185–7188, Sep 1992.

[17] J. C. Charlier, X. Gonze, and J. P. Michenaud, "First-principles study of the stacking effect on the electronic properties of graphite(s)," *Carbon*, vol. 32, no. 2, pp. 289–299, 1994.

[18] P. R. Wallace, "The band theory of graphite," *Physical Review*, vol. 71, no. 7, pp. 476–476, 1947.

[19] M. I. Katsnelson and K. S. Novoselov, "Graphene: New bridge between condensed matter physics and quantum electrodynamics," *Solid State Communications*, vol. 143, no. 1-2, pp. 3–13, 2007.

[20] J. C. Slonczewski and P. R. Weiss, "Band structure of graphite," *Physical Review*, vol. 109, pp. 272–279, Jan 1958.

[21] G. W. Semenoff, "Condensed-matter simulation of a three-dimensional anomaly," *Physical Review Letters*, vol. 53, pp. 2449–2452, Dec 1984.

[22] F. D. M. Haldane, "Model for a quantum Hall effect without Landau levels: Condensed-matter realization of the "parity anomaly"," *Physical Review Letters*, vol. 61, pp. 2015–2018, Oct 1988.

[23] N. M. R. Peres, A. H. C. Neto, and F. Guinea, "Conductance quantization in mesoscopic graphene," *Physical Review B*, vol. 73, no. 19, p. 195411, 2006.

[24] F. Guinea, A. H. C. Neto, and N. M. R. Peres, "Electronic states and Landau levels in graphene stacks," *Physical Review B*, vol. 73, no. 24, p. 245426, 2006.

[25] E. McCann and V. I. Fal'ko, "Landau-level degeneracy and quantum Hall effect in a graphite bilayer," *Physical Review Letters*, vol. 96, no. 8, p. 086805, 2006.

[26] J. Nilsson, A. H. C. Neto, N. M. R. Peres, and F. Guinea, "Electron-electron interactions and the phase diagram of a graphene bilayer," *Physical Review B*, vol. 73, no. 21, p. 214418, 2006.

[27] M. Koshino and T. Ando, "Transport in bilayer graphene: Calculations within a self-consistent Born approximation," *Physical Review B*, vol. 73, no. 24, p. 245403, 2006.

[28] B. Partoens and F. M. Peeters, "From graphene to graphite: Electronic structure around the K point," *Physical Review B*, vol. 74, no. 7, p. 075404, 2006.

[29] S. Frank, P. Poncharal, Z. L. Wang, and W. A. Heer, "Carbon nanotube quantum resistors," *Science*, vol. 280, no. 5370, pp. 1744–1746, 1998.

[30] T. Hertel and G. Moos, "Electron-phonon interaction in single-wall carbon nanotubes: A time-domain study," *Physical Review Letters*, vol. 84, pp. 5002–5005, May 2000.

[31] A. Calogeracos and N. Dombey, "History and physics of the Klein paradox," *Contemporary Physics*, vol. 40, no. 5, pp. 313–321, 1999.

[32] A. D. Martino, L. Dell'Anna, and R. Egger, "Magnetic confinement of massless Dirac fermions in graphene," *Physical Review Letters*, vol. 98, no. 6, p. 066802, 2007.

[33] S. Latil and L. Henrard, "Charge carriers in few-layer graphene films," *Physical Review Letters*, vol. 97, no. 3, p. 036803, 2006.

[34] G. M. Rutter, *Scanning Tunneling Microscopy Studies of Graphene on (0001) 4H- and 6H-SiC Surfaces*. PhD thesis, Georgia Institute of Technology, Dec 2008.

[35] S. Y. Zhou, G. H. Gweon, and A. Lanzara, "Low energy excitations in graphite: The role of dimensionality and lattice defects," *Annals of Physics*, vol. 321, no. 7, pp. 1730–1746, 2006.

[36] S. Y. Zhou, G. H. Gweon, J. Graf, A. V. Fedorov, C. D. Spataru, R. D. Diehl, Y. Kopelevich, D. H. Lee, S. G. Louie, and A. Lanzara, "First direct observation of Dirac fermions in graphite," *Nature Physics*, vol. 2, no. 9, pp. 595–599, 2006.

[37] T. Ohta, A. Bostwick, J. L. McChesney, T. Seyller, K. Horn, and E. Rotenberg, "Interlayer interaction and electronic screening in multilayer graphene investigated with angle-resolved photoemission spectroscopy," *Physical Review Letters*, vol. 98, no. 20, p. 206802, 2007.

[38] K. V. Emtsev, F. Speck, T. Seyller, L. Ley, and J. D. Riley, "Interaction, growth, and ordering of epitaxial graphene on SiC(0001) surfaces: A comparative photoelectron spectroscopy study," *Physical Review B*, vol. 77, no. 15, p. 155303, 2008.

[39] T. Ando, A. B. Fowler, and F. Stern, "Electronic properties of two-dimensional systems," *Reviews of Modern Physics*, vol. 54, pp. 437–672, Apr 1982.

[40] K. v. Klitzing, G. Dorda, and M. Pepper, "New method for high-accuracy determination of the fine-structure constant based on quantized hall resistance," *Physical Review Letters*, vol. 45, pp. 494–497, Aug 1980.

[41] K. S. Novoselov, Z. Jiang, Y. Zhang, S. V. Morozov, H. L. Stormer, U. Zeitler, J. C. Maan, G. S. Boebinger, P. Kim, and A. K. Geim, "Room-temperature quantum Hall effect in graphene," *Science*, vol. 315, no. 5817, p. 1379, 2007.

[42] W. A. de Heer, C. Berger, X. Wu, P. N. First, E. H. Conrad, X. Li, T. Li, M. Sprinkle, J. Hass, M. L. Sadowski, M. Potemski, and G. Martinez, "Epitaxial graphene," *Solid State Communications*, vol. 143, no. 1-2, pp. 92–100, 2007.

[43] A. Bauer, P. Reischauer, J. Krausslich, N. Schnell, W. Matz, and K. Goetz, "Structure refinement of the silicon carbide polytypes 4H and 6H: unambiguous determination of the refinement parameters," *Acta Crystallographica A*, vol. A57, pp. 60–67, 2001.

[44] A. Bauer, J. Kraublich, L. Dressler, P. Kuschnerus, J. Wolf, K. Goetz, P. Kackell, J. Furthmuller, and F. Bechstedt, "High-precision determination of atomic positions in crystals: The case of 6H- and 4H-SiC," *Physical Review B*, vol. 57, pp. 2647–2650, Feb 1998.

[45] A. J. Van Bommel, J. E. Crombeen, and A. Van Tooren, "Leed and Auger electron observations of the SiC(0001) surface," *Surface Science*, vol. 48, no. 2, pp. 463–472, 1975.

[46] F. Owman and P. Martensson, "Scanning tunneling microscopy study of SiC(0001) surface reconstructions," *Journal of Vacuum Science & Technology B*, vol. 14, no. 2, pp. 933–937, 1996.

[47] I. Forbeaux, J.-M. Themlin, and J.-M. Debever, "Heteroepitaxial graphite on 6H-SiC(0001): Interface formation through conduction-band electronic structure," *Physical Review B*, vol. 58, pp. 16396–16406, Dec 1998.

[48] J. Hass, F. Varchon, J. E. Millan-Otoya, M. Sprinkle, N. Sharma, W. A. de Heer, C. Berger, P. N. First, L. Magaud, and E. H. Conrad, "Why multilayer graphene on 4H-SiC($000\bar{1}$) behaves like a single sheet of graphene," *Physical Review Letters*, vol. 100, no. 12, p. 125504, 2008.

[49] F. Owman and P. Mårtensson, "STM study of the SiC(0001) $\sqrt{3} \times \sqrt{3}$ surface," *Surface Science*, vol. 330, no. 1, pp. L639–L645, 1995.

[50] L. Li and I. S. T. Tsong, "Atomic structures of 6H-SiC (0001) and ($000\bar{1}$) surfaces," *Surface Science*, vol. 351, no. 1-3, pp. 141–148, 1996.

[51] C. Riedl, U. Starke, J. Bernhardt, M. Franke, and K. Heinz, "Structural properties of the graphene-SiC(0001) interface as a key for the preparation of homogeneous large-terrace graphene surfaces," *Physical Review B*, vol. 76, no. 24, p. 245406, 2007.

[52] L. Li and T. Sakurai, *Advances in Scanning Probe Microscopy*. Advances in Materials Research, Berlin: Springer, 2000.

[53] L. Muehlhoff, W. J. Choyke, M. J. Bozack, and J. John T. Yates, "Comparative electron spectroscopic studies of surface segregation on SiC(0001) and SiC(000$\bar{1}$)," *Journal of Applied Physics*, vol. 60, no. 8, pp. 2842–2853, 1986.

[54] T. Tsukamoto, M. Hirai, M. Kusaka, M. Iwami, T. Ozawa, T. Nagamura, and T. Nakata, "Structural analysis of the heat-treated 4H(6H)-SiC(0001) Si surface," *Surface Science*, vol. 371, no. 2-3, pp. 316–320, 1997.

[55] I. Forbeaux, J. M. Themlin, A. Charrier, F. Thibaudau, and J. M. Debever, "Solid-state graphitization mechanisms of silicon carbide 6H-SiC polar faces," *Applied Surface Science*, vol. 162-163, pp. 406–412, 2000.

[56] Z. Y. Xie, C. H. Wei, L. Y. Li, Q. M. Yu, and J. H. Edgar, "Gaseous etching of 6H-SiC at relatively low temperatures," *Journal of Crystal Growth*, vol. 217, no. 1-2, pp. 115–124, 2000.

[57] A. Charrier, A. Coati, T. Argunova, F. Thibaudau, Y. Garreau, R. Pinchaux, I. Forbeaux, J.-M. Debever, M. Sauvage-Simkin, and J.-M. Themlin, "Solid-state decomposition of silicon carbide for growing ultra-thin heteroepitaxial graphite films," *Journal of Applied Physics*, vol. 92, no. 5, pp. 2479–2484, 2002.

[58] T. Angot, M. Portail, I. Forbeaux, and J. M. Layet, "Graphitization of the 6H-SiC(0001) surface studied by HREELS," *Surface Science*, vol. 502-503, pp. 81–85, 2002.

[59] F. Meyer and C. J. Loyen, "Ellipsometry applied to surface problems," *Acta Electronica*, vol. 18, p. 33, 1975.

[60] J. Pezoldt, Y. V. Trushin, V. S. Kharlamov, A. A. Schmidt, V. Cimalla, and O. Ambacher, "Carbon surface diffusion and SiC nanocluster self-ordering," *Nuclear Instruments and Methods in Physics Research Section B*, vol. 253, no. 1-2, pp. 241–245, 2006.

[61] M. Bockstedte, A. Mattausch, and O. Pankratov, "*Ab initio* study of the migration of intrinsic defects in 3C-SiC," *Physical Review B*, vol. 68, p. 205201, Nov 2003.

[62] J. C. Meyer, A. K. Geim, M. I. Katsnelson, K. S. Novoselov, T. J. Booth, and S. Roth, "The structure of suspended graphene sheets," *Nature*, vol. 446, no. 7131, pp. 60–63, 2007.

[63] L. M. Viculis, J. J. Mack, and R. B. Kaner, "A chemical route to carbon nanoscrolls," *Science*, vol. 299, no. 5611, pp. 1361–, 2003.

[64] http://www.grapheneindustries.com, "Graphene industries, inc."

[65] J. Hass, R. Feng, T. Li, X. Li, Z. Song, W. A. de Heer, P. N. First, E. H. Conrad, C. A. Jeffrey, and C. Berger, "Highly ordered graphene for two dimensional electronics," *Applied Physics Letters*, vol. 89, no. 14, p. 143106, 2006.

[66] J. Hass, R. Feng, J. E. Millan-Otoya, X. Li, M. Sprinkle, P. N. First, W. A. de Heer, E. H. Conrad, and C. Berger, "Structural properties of the multilayer graphene/4H-SiC(000$\bar{1}$) system as determined by surface x-ray diffraction," *Physical Review B*, vol. 75, no. 21, p. 214109, 2007.

[67] E. Stolyarova, K. T. Rim, S. Ryu, J. Maultzsch, P. Kim, L. E. Brus, T. F. Heinz, M. S. Hybertsen, and G. W. Flynn, "High-resolution scanning tunneling microscopy imaging of mesoscopic graphene sheets on an insulating surface," *Proceedings of the National Academy of Sciences*, vol. 104, no. 22, pp. 9209–9212, 2007.

[68] A. C. Ferrari, J. C. Meyer, V. Scardaci, C. Casiraghi, M. Lazzeri, F. Mauri, S. Piscanec, D. Jiang, K. S. Novoselov, S. Roth, and A. K. Geim, "Raman spectrum of graphene and graphene layers," *Physical Review Letters*, vol. 97, no. 18, p. 187401, 2006.

[69] C. Faugeras, A. Nerriere, M. Potemski, A. Mahmood, E. Dujardin, C. Berger, and W. A. de Heer, "Few-layer graphene on SiC, pyrolitic graphite, and graphene: A Raman scattering study," *Applied Physics Letters*, vol. 92, no. 1, p. 011914, 2008.

[70] Z. H. Ni, W. Chen, X. F. Fan, J. L. Kuo, T. Yu, A. T. S. Wee, and Z. X. Shen, "Raman spectroscopy of epitaxial graphene on a SiC substrate," *Physical Review B*, vol. 77, no. 11, p. 115416, 2008.

[71] J. Rohrl, M. Hundhausen, K. V. Emtsev, T. Seyller, R. Graupner, and L. Ley, "Raman spectra of epitaxial graphene on SiC(0001)," *Applied Physics Letters*, vol. 92, no. 20, p. 201918, 2008.

[72] R. Rosei, M. De Crescenzi, F. Sette, C. Quaresima, A. Savoia, and P. Perfetti, "Structure of graphitic carbon on Ni(111): A surface extended-energy-loss fine-structure study," *Physical Review B*, vol. 28, pp. 1161–1164, Jul 1983.

[73] T. Aizawa, R. Souda, S. Otani, Y. Ishizawa, and C. Oshima, "Anomalous bond of monolayer graphite on transition-metal carbide surfaces," *Physical Review Letters*, vol. 64, pp. 768–771, Feb 1990.

[74] Y. Gamo, A. Nagashima, M. Wakabayashi, M. Terai, and C. Oshima, "Atomic structure of monolayer graphite formed on Ni(111)," *Surface Science*, vol. 374, no. 1-3, pp. 61–64, 1997.

[75] A. Nagashima, K. Nuka, K. Satoh, H. Itoh, T. Ichinokawa, C. Oshima, and S. Otani, "Electronic structure of monolayer graphite on some transition metal carbide surfaces," *Surface Science*, vol. 287-288, no. Part 2, pp. 609–613, 1993.

[76] A. Nagashima, N. Tejima, and C. Oshima, "Electronic states of the pristine and alkali-metal-intercalated monolayer graphite/Ni(111) systems," *Physical Review B*, vol. 50, pp. 17487–17495, Dec 1994.

[77] A. N. Obraztsov, E. A. Obraztsova, A. V. Tyurnina, and A. A. Zolotukhin, "Chemical vapor deposition of thin graphite films of nanometer thickness," *Carbon*, vol. 45, no. 10, pp. 2017–2021, 2007.

[78] P. Yi, S. Dong-Xia, and G. Hong-Jun, "Formation of graphene on Ru(0001) surface," *Chinese Physics*, vol. 16, no. 11, pp. 3151–3153, 2007.

[79] P. E. Quesenberry, *Scanning Tunneling Microscopy Studies of a Reactive Interface: Ni/GaAs*. PhD thesis, Georgia Institute of Technology, 1996.

[80] T. Li, *Characteristics of Graphite Films on Silicon- and Carbon- Terminated Faces of Silicon Carbide*. PhD thesis, Georgia Institute of Technology, Dec 2006.

[81] M. Sprinkle, *unpublished*. PhD thesis, Georgia Institute of Technology.

[82] D. P. Woodruff and T. A. Delchar, *Modern Techniques of Surface Science - Second Edition*. Cambridge University Press, New York, NY 10011-4211, United States, 1994.

[83] M. B. Webb and M. G. Lagally, *Elastic Scattering of Low-Energy Electrons from Surfaces*, vol. 28 of *Solid State Physics*. Academic Press, Inc., 1973.

[84] Veeco Metrology, Santa Barbara, CA 93117, *CP-II User's Guide*, 85-10354 rev. B ed., 2004.

[85] G. Binnig, C. F. Quate, and C. Gerber, "Atomic force microscope," *Physical Review Letters*, vol. 56, pp. 930–933, Mar 1986.

[86] R. García and R. Pérez, "Dynamic atomic force microscopy methods," *Surface Science Reports*, vol. 47, no. 6-8, pp. 197–301, 2002.

[87] G. Harris, ed., *Properties of silicon carbide, EMIS data review series*. No. 13, London: INSPEC, 1995.

[88] V. Ramachandran, M. Brady, A. Smith, R. Feenstra, and D. Greve, "Preparation of atomically flat surfaces on silicon carbide using hydrogen etching," *Journal of Electronic Materials*, vol. 27, no. 4, pp. 308–312, 1998.

[89] Q. Xue, Q. K. Xue, Y. Hasegawa, I. S. T. Tsong, and T. Sakurai, "Two-step preparation of 6H-SiC(0001) surface for epitaxial growth of GaN thin film," *Applied Physics Letters*, vol. 74, no. 17, pp. 2468–2470, 1999.

[90] I. T. L. Li, Y. Hasegawa and T. Sakurai, "Structures of SiC surfaces," *Journal de Physique IV*, vol. 6, pp. 167–172, Sept 1996.

[91] R. Kaplan, "Surface structure and composition of β- and 6H-SiC," *Surface Science*, vol. 215, no. 1-2, pp. 111–134, 1989.

[92] V. M. Bermudez, "Adsorption and co-adsorption of boron and oxygen on ordered α-SiC surfaces," *Applied Surface Science*, vol. 84, no. 1, pp. 45–63, 1995.

[93] L. I. Johansson, F. Owman, and P. Mårtensson, "High-resolution core-level study of 6H-SiC(0001)," *Physical Review B*, vol. 53, pp. 13793–13802, May 1996.

[94] K. Heinz, U. Starke, J. Bernhardt, and J. Schardt, "Surface structure of hexagonal SiC surfaces: key to crystal growth and interface formation?," *Applied Surface Science*, vol. 162-163, pp. 9–18, 2000.

[95] U. Starke, J. Schardt, J. Bernhardt, M. Franke, and K. Heinz, "Stacking transformation from hexagonal to cubic SiC induced by surface reconstruction: A seed for heterostructure growth," *Physical Review Letters*, vol. 82, pp. 2107–2110, Mar 1999.

[96] U. Starke, C. Bram, P. R. Steiner, W. Hartner, L. Hammer, K. Heinz, and K. Müller, "The (0001)-surface of 6H-SiC: morphology, composition and structure," *Applied Surface Science*, vol. 89, no. 2, pp. 175–185, 1995.

[97] T. Seyller, K. V. Emtsev, K. Gao, F. Speck, L. Ley, A. Tadich, L. Broekman, J. D. Riley, R. C. G. Leckey, O. Rader, A. Varykhalov, and A. M. Shikin, "Structural and electronic properties of graphite layers grown on SiC(0001)," *Surface Science*, vol. 600, no. 18, pp. 3906–3911, 2006.

[98] G. Gu, S. Nie, R. M. Feenstra, R. P. Devaty, W. J. Choyke, W. K. Chan, and M. G. Kane, "Field effect in epitaxial graphene on a silicon carbide substrate," *Applied Physics Letters*, vol. 90, no. 25, p. 253507, 2007.

[99] J. Hass, J. Millan-Otoya, P. First, and E. Conrad, "The interface structure of few layer epitaxial graphene grown on 4H-SiC(0001)," *Physical Review B (in press)*, 2008.

[100] H. Hibino, H. Kageshima, F. Maeda, M. Nagase, Y. Kobayashi, and H. Yamaguchi, "Microscopic thickness determination of thin graphite films formed on SiC from quantized oscillation in reflectivity of low-energy electrons," *Physical Review B*, vol. 77, no. 7, p. 075413, 2008.

[101] G. M. Rutter, J. N. Crain, N. P. Guisinger, P. N. First, and J. A. Stroscio, "Structural and electronic properties of bilayer epitaxial graphene," *Journal of Vacuum Science & Technology A*, vol. 26, no. 4, pp. 938–943, 2008.

[102] N. Sharma, *unpublished*. PhD thesis, Georgia Institute of Technology, 2009.

[103] J. Bernhardt, M. Nerding, U. Starke, and K. Heinz, "Stable surface reconstructions on 6H-SiC(0001)," *Materials Science and Engineering B*, vol. 61-62, pp. 207–211, 1999.

[104] L. I. Johansson, P. A. Glans, and N. Hellgren, "A core level and valence band photoemission study of 6H-SiC," *Surface Science*, vol. 405, no. 2-3, pp. 288–297, 1998.

[105] J. Bernhardt, J. Schardt, U. Starke, and K. Heinz, "Epitaxially ideal oxide–semiconductor interfaces: Silicate adlayers on hexagonal (0001) and (000$\bar{1}$) SiC surfaces," *Applied Physics Letters*, vol. 74, no. 8, pp. 1084–1086, 1999.

[106] A. Seubert, J. Bernhardt, M. Nerding, U. Starke, and K. Heinz, "In situ surface phases and silicon-adatom geometry of the (2x2)c structure on 6H-SiC(0001)," *Surface Science*, vol. 454-456, pp. 45–48, 2000.

[107] I. Forbeaux, J. M. Themlin, and J. M. Debever, "High-temperature graphitization of the 6H-SiC (000$\bar{1}$) face," *Surface Science*, vol. 442, no. 1, pp. 9–18, 1999.

[108] P. Badziag, "Composition of the reconstructed α-SiC(0001) surface," *Surface Science*, vol. 236, no. 1-2, pp. 48–52, 1990.

[109] F. Varchon, P. Mallet, L. Magaud, and J.-Y. Veuillen, "Rotational disorder in few-layer graphene films on 6H-SiC(000$\bar{1}$): A scanning tunneling microscopy study," *Physical Review B*, vol. 77, no. 16, p. 165415, 2008.

[110] M. A. Pimenta, G. Dresselhaus, M. S. Dresselhaus, L. G. Cancado, A. Jorio, and R. Saito, "Studying disorder in graphite-based systems by Raman spectroscopy," *Physical Chemistry Chemical Physics*, vol. 9, no. 11, pp. 1276–1290, 2007.

[111] W. J. Ong and E. S. Tok, "Role of Si clusters in the phase transformation and formation of (6×6)-ring structures on 6H-SiC(0001) as a function of temperature: An STM and XPS study," *Physical Review B*, vol. 73, no. 4, p. 045330, 2006.

[112] Y. Ma, "Simulation of interstitial diffusion in graphite," *Physical Review B*, vol. 76, no. 7, p. 075419, 2007.

[113] H. Matsunami, "Technological breakthroughs in growth control of silicon carbide for high power electronic devices," *Japanese Journal of Applied Physics*, vol. 43, pp. 6835–6847, Oct 2004.

[114] M. Kusunoki, T. Suzuki, K. Kaneko, and M. Ito, "Formation of self-aligned carbon nanotube films by surface decomposition of silicon carbide," *Philosophical Magazine Letters*, vol. 79, no. 4, pp. 153–161, 1999.

[115] T. Maruyama, H. Bang, N. Fujita, Y. Kawamura, S. Naritsuka, and M. Kusunoki, "STM and XPS studies of early stages of carbon nanotube growth by surface decomposition of 6H-SiC($000\bar{1}$) under various oxygen pressures," *Diamond and Related Materials*, vol. 16, no. 4-7, pp. 1078–1081, 2007.

[116] S. Irle, Z. Wang, G. Zheng, K. Morokuma, and M. Kusunoki, "Theory and experiment agree: Single-walled carbon nanotube caps grow catalyst-free with chirality preference on a SiC surface," *The Journal of Chemical Physics*, vol. 125, no. 4, p. 044702, 2006.

[117] I. K. Robinson, *Handbook on Synchrotron Radiation*, vol. 3. North-Holland, Amsterdam, 1991.

[118] E. Conrad, *Handbook of Surface Science*, vol. 1.7 Physical Structure: Diffraction Methods. Elsevier Science B.V., 1996.

[119] I. K. Robinson, "Crystal truncation rods and surface roughness," *Physical Review B*, vol. 33, pp. 3830–3836, Mar 1986.

[120] E. Vlieg, "Integrated intensities using a six-circle surface x-ray diffractometer," *Journal of Applied Crystallography*, vol. 30, pp. 532–543, Oct 1997.

[121] Q. Shen, "X-ray flux, brilliance and coherence of the proposed Cornell energy-recovery synchrotron source," Tech. Rep. 01-002, Cornell High Energy Synchrotron Source (CHESS), Cornell University, Ithaca, NY 14853, March 2001.

[122] http://www.aps.anl.gov/About, "Overview of the advanced photon source."

[123] http://www.coe.berkeley.edu/AST/srms/, "Synchrotron radiation for materials science."

[124] H. You, "Angle calculations for a '4S+2D' six-circle diffractometer," *Journal of Applied Crystallography*, vol. 32, pp. 614–623, Aug 1999.

[125] R. Feng, *Structural and Kinetics Study of Quantum Size Effect Pb Islands Grown on Si(111)*. PhD thesis, Georgia Institute of Technology, Dec 2006.

[126] T. M. Lu and M. G. Lagally, "Diffraction from surfaces with randomly distributed steps," *Surface Science*, vol. 120, no. 1, pp. 47–66, 1982.

[127] W. C. Elliott, P. F. Miceli, T. Tse, and P. W. Stephens, "Orientation dependence of homoepitaxy: An in situ x-ray scattering study of Ag," *Physica B: Condensed Matter*, vol. 221, no. 1-4, pp. 65–69, 1996.

[128] G. M. Rutter, N. P. Guisinger, J. N. Crain, E. A. A. Jarvis, M. D. Stiles, T. Li, P. N. First, and J. A. Stroscio, "Imaging the interface of epitaxial graphene with silicon carbide via scanning tunneling microscopy," *Physical Review B*, vol. 76, no. 23, p. 235416, 2007.

[129] F. Varchon, P. Mallet, J.-Y. Veuillen, and L. Magaud, "Ripples in epitaxial graphene," 2007.

[130] V. W. Brar, Y. Zhang, Y. Yayon, T. Ohta, J. L. McChesney, A. Bostwick, E. Rotenberg, K. Horn, and M. F. Crommie, "Scanning tunneling spectroscopy of inhomogeneous electronic structure in monolayer and bilayer graphene on sic," *Applied Physics Letters*, vol. 91, no. 12, p. 122102, 2007.

[131] J. K. Burdett, *Chemical Bonding in Solids*. Oxford University Press, 1995.

[132] W. Chen, H. Xu, L. Liu, X. Gao, D. Qi, G. Peng, S. C. Tan, Y. Feng, K. P. Loh, and A. T. S. Wee, "Atomic structure of the 6H-SiC(0001) nanomesh," *Surface Science*, vol. 596, no. 1-3, pp. 176–186, 2005.

[133] F. Varchon, R. Feng, J. Hass, X. Li, B. N. Nguyen, C. Naud, P. Mallet, J.-Y. Veuillen, C. Berger, E. H. Conrad, and L. Magaud, "Electronic structure of epitaxial graphene layers on SiC: Effect of the substrate," *Physical Review Letters*, vol. 99, no. 12, p. 126805, 2007.

[134] A. Mattausch and O. Pankratov, "*Ab Initio* study of graphene on SiC," *Physical Review Letters*, vol. 99, no. 7, p. 076802, 2007.

[135] A. Bostwick, T. Ohta, T. Seyller, K. Horn, and E. Rotenberg, "Quasiparticle dynamics in graphene," *Nature Physics*, vol. 3, no. 1, pp. 36–40, 2007.

[136] S. Y. Zhou, G. H. Gweon, A. V. Fedorov, P. N. First, W. A. de Heer, D. H. Lee, F. Guinea, A. H. Castro Neto, and A. Lanzara, "Substrate-induced bandgap opening in epitaxial graphene," *Nature Materials*, vol. 6, no. 10, pp. 770–775, 2007.

[137] N. Barrett, E. E. Krasovskii, J.-M. Themlin, and V. N. Strocov, "Elastic scattering effects in the electron mean free path in a graphite overlayer studied by photoelectron spectroscopy and LEED," *Physical Review B*, vol. 71, no. 3, p. 035427, 2005.

[138] R. E. Franklin, "The structure of graphitic carbons," *Acta Crystallographica*, vol. 4, pp. 253–261, May 1951.

[139] L. G. Cançado, M. A. Pimenta, R. Saito, A. Jorio, L. O. Ladeira, A. Grueneis, A. G. Souza-Filho, G. Dresselhaus, and M. S. Dresselhaus, "Stokes and anti-Stokes double resonance Raman scattering in two-dimensional graphite," *Physical Review B*, vol. 66, no. 3, 2002.

[140] L. A. Girifalco and R. A. Lad, "Energy of cohesion, compressibility, and the potential energy functions of the graphite system," *The Journal of Chemical Physics*, vol. 25, no. 4, pp. 693–697, 1956.

[141] A. N. Kolmogorov and V. H. Crespi, "Registry-dependent interlayer potential for graphitic systems," *Physical Review B*, vol. 71, no. 23, p. 235415, 2005.

[142] J. M. Hutcheon, *Modern Aspects of Graphite Technology*. London, New York: Academic Press, Inc., 1970.

[143] G. D. Barrera, J. A. O. Bruno, T. H. K. Barron, and N. L. Allan, "Negative thermal expansion," *Journal of Physics: Condensed Matter*, vol. 17, no. 4, pp. R217–R252, 2005.

[144] M. Weinert, E. Wimmer, and A. J. Freeman, "Total-energy all-electron density functional method for bulk solids and surfaces," *Physical Review B*, vol. 26, pp. 4571–4578, Oct 1982.

[145] G. Binnig, H. Rohrer, C. Gerber, and E. Weibel, "7×7 reconstruction on Si(111) resolved in real space," *Physical Review Letters*, vol. 50, pp. 120–123, Jan 1983.

[146] R. Young, J. Ward, and F. Scire, "Observation of metal-vacuum-metal tunneling, field emission, and the transition region," *Physical Review Letters*, vol. 27, pp. 922–924, Oct 1971.

[147] J. A. Golovchenko, "The tunneling microscope: A new look at the atomic world," *Science*, vol. 232, no. 4746, pp. 48–53, 1986.

[148] J. A. Stroscio and W. J. Kaiser, eds., *Scanning Tunneling Microscopy*. Academic Press, Inc., 1993.

[149] J. Tersoff and D. R. Hamann, "Theory of the scanning tunneling microscope," *Physical Review B*, vol. 31, pp. 805–813, Jan 1985.

[150] A. J. Melmed, "The art and science and other aspects of making sharp tips," *Journal of Vacuum Science & Technology*, vol. 9, no. 2, pp. 601–608, 1991.

[151] G. M. Rutter, J. N. Crain, N. P. Guisinger, T. Li, P. N. First, and J. A. Stroscio, "Scattering and interference in epitaxial graphene," *Science*, vol. 317, no. 5835, pp. 219–222, 2007.

[152] F. Varchon *Private communication*, 2008.

[153] K. Y. B. An, S. Fukuyama, "Graphitization of 6H-SiC(000$\bar{1}$) surface by scanning tunneling microscopy," *Japanese Journal of Applied Physics*, vol. 41, pp. 4890–4893, July 2002.

[154] M. Naitoh, M. Kitada, S. Nishigaki, N. Toyama, and F. Shoji, "An STM observation of the initial process of graphitization at the 6H-SiC(000$\bar{1}$) surface," *Surface Review & Letters*, vol. 10, no. 2/3, 2003.

[155] W.-T. Pong and C. Durkan, "A review and outlook for an anomaly of scanning tunnelling microscopy (STM): Superlattices on graphite," *Journal of Physics D: Applied Physics*, vol. 38, no. 21, pp. R329–R355, 2005.

[156] J. Steinier, Y. Termonia, and J. Deltour, "Smoothing and differentiation of data by simplified least square procedure," *Analytical Chemistry*, vol. 44, no. 11, pp. 1906–1909, 1972.

[157] R. M. Tromp, "Spectroscopy with the scanning tunnelling microscope: a critical review," *Journal of Physics: Condensed Matter*, vol. 1, no. 51, pp. 10211–10228, 1989.

[158] J. M. Campanera, G. Savini, I. Suarez-Martinez, and M. I. Heggie, "Density functional calculations on the intricacies of Moiré patterns on graphite," *Physical Review B*, vol. 75, no. 23, p. 235449, 2007.

[159] M. L. Sadowski, G. Martinez, M. Potemski, C. Berger, and W. A. de Heer, "Magnetospectroscopy of epitaxial few-layer graphene," *Solid State Communications*, vol. 143, no. 1-2, pp. 123–125, 2007.

[160] J. M. B. L. dos Santos, N. M. R. Peres, and A. H. C. Neto, "Graphene bilayer with a twist: Electronic structure," *Physical Review Letters*, vol. 99, no. 25, p. 256802, 2007.

[161] S. Latil, V. Meunier, and L. Henrard, "Massless fermions in multilayer graphitic systems with misoriented layers: *Ab initio* calculations and experimental fingerprints," *Physical Review B*, vol. 76, no. 20, p. 201402, 2007.

[162] K. V. Emtsev, A. Bostwick, K. Horn, J. Jobst, G. L. Kellogg, L. Ley, J. L. McChesney, T. Ohta, S. A. Reshanov, E. Rotenberg, A. K. Schmid, D. Waldmann, H. B. Weber, and T. Seyller, "Atmospheric pressure graphitization of SiC(0001)-a route towards wafer-size graphene layers," *http://arxiv.org/abs/0808.1222*, 2008.

VITA

Joanna Rachel Hass was born in Fairfax, Virginia on July 9, 1976. She lived in Reston, VA throughout her childhood and graduated from South Lakes High School in 1994. She received a Bachelor of Arts in Chemical Physics from Bowdoin College in Brunswick, ME in 1998. From there Joanna joined Teach For America, a non-profit organization that places top recent college graduates in full-time teaching positions in the most disadvantaged public schools in the United States. She taught Honors Physics, Algebra I, Geometry, and Algebra II at Greenwood High School in Greenwood, MS from 1998-2001. After spending one year completing physics coursework at the University of Mississippi and another year waitressing on St. John in the U.S. Virgin Islands, she joined the Georgia Tech Physics Department in 2003.